UNIVERSITÀ DI PARMA

Università degli Studi di Parma

Dottorato di Ricerca in
Ingegneria Civile e Architettura

Ciclo XXXI

# Swell and wind-waves interaction under partial reflection conditions

Coordinatore:
Prof. Andrea Carpinteri

Supervisor:
Prof. Sandro Longo, PhD

Co-supervisor:
Prof. María Clavero, PhD

Candidato: Fabio Addona

Anni 2015-2018

Ita res accendent lumina rebus

Lucrezio, *De Rerum Natura*

# Acknowledgments

Il primo ringraziamento va al professor Longo. Il suo lavoro in questi anni è stato un punto di riferimento imprescindibile, così come l'inesauribile disponibilità e il prezioso aiuto offerto in ogni fase del mio percorso.

Un sentito ringraziamento va a Luca, per tutte le discussioni, le chiacchierate e l'immancabile supporto ricevuti.

Doy las gracias a todas las personas conocidas en el fantastico Grupo de Dinámica de Flujos Ambientales del IISTA de Granada, a Fran, Montse, Rafa, Manolo, María, Sergio, Elisa, Asunción, Migue, Tino, y todos los que faltan en esta lista pero quedan en mi memoria. Y muchas gracias Andrea, por compartir alegrías y tristezas de mi camino desde el inicio hasta su conclusión.

Por último, un agradecimiento particular a Miguel, que siempre ha sido fuente de inspiracíón con sus ideas estimulantes y su cabeza siempre activa. Esta tesis nacío detrás de su idea.

A tutte le persone che mi sono state vicine: ai miei compagni di studio e di pranzo, Diana, Federico, Michele, Donatella.

Ai miei amici, alla mia famiglia, a Giusy e a Pippo. Ai miei genitori e a Davide, luci che mi hanno guidato come in passato, anche questo tortuoso sentiero.

Ad Alessandra, per il suo incondizionato affetto e sostegno, per la forza data nei momenti più luminosi e in quelli più bui, e per riempire il mio cuore.

# Abstract

The main aim of this thesis is to shed light about the influence that partial reflection (one of the most common cases encountered both in field and laboratory studies of water waves) exerts on a wave field where regular waves are present alone and under the action of following or opposing wind.

We have analyzed experimentally and theoretically the flow field of paddle waves, paddle waves plus following wind and paddle waves with opposing wind under partial reflection conditions in laboratory, in terms of free surface elevations, velocities and stresses.

For the theoretical and experimental analyses of the flow field, we consider velocities and free surface elevations as a superposition of a mean (current), a periodic (wave) and a turbulent (fluctuating) component.

A theoretical model for the periodic (wave) component is developed by means of a perturbation scheme considering the wave field as a superposition of an incident, a reflected and a bound wave. The phase shift between the incident and the reflected wave is included in the analysis. The theory yields an analytical formulation of the wave components of velocities and stresses, and a spatial variation of the mean water level. The model also predicts the principal stresses, as well as the angle of the principal axes, of both the Reynolds wave and turbulent stress tensors.

The wave flume used for the experimental activity provides a complete control of the generated and reflected wave conditions, and is used to investigate the influence of partial reflection on the main variables of interest, i.e. velocity and free surface elevation, and the combined effect of regular waves and wind action.

We measure velocity and free surface elevation in two different sets of experiments: in the first series, paddle waves and paddle waves plus following wind are observed and studied; in the second series, paddle waves with opposing wind are observed and studied.

Data analysis allows a complete representation of the experimental velocities, stresses and free surface characteristics of the flow field. Time average yields the mean components, phase average yields the wave (periodic) components, while the residual part (after time and phase average) represents the fluctuating components. A spectral filter is also used for the separation of the free surface elevation component attributed to the paddles (wave) and to the wind (turbulent). Several analyses of velocity and free surface data are performed to quantify the experimental contributions of the separated components.

The discussions of the two series of experiments show separately the main results of the activities, and the final conclusions offer a unified vision of the advances brought by this thesis in the wide scenario of swell and wind waves interaction under partially-reflective conditions.

# Contents

# List of Tables

# List of Figures

# Introduction

Water covers most of the entire surface on the Earth. At the interface between water and atmosphere, surface gravity waves manifest themselves at different scales, varying from ripples (dominated by capillarity) to planetary waves (governed by earth rotation, gravity, latitude and ocean depth). The interaction with atmosphere determines the exchanges of heat, momentum, gas and in general can modify the global balance of substances relevant for humans, like carbon dioxide ($CO_2$), in air and water.

Several researchers have investigated and analysed the vertical momentum flux in surface gravity waves subjected to the action of wind, shoaling or decay. The vertical momentum balance is important in order to determine the exchanges of chemicals, sediments and pollutants, which take place at the air-sea interface. Although it is not clear how the momentum is transferred from air to water (and vice versa), theoretical models which describe the interaction of wind and water have been developed to shed light on the mechanisms responsible for wave growth and attenuation (Phillips, 1957; Miles, 1957; Longuet-Higgins, 1969*a*). Wind waves and swell are probably the most common and prominent for human activities, with wave periods $T$ of 1–25 s. Usually, swell comprises waves that are fully developed and propagate far from their generation area, generally showing a regular behavior if compared to early-stage growing waves. As any other free water surface, swell can be subjected to the action of the wind, potentially coming from any direction.

In the past, a special attention was given to the study of swell waves under the action of wind blowing in the same direction. Longuet-Higgins &

Stewart (1960) derived an analytical form to describe the evolution of the short wave shape on long waves crests (shorter and steeper) and troughs (longer and lower). Phillips (1963) showed from a theoretical point of view how short waves breaking on a longer wave crest can subtract energy causing an attenuation of the long wave, and Longuet-Higgins (1969*b*) described a maser-like mechanism of energy transfer from shorter to longer waves using the radiation stress concept. Hasselmann (1971) states that the long wave attenuation due to dissipation represents the difference between the positive work done by the interaction stress, defined as the transfer of momentum between the mean motion and the wave field, and the loss of potential energy due to the mass transfer. Then, Garrett & Smith (1976) pointed out that the correlation between the generation of short waves and the orbital velocity of long waves, assumed zero by Hasselmann, can cause a positive (negative) momentum transfer from shorter to longer waves in case of following (opposing) wind. Experimental works (see, e.g., Mitsuyasu & Honda, 1982; Hsu & Hsu, 1983; Thais & Magnaudet, 1996; Grare *et al.*, 2013) and field campaigns (Dobson, 1971; Snyder *et al.*, 1981) report that swell (or monochromatic waves, in laboratory) energy is generally increased when ruffled by following wind, while wind-generated waves and their growth are attenuated or suppressed when superimposed to longer waves (Belcher *et al.*, 1994; Donelan, 1987; Chen & Belcher, 2000). Sullivan & McWilliams (2010) gave an overlook of the main effects of water waves coupling with adjacent wind and currents, while Deigaard & Nielsen (2018) studied the mechanisms of energy and momentum transfer between wind and waves, distinguishing between the spatial and the temporal growth. Cavaleri *et al.* (2007) underlined the role of the wind stress modulation, which works against the wave orbital velocity and should be added to the long wave energy rate of change. The overall result is that long waves would be amplified when propagating in the same direction of the wind, and attenuated when waves and wind are in opposite direction.

Wind-following swell waves represent just one of the possible states of the sea. In reality, wind faces swell from all directions when weather conditions change rapidly in time and space, as in tropical cyclones. Dobson (1969), in their Appendix 2 noticed that wave groups were damped by an adverse wind, and encouraged further works to study the reason of the observed damping, due to the important role that this effect may have in wave weather forecasting. Stewart & Teague (1980) measured the interaction of swell and wind offshore of Galveston Island, Texas, for a distance of 80 m. They observed a wave growth as a function of the angle to wind, and the decay for swell propagating against the wind by both radar and wave staffs. Young & Sobey (1985) conducted experiments for evaluating specifically the wave field of mechanically-generated waves superposed to an opposing wind. They found that (i) the rate of decay of the long wave is proportional to the square of the wave slope and the ratio between wind and wave phase speed, and (ii) the Reynolds wave horizontal normal stress (computed from velocity measurements) is the most relevant component which causes the decay of the long wave in opposing winds. Donelan *et al.* (1997) measured, amongst other quantities, the directional spectra of waves in ocean, observing that counter- and cross-swell waves (with respect to wind direction) can yield drag coefficients much larger than in case of pure wind. Peirson *et al.* (2003) carried out experiments with monochromatic waves propagating against an opposing wind, measuring the long wave attenuation. They found that the magnitude of long wave growth rates due to following wind forcing is approximately 2.5 times smaller than the magnitude of wave attenuation rates due to comparable opposing winds.

It is known that waves approaching coasts always encounter reflective conditions due, amongst others, to shoreline or anthropogenic structures like breakwaters, making reflection and its effects almost ubiquitous. Stewart & Teague (1980), in their field campaign, estimated a reflection coefficient (the ratio between the reflected and the incoming wave energy) larger than expected, i.e. about 1%, and were surprised that even natural beaches with mild slope could cause a measurable wave reflection. Peirson *et al.* (2003), in their laboratory investigation, described some difficulties during experiments since the wave field was contaminated by wave reflection, addressing the problem by positioning a polyethylene sheet at the two sides of the tank. They affirm that the measured reflection was finally less than 2%, even though they do not specify the analysis followed for the evaluation of the reflection. Generally, vertical breakwaters reflect more than 70% of the incoming wave energy, while rubble-mound breakwaters $\approx 30 - 40\%$. However, it is not well understood how relevant the perturbations due to reflected components are when compared to the other quantities involved in the process, thus there still lacks a uniform path towards the inclusion of reflective conditions in wave models. Notice that, in natural environments, perfect (complete) reflection does not exist and we should speak always about partial reflection. Coastal areas are one of the most common places where waves are partially reflected; for long waves, partial reflection involves all the continental shelf areas. Ardhuin & Roland (2012) showed that including a coastal reflection parametrization in a phase-averaged wave model is necessary to reproduce the relatively broad directional spectra, and that the steepness of the shore plays a fundamental role in this process. Yu & Mei (2000) showed that, when some reflection appears from the shore, in some condition the outgoing wave exhibits more energy than the incident wave, increasing the hazards to the beach. Partial reflection also affects sediment transport and bed forms, contributing to the structural change of the bottom boundary layer, and its effects can be particularly relevant in shallow water. Partial reflection of regular wave groups gives a high-order contribution to the steady shear stress, introducing a further scale in a flow field already controlled by several effects (Sánchez-Badorrey *et al.*, 2009); also, it could induce toe erosion and the generation of rhythmic bed forms (Sánchez-Badorrey *et al.*, 2008). It means that the sediment transport mechanism can be significantly influenced by the presence of progressive (incoming) and retrogressive (reflected) wave trains. In particular, their interaction can enhance scouring and favor the failure of break waters and protective structures (Baquerizo & Losada, 1999*a*). Partial reflection also modulates nonlinear water waves, which combined to the action of currents change the intensity of sediment transport (Ribberink *et al.*, 1995).

Research on local effects of partial reflection can be easily extended to larger scales. Understanding the main features of the interaction between air and water provides a great step in advance to predict global phenomena, like climate change, which influence man life and Earth environment. We infer that partially–reflected waves also influence the ocean circulation patterns and can affect exchanges of chemicals (like carbon dioxide), in particular in continental shelves. Several techniques have beeen developed since the sixties to obtain quantitative estimates of $CO_2$ in the ocean (Park, 1969; Dickson *et al.*, 2007), noticing that the ocean plays a main role for the atmospheric $CO_2$ concentration, acting like a tank capable of retaining $CO_2$ in deep waters (Bopp *et al.*, 2002; Le Quéré *et al.*, 2003).

It is widely accepted that continental shelves have a prominent role in the carbon and nitrogen global cycle. Even though direct observations hardly give enough reliable information, biogeochemical model-based simulations reveal the importance of shelves in nitrogen sinking and carbon fluxes to the open ocean deep waters (see Fennel, 2010). The fluxes at the sea-atmosphere interface of carbon, nitrogen, phosphorus, and oxygen due to anthropogenic perturbations of the environment are particularly relevant in the coastal ocean (Mackenzie *et al.*, 2011). Several elements suggest that continental shelves may have turned into a net sink for $CO_2$ during post-industrial times, even though air–water $CO_2$ fluxes are subjected to large uncertainties (50% or more) in coastal waters, due to the complex physics and to the heterogeneity (and lack) of the data (Bauer *et al.*, 2013). High uncertainty in the global $CO_2$ budget estimates can also be attributed to the biased distribution of local studies, and to the different definitions of the continental shelf domain given by different studies (Laruelle *et al.*, 2010). However, the global trend of model-based evaluations yields a more $CO_2$ density flux at the continental shelves ($-0.7$ to $-1.2\,\mathrm{mol\,C\,m^{-2}\,yr^{-1}}$) than at the open ocean ($-0.5\,\mathrm{mol\,C\,m^{-2}\,yr^{-1}}$), with a relevant contribution of the arctic shelves to the global $CO_2$ uptake ($-0.07\,\mathrm{Pg\,C\,yr^{-1}}$). These results rely on advanced models, which calculate air-water gas fluxes by means of global data about direct $CO_2$ measurements of surface ocean and of available temperature, salinity, and wind speed field data (Laruelle *et al.*, 2014). To date, however, the use of global models is still debated. It is demonstrated (Fiechter *et al.*, 2014) that coarse resolution may not represent effectively ocean circulation, wind-driven upwelling, coastal currents. Coastal ocean processes should be modeled with high-grid resolution to include the direction of $CO_2$ transfer (from or to the water), and the effects of mesoscale eddies, which affect the $CO_2$ fluxes in continental shelves (Lachkar *et al.*, 2007; Borges, 2005).

The extensive literature about air-sea interaction research (and its interdisciplinarity) highlights the great importance that this subject has for human life. But answers and discoveries given so far still remain controversial and are accompanied by serious doubts and uncertainties. The work of this thesis is inspired by the need to shed light on this subject.

For our analysis, the variables of interest of the wave field (velocity and free surface elevation) are described as a linear superposition of a mean, a periodic and a fluctuating component. This view of the flow field is usually called triple decomposition (see, e.g. Phillips, 1966; Thais & Magnaudet, 1995) and it is useful to separate and evaluate the single effect of each component. Horizontal and vertical velocities are written as $u = \overline{u} + \widetilde{u} + u'$, and $w = \overline{w} + \widetilde{w} + w'$, where the overline is time average (mean component), the tilde is phase average (wave-induced or periodic component) and the prime is fluctuation or turbulence. When time and phase averages are applied to the horizontal momentum equations, the shear stress in the vertical results as the combination of several correlations (or covariances) between mean, periodic and fluctuating component. Among them, the interest is focussed on the term $-\overline{\widetilde{u}\widetilde{w}}$, which is defined as Reynolds wave shear stress, velocity correlation (between the horizontal and vertical velocity) or velocity covariance. In the absence of sinks or sources, for progressive waves which propagate over a rigid flat bottom in uniform depth this term is always null, because from linear potential theory of water waves the horizontal and vertical periodic velocities $\widetilde{u}$ and $\widetilde{w}$ are 90° out of phase (in quadrature). However, several studies demonstrated that, in different conditions of the wave field, the velocity covariance is different from zero. For instance, Deigaard & Fredsøe (1989) showed that, in dissipative water waves, the efficiency of vertical momentum transfer and the fluxes of energy can be explained by a non-null contribution of $-\overline{\widetilde{u}\widetilde{w}}$, due to the change of the wave conditions in the propagating direction of the waves. In particular, the Reynolds wave shear stress exhibits a linear profile in the vertical for dissipative conditions near the bottom and near the surface. (De Vriend & Kitou, 1991) derived analytically a linear profile of the Reynolds wave shear stress by including some wave-effects into a three-dimensional current model. Rivero & Arcilla (1995) introduced the oscillatory vorticity

$\overline{\widetilde{w}\widetilde{\omega}}$, where the vector $\widetilde{\omega}$ is perpendicular to $u$ and $w$, in order to explain the out-of-quadrature velocity covariance which can emerges from several sources. For irrotational flows, their results are consistent to those of other researchers. See also the experimental study of irregular waves on a sloping sand bottom conducted in De Serio & Mossa (2013). Olfateh *et al.* (2017) focussed their study on the velocity correlation $-\overline{\widetilde{u}\widetilde{w}}$, and reported contradicting experimental and field results in literature. They showed existing variegated data of the Reynolds wave shear stress and that its contribution to the momentum transfer under regular and wind generated waves vary in sign and intensity. They put the attention on the role of reflection in laboratory activities, in addition to possible contamination due to secondary recirculation cells in the experimental channels. They also derived a theoretical relation to explain the behaviour of the Reynolds shear stress and its spatial variation, but they do not include the phase shift between the incoming and reflected wave trains and averaged their results in the horizontal. The lack of a universal approach to the problem is a sufficient reason to encourage further studies of reflection effects on the wave field.

Experiments and analyses of this thesis are thought to yield a better comprehension of the wave field contaminated by reflection. In particular, it concerns with an analytical and experimental study of the interaction between wind and paddle-generated waves affected by reflection. One of the aims of this work is to analyse how different reflective conditions influence the flow field in the water side, and to compare reflection-induced stress with other forcing terms (such as turbulence). Wind and regular paddle waves are generated, together and separately, in an ocean-atmosphere interaction flume, which allows active absorption in order to obtain the reflection desired for each experiment. The possibility of generating a desired reflection in the wave field allows a complete assessment and quantification of the reflective effect on the wave field.

The particular type of flume used for experiments of this work represents a step in advance in studying physical models of complex phenomena. A complete control of wave generation and reflective conditions for a sufficient long time gives the chance to observe, investigate and analyse the flow field in a way that it is not possible to reproduce in standard facilities and in field campaigns. The scenario of investigation can be simplified, giving the tools to separate the effects of the single factors which occur in natural environment, where local morphology, bottom dynamics, currents and other elements also influence the overall dynamics of flow field and sediment transport mechanism. The general evolution of the sand bottom is strongly influenced by small changes in the wave field, where the interaction of incoming and partially-reflected waves play a fundamental role also on the dynamics of the bottom boundary layer. We remind that bed forms, like ripples and sandbars, grow up and evolve as answer to the small perturbations which reach and propagate on the moving bed.

In this framework, the emerging of additional stresses (like the term $\overline{\tilde{u}\tilde{w}}$), the spatial modulation of the mean water level and other phenomena are experimentally observed and theoretically derived. Furthermore, wind in the same and in opposite direction can be superposed to the paddle waves, and the interaction between wind and reflection is investigated yielding to novel observations.

The thesis is structured as follows. In Chapter 1, the theoretical approach used for the analytical derivation of the quantities observed is presented. In Chapter 2, the experimental set-up, the tests and the instrumentation used are described, including the techniques used for data analysis and the related uncertainty. In Chapter 3, results about the influence of partial reflection on the wave shear stress and the mean water level are shown, for only-paddle waves and paddle waves with wind blowing in the same direction. In Chapter 4, the effects of partial reflection on paddle waves opposing wind are reported, confirming the correct approach of Chapter 3 and showing new results. Finally, the general conclusions of the thesis and considerations for future works are given.

# Chapter 1

# Theory

This chapter includes the study by Addona *et al.* (2018). A perturbation scheme for the calculation of the wave velocity potential is developed, considering the wave field as the superposition of an incident, a reflected and a bound wave. An analytical form of the periodic velocities and stresses (including the phase shift between and the reflected waves) is obtained. By means of the radiation stress concept, a spatial variation of the mean water level can be calculated. The analysis is also extended to the Reynolds wave and turbulent stress tensors, in terms of the principal stresses and angle.

## 1.1 Regular waves under partial reflection conditions

In this theoretical treatment only the periodic components are considered, following the analysis by Goda & Abe (1968) for water waves under partial reflection conditions which propagate over a flat bottom. We make use of the Stokes waves theory, expressing the free surface elevation and the velocity potential in terms of harmonic series. The potentials of a progressive and a reflected wave can be written as a linear combination of the independent potentials. However, non-linear effects require a third component which represents the interaction term, often described as "bound" wave because it is nondispersive in frequency. The wave velocity potential $\Phi$ and the free surface displacement $\eta$ of an incoming and a reflected finite-amplitude wave train are

$$\Phi = \Phi_i + \Phi_r + \Phi_b, \quad \eta = \eta_i + \eta_r + \eta_b, \tag{1.1}$$

where $i$, $r$ and $b$ are the "incident", "reflected" and "bound" components, respectively. We introduce the small parameter $\epsilon = a_i$, equal to the incident wave amplitude, to expand in series the wave potential as

$$\begin{aligned} \Phi_i &= \epsilon\Phi_i^{(0)} + \epsilon^2\Phi_i^{(1)} + O(\epsilon^3), \\ \Phi_r &= K_r\epsilon\Phi_r^{(0)} + K_r^2\epsilon^2\Phi_r^{(1)} + O(\epsilon^3), \\ \Phi_b &= \epsilon^2\Phi_b^{(1)} + O(\epsilon^3), \end{aligned} \tag{1.2}$$

and the free surface elevation as

$$\begin{aligned} \eta_i &= \epsilon\eta_i^{(0)} + \epsilon^2\eta_i^{(1)} + O(\epsilon^3), \\ \eta_r &= K_r\epsilon\eta_r^{(0)} + K_r^2\epsilon^2\eta_r^{(1)} + O(\epsilon^3), \\ \eta_b &= \epsilon^2\eta_b^{(1)} + O(\epsilon^3), \end{aligned} \tag{1.3}$$

where $K_r$ is the ratio of the reflected wave amplitude to the incident wave amplitude. The potentials of the incident and the reflected waves satisfy the classical differential problem

$$\left.\begin{aligned} &\Phi_{,xx} + \Phi_{,zz} = 0, \quad -h < z < \eta, \quad \forall x, \\ &g\eta + \Phi_{,t} + \frac{1}{2}\left[(\Phi_{,x})^2 + (\Phi_{,z})^2\right] \quad \text{on } z = \eta, \\ &\Phi_{,z} = \eta_{,t} + \eta_{,x}\Phi_{,x} \qquad \text{on } z = \eta, \\ &\Phi_{,z} = 0 \quad \text{on } z = -h, \end{aligned}\right\} \tag{1.4}$$

with the additional conditions of water mass conservation over a wave length $L$

$$\int_0^{2\pi/k} \eta(x,t)\mathrm{d}x = 0, \tag{1.5}$$

and periodicity both in time and space

$$\nabla\Phi(x,z,t+2\pi/\omega)=\nabla\Phi(x+2\pi/k,z,t)=\nabla\Phi(x,z,t), \tag{1.6}$$

where $x-z$ is the reference system (the horizontal and vertical coordinate, respectively) with the origin at the still water level ($z=-h$ is the rigid flat bottom), $g$ is gravity acceleration, $t$ is the time, $T$ is the wave period, $\omega=2\pi/T$ is the radial frequency and $k=2\pi/L$ is the wave number. The comma in the subscript stands for the partial derivative.

To the second order, the solution reads

$$\eta_j=a_j\cos(k_jx-\omega_jt+\varphi_j)+\\ \frac{a_j^2}{4k_j}[3\coth^3(k_jh)-\coth(k_jh)]\cos[2(k_jx-\omega_jt+\varphi_j)], \tag{1.7}$$

for the free surface elevation, and

$$\Phi_j=\frac{a_j\omega_j}{k_j}\frac{\cosh[k_j(z+h)]}{\sinh(k_jh)}\sin(k_jx-\omega_jt+\varphi_j)+\\ \frac{3a_j^2\omega_j}{8}\frac{[\coth^4(k_jh)-1]\cosh[2k_j(z+h)]}{\cosh(2k_jh)}\times\\ \sin[2(k_jx-\omega_jt+\varphi_j)]-\frac{a_j^2\omega_j^2}{4\sinh^2(k_jh)}t, \tag{1.8}$$

for the wave potential, where $j=i,r$, $\varphi_j$ is an initial phase shift (when $x$ and $t$ are null) and the dispersion relation $\omega_j^2=gk_j\tanh k_jh$ holds. Equations (1.8–1.7) can refer to the incident and the reflected wave component by substituting $k_i=-k_r\equiv k$, $a_r=K_ra_i$, $\omega_i=\omega_r\equiv\omega$ and specifying the initial phases $\varphi_i$ and $\varphi_r$, respectively. We also define $\theta_i=kx-\omega t+\varphi_i$ and $\theta_r=kx+\omega t-\varphi_r$, with their sum $\theta_i+\theta_r=2kx+\varphi_i-\varphi_r$ (time-independent) and difference $\theta_r-\theta_i=2\omega t-\varphi_i-\varphi_r$ (space-independent).

The solutions for the bound wave potential and the bound free surface elevation are obtained by imposing that $\Phi$ and $\eta$ satisfy the system of differential equations (1.2–1.3), with components expressed by equations

(1.2–1.3), and the conditions (1.5-1.6). The result to the first order is null, while to the second order reads

$$\begin{aligned}\Phi_b &= \frac{K_r a_i^2 \omega}{4}[3+\coth^2(kh)]\sin(\theta_r-\theta_i),\\ \eta_b &= K_r k a_i^2 \coth(2kh)\cos(\theta_i+\theta_r).\end{aligned} \tag{1.9}$$

Notice that bound wave potential does not contribute to the velocity field since it only depends on $t$, and that $\eta_b$ does not depend on $t$, i.e. the bound wave is stationary.

The horizontal $\widetilde{u}$ and vertical $\widetilde{w}$ velocities are computed by differentiating the wave potential:

$$\begin{aligned}\widetilde{u}(x,z,t) \equiv \Phi_{,x} =& \frac{g a_i k}{\omega}\frac{\cosh[k(z+h)]}{\cosh(kh)}(\cos\theta_i - K_r\cos\theta_r)+\\ &\frac{3}{4}\frac{g a_i^2 k^2}{\omega}\frac{\cos[2k(h+z)]}{\cosh(kh)\sinh^3(kh)}[\cos(2\theta_i)-K_r^2\cos(2\theta_r)],\end{aligned} \tag{1.10}$$

$$\begin{aligned}\widetilde{w}(x,z,t) \equiv \Phi_{,z} =& \frac{g a_i k}{\omega}\frac{\sinh[k(z+h)]}{\cosh(kh)}(\sin\theta_i - K_r\sin\theta_r)+\\ &\frac{3}{4}\frac{g a_i^2 k^2}{\omega}\frac{\sinh[2k(h+z)]}{\cosh(kh)\sinh^3(kh)}[\sin(2\theta_i)-K_r^2\sin(2\theta_r)].\end{aligned} \tag{1.11}$$

where the tilde identifies the periodic (wave-induced) component of the velocity. We see the wave potential solution of equation (1.8) does contribute to the second-order orbital velocities, represented by the second term of the R.H.S. of equations (1.10–1.11). The instantaneous free surface elevation results

$$\begin{aligned}\eta(x,t) = a_i(\cos\theta_i + K_r\cos\theta_r) + \frac{k a_i^2}{4}[3\coth^3(kh)-\coth(kh)]\times\\ [\cos(2\theta_i)+K_r^2\cos(2\theta_r)] + K_r k a_i^2\coth(2kh)\cos(\theta_r+\theta_i).\end{aligned} \tag{1.12}$$

If only the linear contribution is considered in equation (1.12), we find nodes and antinodes at $x_n = mL/4 - (\varphi_i - \varphi_r)L/(4\pi)$, and $x_a = mL/2 - (\varphi_i - \varphi_r)L/(4\pi)$, $\quad m = 0, 1, 2, \ldots$, respectively. Including the second-order components, the antinodes and nodes fluctuate around the sections at $x_n$ and $x_a$.

From equations (1.10–1.11), a time average of the covariance $-\widetilde{u}\widetilde{w}$ results

$$
\begin{aligned}
-\overline{\widetilde{u}\widetilde{w}} = K_r g k a_i^2 \frac{\sinh[2k(z+h)]}{\sinh(2kh)} \sin(\theta_i + \theta_r) + \\
\frac{9}{16} K_r^2 g k^3 a_i^4 \frac{\sinh[4k(h+z)]}{\sinh^6(kh)\sinh(2kh)} \sin(2\theta_i + 2\theta_r). \quad (1.13)
\end{aligned}
$$

For progressive waves, horizontal and vertical velocities are 90° out of phase and their averaged product is null. When reflection is present, the velocity correlation is different from zero, with maximum values achieved in case of total reflection ($K_r \to 1$). From equation (1.13), the sinusoidal spatial variation of $-\overline{\widetilde{u}\widetilde{w}}$ supports a variation of the mean water level, also at the first order. We take advantage of the radiation stress concept to evaluate the mean water level.

## 1.2 Radiation stress for water waves in partially-reflective condition

We follow the analysis by Longuet-Higgins & Stewart (1964) to evaluate the wave-induced component $S_{xx}$ of the radiation stress as

$$
\begin{aligned}
S_{xx} = \overline{\int_{-h}^{\zeta} (p + \rho\widetilde{u}^2)\mathrm{d}z} - \int_{-h}^{0} p_0 \mathrm{d}z \equiv \\
\overline{\int_{-h}^{\zeta} \rho\widetilde{u}^2 \mathrm{d}z} + \overline{\int_{-h}^{0} (p - p_0)\mathrm{d}z} + \overline{\int_{0}^{\zeta} p\mathrm{d}z} \equiv S_{xx}^{(1)} + S_{xx}^{(2)} + S_{xx}^{(3)}, \quad (1.14)
\end{aligned}
$$

with $\zeta = \overline{\zeta} + \eta$, where $\overline{\zeta}$ represents the mean water level, $p$ and $p_0$ are total and hydrostatic pressure, respectively.

The first contribution in equation (1.14) is

$$
\begin{aligned}
S_{xx}^{(1)} = \overline{\int_{-h}^{\zeta} \rho \widetilde{u}^2 \mathrm{d}z} \equiv \overline{\int_{-h}^{0} \rho \widetilde{u}^2 \mathrm{d}z} \equiv \int_{-h}^{0} \rho \overline{\widetilde{u}^2} \mathrm{d}z = \\
\frac{\rho g a_i^2 [2hk + \sinh(2hk)]}{4 \sinh(2hk)} \left[1 + K_r^2 - 2K_r \cos\left(\theta_i + \theta_r\right)\right] \equiv \\
\frac{E}{2}(G+1)\left[1 + K_r^2 - 2K_r \cos\left(2kx + \Delta\varphi\right)\right], \quad (1.15)
\end{aligned}
$$

where we introduce the incident-wave energy density $E = \rho g a_i^2/2$ and the term $G = 2kh/\sinh(2kh)$. The integral in the domain $[0,\ \zeta]$ is of higher order and has been neglected, and the time mean operator has been transferred to the argument of the integral since the two extremes of integration $-h$ and 0 do not depend on time.

The second contribution in equation (1.14) is

$$
S_{xx}^{(2)} = \int_{-h}^{0} (\overline{p} - p_0) \mathrm{d}z, \quad (1.16)
$$

and requires the knowledge of the pressure. The pressure can be evaluated by considering the vertical flux of momentum, which yields

$$
\overline{p} - p_0 = -\rho \overline{\widetilde{w}^2} - \rho \int_{0}^{z} \frac{\partial \overline{\widetilde{u}\widetilde{w}}}{\partial x} \mathrm{d}z + \rho g \overline{\zeta}, \quad (1.17)
$$

hence

$$
\begin{aligned}
S_{xx}^{(2)} = \frac{\rho g a_i^2 [2hk - \sinh(2hk)]}{4 \sinh(2hk)} \left[1 + K_r^2 + 2K_r \cos\left(\theta_i + \theta_r\right)\right] + \\
\frac{1}{2} \rho g a_i^2 K_r [1 - 2hk \coth(2hk)] \cos\left(\theta_i + \theta_r\right) + \rho g h \overline{\zeta} \equiv \\
\frac{E}{2}(G-1)\left[1 + K_r^2 + 2K_r \cos\left(\theta_i + \theta_r\right)\right] + \\
E K_r [1 - 2hk \coth(2hk)] \cos\left[\theta_i + \theta_r\right] + \rho g h \overline{\zeta}. \quad (1.18)
\end{aligned}
$$

The third contribution in equation (1.14) is evaluated by assuming a hydrostatic pressure in $[0,\ \zeta]$, equal to $p = \rho g(\zeta - z)$, hence

$$S_{xx}^{(3)} = \frac{1}{2}\rho g\overline{\zeta^2} \equiv \frac{1}{4}\rho g a_i^2 \left[K_r^2 + 1 + 2K_r \cos\left(\theta_i + \theta_r\right)\right] \equiv \frac{E}{2}\left[K_r^2 + 1 + 2K_r \cos\left(\theta_i + \theta_r\right)\right], \quad (1.19)$$

where a term $\propto \overline{\zeta}^2$ has been neglected.

Upon substitution of all terms in equation (1.14) yields

$$S_{xx} = E\left(G + \frac{1}{2}\right)(1 + K_r^2) - EGK_r \cos(\theta_i + \theta_r)\cosh(2hk) + \rho g h\overline{\zeta}. \quad (1.20)$$

From conservation of momentum along $x$, it follows that, in the absence of a forcing, momentum cannot accumulate and $S_{xx}$ is equal to its horizontal average (along $x$) over a wave length. Hence equation (1.20) becomes

$$S_{xx} = E\left(G + \frac{1}{2}\right)(1 + K_r^2). \quad (1.21)$$

For progressive waves ($K_r \to 0$) it reduces to

$$S_{xx} = E\left(G + \frac{1}{2}\right), \quad (1.22)$$

and in case of total reflection $K_r = 1$ (standing waves)) it yields

$$S_{xx} = 2E\left(G + \frac{1}{2}\right), \quad (1.23)$$

which collapses to the result in Longuet-Higgins & Stewart (1964).

### 1.2.1 Mean water level

Partial reflection conditions induce a modulation of the wave shear stress $-\rho\overline{\tilde{u}\tilde{w}}$ along $x$. This modulation supports a variation of the mean water level $\overline{\zeta}$, which can be computed from equation (1.20) by imposing the balance between the two last terms on the right-hand side:

$$\overline{\zeta} = ka_i^2 K_r \coth(2kh) \cos\left(\theta_i + \theta_r\right) + \text{const.} \tag{1.24}$$

The mean water level, as the velocity covariance, has a spatial modulation along $x$ with minima and maxima that are not necessarily in the nodes and in the antinodes. The constant can be evaluated by imposing mass conservation in a finite length channel, and is negligible for long channels (long with respect to the wave length of the waves). In the limit $K_r \to 1$ and $\Delta\varphi = 0$, equation (1.24) reduces to the expression given in Longuet-Higgins & Stewart (1964).

## 1.3 Reynolds stress tensor principal axes

The wave-induced components yield, in the Reynolds averaged Euler equations, a periodic (wave) Reynolds stress tensor of the second order, which is diagonal only for progressive waves. For two-dimensional partially-reflected waves, the Reynolds wave stress tensor is a matrix of the form

$$\begin{bmatrix} \overline{\widetilde{u}^2} & \overline{\widetilde{u}\widetilde{w}} \\ \overline{\widetilde{u}\widetilde{w}} & \overline{\widetilde{w}^2} \end{bmatrix}. \tag{1.25}$$

The density of the water $\rho$ is omitted since it is constant in our experimental conditions.

We can diagonalize the second-order tensor (1.25) to obtain the maximum and minimum principal Reynolds wave stresses in the $x - z$ plane, defined as

$$\widetilde{\sigma}_i = \frac{\overline{\widetilde{u}\widetilde{u}} + \overline{\widetilde{w}\widetilde{w}}}{2} \pm \sqrt{\left(\frac{\overline{\widetilde{u}\widetilde{u}} - \overline{\widetilde{w}\widetilde{w}}}{2}\right)^2 + \overline{\widetilde{u}\widetilde{w}}^2}, \tag{1.26}$$

with $i = \max, \min$ represent the maximum (sign $+$) and minimum (sign $-$) stress, respectively. At the first order, by means of equations (1.10–1.11–

1.13) we obtain:

$$\widetilde{\sigma}_i = \frac{gka_i^2}{\sinh(2kh)}\left(\frac{1+K_r^2}{2}\cosh\left[2k(z+h)\right] - K_r\cos(\theta_i+\theta_r)\pm\right.$$
$$\left[\left(\frac{1+K_r^2}{2} - K_r\cosh\left[2k(z+h)\right]\cos(\theta_i+\theta_r)\right)^2 + \right.$$
$$\left.\left.K_r^2\sin^2(\theta_i+\theta_r)\sinh^2\left[2k(z+h)\right]\right]^{1/2}\right). \tag{1.27}$$

We can also calculate the principal angle, which is the angle that the principal stresses form with $x$ and $z$. By definition, the principal Reynolds wave angle reads

$$\widetilde{\alpha}_p = \frac{1}{2}\tan^{-1}\left(\frac{2\overline{\widetilde{u}\widetilde{w}}}{\overline{\widetilde{u}\widetilde{u}} - \overline{\widetilde{w}\widetilde{w}}}\right). \tag{1.28}$$

The analytical form of $\alpha_p$ follows from straightforward substitution of all terms in equation (1.28):

$$\widetilde{\alpha}_p = -\frac{1}{2}\tan^{-1}\left(\frac{2K_r\sinh(2hk)\sinh[2k(h+z)]\sin\left(\theta_i+\theta_r\right)}{1+K_r^2-2K_r\cosh\left[2k\left(z+h\right)\right]\cos\left(\theta_i+\theta_r\right)}\right). \tag{1.29}$$

Analogously to the Reynolds wave stress tensor, we can define a Reynolds turbulent stress tensor, which involves turbulent velocities and reads:

$$\begin{bmatrix} \overline{\widetilde{u'u'}} & \overline{\widetilde{u'w'}} \\ \overline{\widetilde{u'w'}} & \overline{\widetilde{w'w'}} \end{bmatrix}. \tag{1.30}$$

In this thesis we do not explicit an analytical formulation for the turbulent fluctuations and stresses. However, the relation 1.26 yields:

$$\sigma_i' = \frac{\overline{\widetilde{u'u'}} + \overline{\widetilde{w'w'}}}{2} \pm \sqrt{\left(\frac{\overline{\widetilde{u'u'}} - \overline{\widetilde{w'w'}}}{2}\right)^2 + \overline{\widetilde{u'w'}}^2}, \tag{1.31}$$

with $i = \max, \min$. Following equation (1.28), the principal angle of the Reynolds turbulent principal stresses reads:

$$\alpha'_p = \frac{1}{2} \tan^{-1} \left( \frac{2\overline{\widetilde{u'w'}}}{\overline{\widetilde{u'u'}} - \overline{\widetilde{w'w'}}} \right). \tag{1.32}$$

# Chapter 2

# Experiments and methodology

## 2.1 Facility

A series of experiments were carried out in the Ocean-Atmosphere Interaction Flume (CIAO), located at IISTA (Andalusian Institute of Earth System Research) - Universidad de Granada. The wave flume is 16–m long and 1–m wide with rectangular cross-section, is designed for water depth of $\approx 70\,\mathrm{cm}$ and has two piston-type paddles (wavemakers) at the two ends. The two paddles can generate and absorb waves in both directions, with a wave period from 1 to 5 s and a wave height up to 25 cm, and are equipped with an active wave absorption system with a feedback control, in order to reach the desired reflective conditions. The description of the active absorption system and its principles of operation can be found in Lykke Andersen *et al.* (2016). A current-generation system, constituted by two pumps external to the CIAO, can supply longitudinal currents up to $0.75\,\mathrm{ms}^{-1}$ between the two paddles, in both directions. The upper part of the flume is closed by a wind tunnel, which has two fans in a closed-circuit system for wind generation up to $12\ \mathrm{m\,s}^{-1}$. On the roof of the wind tunnel, a rain generator is installed at a mid section of the flume and can supply rain with intensity between 75 and 300 mm h$^{-1}$. The four components (wave, wind, current and rain generators) work independently from each other, and the entire system is designed to study one precise condition or combinations of more. For the experimental activity of this thesis, we used the wavemakers to generate/absorb regular waves and the two fans of the wind tunnel for the superposition of wind to the paddle-generated waves. Current and rain generators were kept off during all the experiments.

A sketch of CIAO from different perspectives is shown in figure 2.1. Measurements of the wind speed were performed with a Pitot tube, which was far 9.2 m from paddle 1 and 6.8 m from paddle 2, at six different heights from the still water level to reconstruct the air velocity profile. Eight UltraLab ULS 80D acoustics wave gauges (US) were employed for water level measurements along the flume, in two different configurations: (i) configuration *a*, with a larger spacing between the US to cover the spatial variation of free water surface in the entire channel; configuration *b*, with a narrow spacing to analyse free surface in closer sections. Velocity under waves was measured with a two-component Laser Doppler Velocimeter (2D-LDV) by TSI Inc., with fiber-optics probe. The 2D-LDV was used to investigate the velocity profile in water between still water level and the bottom, in the range permitted by material obstacles. For some experiments, the LDV probe was set at the same measurement section varying the reflective conditions, while for others the probe was moved in the longitudinal direction to study the spatial variation of the velocity field maintaining similar experimental conditions, i.e. reflection parameters and paddle wave characteristics.

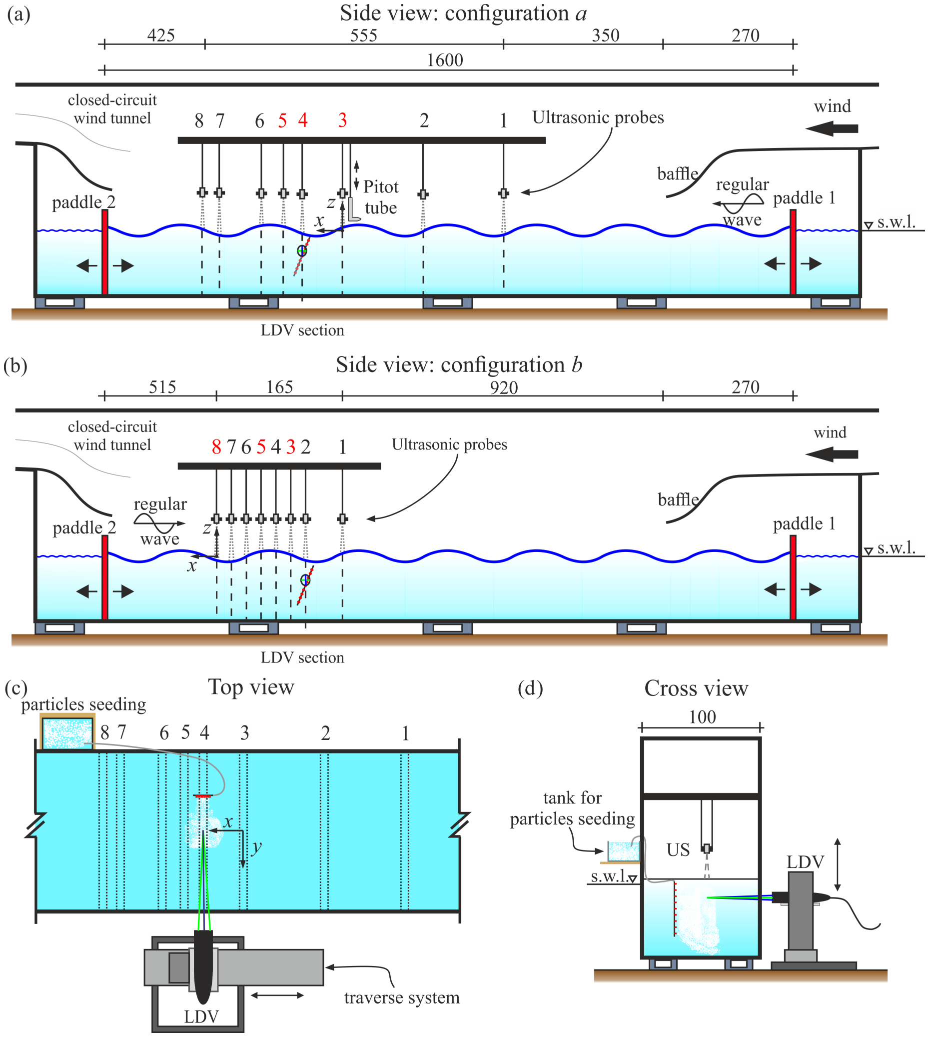

Figure 2.1: (a) Side view of the experimental set-up for larger US spacings (configuration *a*). (b) Side view of the experimental set-up for narrow US spacings (configuration *b*). (c) Top view of the flume (configuration *a*). (d) Cross view of the flume. No wind blockage was observed in proximity of paddle 2, indicating good performances of the closed-circuit wind tunnel.

## 2.2 Velocity field

### 2.2.1 Instruments and technology

A TSI two-dimension Laser Doppler Velocimetry (2D-LDV) was used to measure the velocity field for paddle waves and paddle waves with wind. An INNOVA70 Series water-cooled Air-Ion laser was used as source, with maximum power of 5 W. Ten points below the water surface were acquired along one measurement section for each test. An ISEL traverse system allowed remote-controlled displacements in longitudinal ($x$) and vertical ($z$) directions of the LDV probe, with possibility of manual movements along $y$. The LDV probe was horizontal, with the axis in crosswise ($y$) direction. The system measured two orthogonal components: horizontal velocity along $x$ through Channel 1 (Green light, wavelength $\lambda_g = 514.5\,\mathrm{nm}$) and vertical velocity along $z$ through Channel 2 (Blue Light, wavelength $\lambda_b = 488\,\mathrm{nm}$). Figure 2.2 shows a sketch of the LDV system.

Measurements were conducted in Non-Coincidence mode, which means that the particles detected from the two lights (Green and Blue) may differ. The power of the laser was set at 2.2 W for all tests. The data rate varied between hundreds to over one thousand hertz. For all experiments (except for one), the measurement section coincided with the position of one US, depending on the test. In this way velocities and water levels are obtained for the same section at the same time. Only in one case it was not possible to move the LDV probe below one US measurement section, for the finite range of motion of the traverse system.

Spherical glass particles with nominal diameter $D = 8 - 12\,\mu\mathrm{m}$ were used to seed the measurement volume during the tests in order to increase data rate and enhance data quality. The seeding system was composed by 9 small tubes displaced at different quotes attached to an inclined support, with injecting part oriented in $y$ direction. Tubes were connected to an external tank, fixed outside the flume above the water level, thus seeding was provided by gravity.

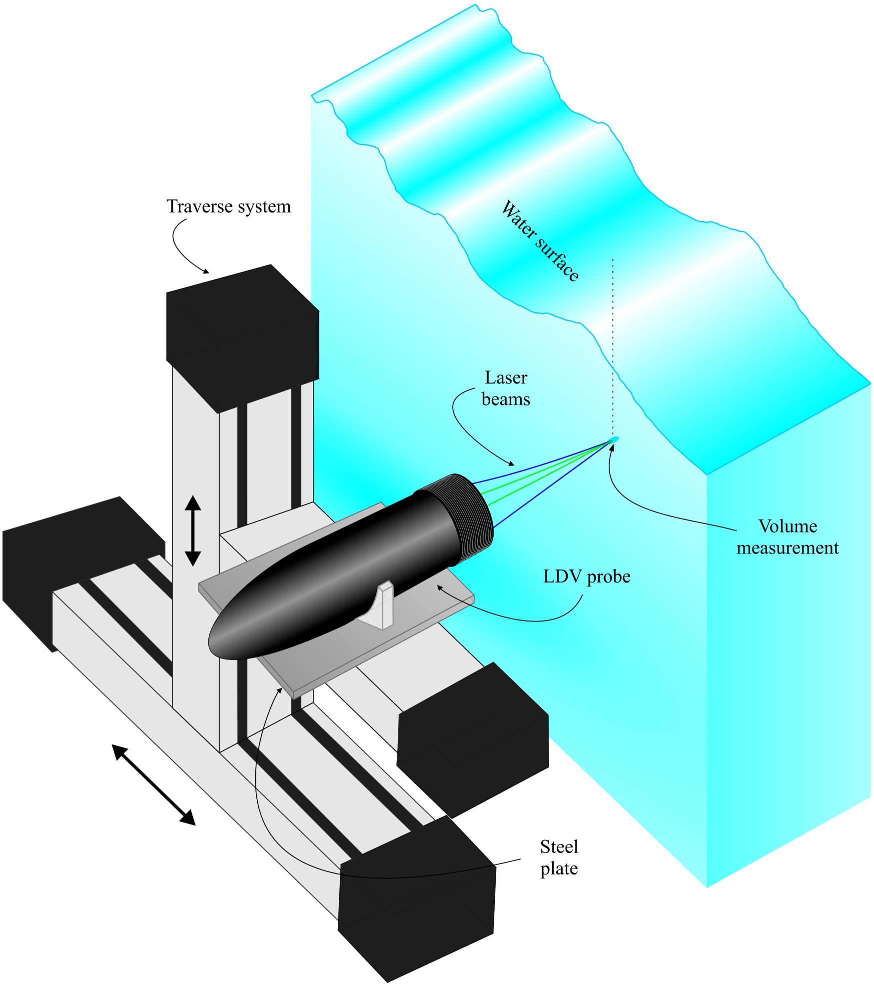

Figure 2.2: Positioning of the LDV system (probe and traverse) during measurements.

### 2.2.2 Uncertainty in velocity measures

Several sources of uncertainty can arise in the LDV system. First, the data rate is not constant. It causes in general a velocity bias, since particles with higher velocities have higher probability to cross the measurement volume. Another source of velocity bias is represented by an inhomogeneous distribution of tracer (in our case, the particles injected). We solved this type of velocity bias by interpolating the raw measured data with a fixed time interval.

Uncertainties can be also attributed to errors in the individual velocity measurements, occurrence of velocity gradients in the measurement volume, the presence of errors in the optical system, the resolution of the detector and the signal processing. These may be viewed as noise adding up to the wide bandwidth electric noise from stray light (reflections or scattering of laser light from walls, windows or optical components), the photomultiplier and the associated electronics. These effects are evaluated by the data sheet of the instrument, which quantifies the velocity accuracy in an error of less than 0.5% of measured velocity.

Another error may derive from the non-orthogonality between the laser probe and the crystal wall of the flume. The main effect is to underestimate or overestimate the velocity component, depending on the orientation of the rotation with respect to the real velocity vector. For a mainly 2D flow, it can be demonstrated that the expected uncertainty is (at most) $\approx 0.5\%$ of the measured value. Considering all the possible sources of error, an overall instrumental uncertainty less than 1% of the measured value is expected.

### 2.2.3 Measurement and signal processing

#### Pre-processing

In order to improve the performance and accuracy of the LDV system, a pre-processing of the signal is needed, mainly for two reasons: non-fixed data rate and outliers in the output signal.

As remarked in §2.2.1, a varying time interval between two subsequent measures causes velocity bias, and the problem is solved by interpolating the raw signal on a fixed time stamp. We choose, as the fixed sampling time interval, the inverse of the mean data rate (the ratio of the number measures to the sampling time), approximated to the third decimal.

The Flowsizer software (produced by TSI) is used to analyse the scattering of lights given by particles which cross the measurement volume and are captured by the optical system. The software takes advantage of several filters, which assess the quality of the received analog signal, in order to validate the acquisitions and obtain a good Signal-to-Noise ratio. The points validated are returned as velocity signals to the user. However, at very high data rate, outliers may overcome the software algorithm and some spikes appear. To avoid that problem and eliminate any outliers, the despiking method developed by Goring & Nikora (2002) and modified by Mori *et al.* (2007) is performed for LDV measurements.

### Triple decomposition technique

Horizontal and vertical velocities, measured by 2D-LDV and filtered in pre-processing, are analysed through a triple decomposition technique. Each velocity signal is split into 3 parts (see Hussain & Reynolds, 1970):

$$v(x,z,t) = \bar{v}(x,z) + \tilde{v}(x,z,\tau) + v'(x,z,t) \tag{2.1}$$

representing, in order, a mean, a periodic and a fluctuating component. The mean component is taken as the time average of the whole measurement:

$$\bar{v}(x,z) = \frac{1}{T_{acq}} \int_0^{T_{acq}} v(x,z,t)\mathrm{d}t, \tag{2.2}$$

where $T_{acq}$ is the sampling time for an acquisition point, and it is always a multiple of the paddle wave period $T$. Then, the periodic (organised) velocity is obtained by the phase average of the measured velocity, after subtracting the time average component:

$$\tilde{v}(x,z,\tau) = \langle v - \bar{v} \rangle = \frac{1}{N_w} \sum_{n=1}^{N_w} \big( v(x,z,\tau + nT) - \bar{v}(x,z) \big). \tag{2.3}$$

where $T$ is the regular wave period and $N_w$ is the number of waves recorded during one measurement.

The turbulent (fluctuating) component is calculated as the residual part after time and phase averaging:

$$v'(x,z,t) = v(x,z,t) - \bar{v}(x,z) - \tilde{v}(x,z,t). \tag{2.4}$$

### Velocity covariance

After the decomposition, the time average of the experimental correlations (covariances) between horizontal $u$ and vertical $w$ velocities, for fluctuating and periodic components, reads:

$$\overline{\widetilde{v}_l \widetilde{v}_m}(x,z) = \frac{1}{T}\int_0^T \widetilde{v}_l \widetilde{v}_m \mathrm{d}t, \tag{2.5}$$

$$\overline{\widetilde{v}_l v'_m}(x,z) = \frac{1}{T}\int_0^T \widetilde{v}_l v'_m \mathrm{d}t, \tag{2.6}$$

$$\overline{\widetilde{v'_l v'_m}}(x,z) = \frac{1}{T_{acq}}\int_0^{T_{acq}} \widetilde{v'_l v'_m} \mathrm{d}t, \tag{2.7}$$

with $l, m = 1, 2$ for, respectively, horizontal and vertical velocities. By definition, the mixed correlations are null, $\overline{\widetilde{u}_l v'_m} = \overline{\widetilde{v}_l u'_m} = 0$.

Covariance between horizontal and vertical velocity is not null for water waves under partial reflection conditions, and causes additional stresses and interactions that modify the global momentum transfer. The terms calculated through 2.5 represent the experimental evaluation of the wave-induced velocity covariance in our tests.

### Quadrant analysis

The quadrant analysis is a technique to get more information about momentum transfer from the turbulent boundary layer to the outer flow, and viceversa (Wallace, 2016). This technique consists of a characterization of the turbulent field by considering the permanence of the fluctuating velocities $u'$ and $w'$ in the four quadrants, defined by the sign the fluctuating

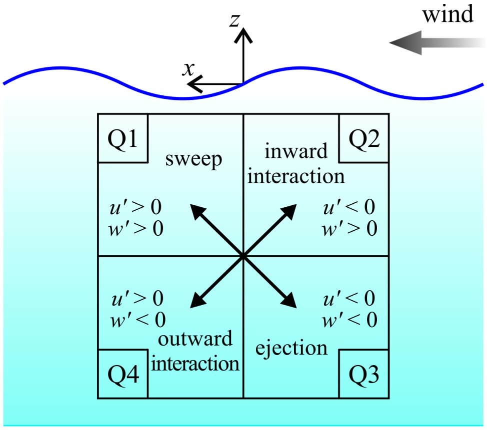

Figure 2.3: Turbulent velocities decomposition in 4 quadrants. Ejection and sweep are considered as the momentum transfer in the boundary layer with low-speed and high-speed fluids, respectively.

components. We make use of the definitions usually adopted in previous literature: (i) ejections are outward movements of fluid from the boundary at low speed; (ii) sweeps are high-speed movements of fluid towards the boundary. In particular, for our reference system, we have ejections when $u' < 0, w' < 0$ and sweeps when $u' > 0, w' > 0$ (see Figure 2.3). The other two possible conditions, $u' < 0, w' > 0$ and $u' > 0, w' < 0$, are defined in a more generical way as inward and outward interactions, respectively. Referring to the topic of this thesis, the quadrant analysis is conducted to get insight of turbulent Reynolds shear stresses both in air and water boundary layers in the presence of wind-generated waves (see, e.g., Longo & Losada, 2012; Longo, 2012).

Several studies observed that ejections and sweeps are the main contributor to the transfer of momentum and turbulent kinetic energy in the turbulent boundary layer (Kline *et al.*, 1967; Wallace & Brodkey, 1977; Li & Bou-Zeid, 2011). In order to determine the dominant motion, we split the contribution of each quadrant to the total shear stress. The event-averaged shear stress is defined as

$$S_j = \frac{1}{N_j} \sum_{i=0}^{N_j} \left(u'w'_i\right)_j, \quad j = 1, \ldots, 4, \tag{2.8}$$

where $N_j$ is the number of samples belonging to the $j$th quadrant. The average stress of the $j$th quadrant is

$$\overline{u'w'}_j = \frac{1}{N} \sum^{N_j} \left(u'w'\right)_j, \quad j = 1, \ldots, 4 \tag{2.9}$$

where $N$ is the total number of samples. Equation (2.9) can also be written as

$$\overline{u'w'}_j = \frac{N_j}{N} S_j, \quad j = 1, \ldots, 4 \tag{2.10}$$

where the ratio $N_j/N$ is the relative permanence of the event in the $j$th quadrant, and the total shear stress results

$$\overline{u'w'} = \sum_{j=1}^{4} \overline{u'w'}_j. \tag{2.11}$$

The introduction of a threshold for the analysis of the results can be helpful in the description of bursting, which includes highly-intermittent and also explosive events which carry most of the momentum from the boundary layer to the mean flow (and vice versa). We consider the events that satisfy the following relation:

$$u'w' > M u'_{\text{rms}} w'_{\text{rms}}, \tag{2.12}$$

where the parameter $M$ determines the threshold. Considering a fixed threshold, the concentration of the $j$th quadrant is

$$C_M^j = \frac{1}{N} \sum_{i=1}^{N} \phi_{M,i}^j, \tag{2.13}$$

with the coefficient $\phi^j_{M,i}$ defined as

$$\phi^j_{M,i} = \begin{cases} 1 \,\text{if}\, u'w' > M u'_{\text{rms}} w'_{\text{rms}} \,\text{and belongs to the}\, j\text{th quadrant} \\ 0 \,\text{otherwise} \end{cases} \tag{2.14}$$

Thus, we can define the phasic-averaged Reynolds shear stress for the $j$th quadrant as

$$\left(\widehat{u'w'}\right)^j_M = \frac{\sum_{i=1}^N \left(u'w'\right)_i \phi^j_{M,i}}{\sum_{i=1}^N \phi^j_{M,i}}, \tag{2.15}$$

and the time-averaged Reynolds shear stress as

$$\left(\overline{u'w'}\right)^j_M = \frac{1}{N} \sum_{i=1}^N \left(u'w'\right)_i \phi^j_{M,i} = C^j_M \left(\widehat{u'w'}\right)^j_M . \tag{2.16}$$

Equation (2.16) can be expressed as stress fraction in non-dimensional form

$$F^j_M = \left(\overline{u'w'}\right)^j_M / \overline{u'w'}, \tag{2.17}$$

which yields

$$\sum_{j=1}^4 F^j_0 = 1. \tag{2.18}$$

## 2.3 Free surface and water waves

### 2.3.1 Instruments and technology

Eight ultrasound acoustic sensors (USS635, UltraLab ULS 80 D, General Acoustics), here also called US, are used along the flume to measure the water surface level. The working range of US is 60 to 350 mm, with a repetition rate of 75 Hz, a technical nominal resolution of 0.18 mm and reproducibility equal to ±0.15% of the measured value. Each measurement is the average level over the area of intersection of the ultrasonic conic beam (a circular area with a few centimeters of diameter) and the free surface. A scheme of a working US is shown in figure 2.4(a).

The instrument is set to get an analog output between $0-10\,\mathrm{V}$. The relation between voltage (in V) and distance (cm) is linear: $z(V)=a+C_C\cdot V$, where $a$ is the offset, $C_C$ the angular coefficient of the calibration curve and $V$ is the signal (in volts). The calibration points are obtained by setting the US probe at a known height, measuring the output for ten seconds and estimating the mean value of the output voltage, at four vertical coordinates for each US. An example of the resulting calibration parameters and deviations of the measured points with the linear interpolation curve is shown in figures 2.4(b–c). Deviations are always within the instrumental error. The software used for data acquisition (calibration and experiments) was LabVIEW.

The use of ultrasound probes presents the advantage to be non-invasive, i.e. there is no direct contact between the measurement field (water domain) and the instrument. This is important because in this way we are sure that the presence of US does not affect the measurements, and for that reason US probes are chosen for water level measures in our experiments instead of other typical instruments, such as resistance probes. However, US probes may have also some disadvantages: (i) temperature gradients can influence the propagation speed of the ultrasonic wave packets, and it can affect the measures; (ii) when the probe is not sufficiently vertical or the water level is too steep, the echo of the ultrasonic wave packets can be lost; (iii) the US probe measures the distance between the probe and the water surface, but does not identify the presence or the absence of spray and bubbles. The first problem was not present during the execution of our experiments since the working range of the instrument ($6-35\,\mathrm{cm}$) is sufficiently limited to avoid strong temperature gradients. Part of the second issue was solved by verifying the verticality of the probes just before the realization of the experiments. It was not possible to control the steepness of random waves, but a check of the signal after the despiking technique assured that the water level conditions did not affect the quality of the measurements. The last problem was avoided since micro-breaking of the water waves, which happened occasionally for strong wind conditions, has a negligible entrainment of air. Other possible sources of measurement errors are addressed during the pre-processing of the data.

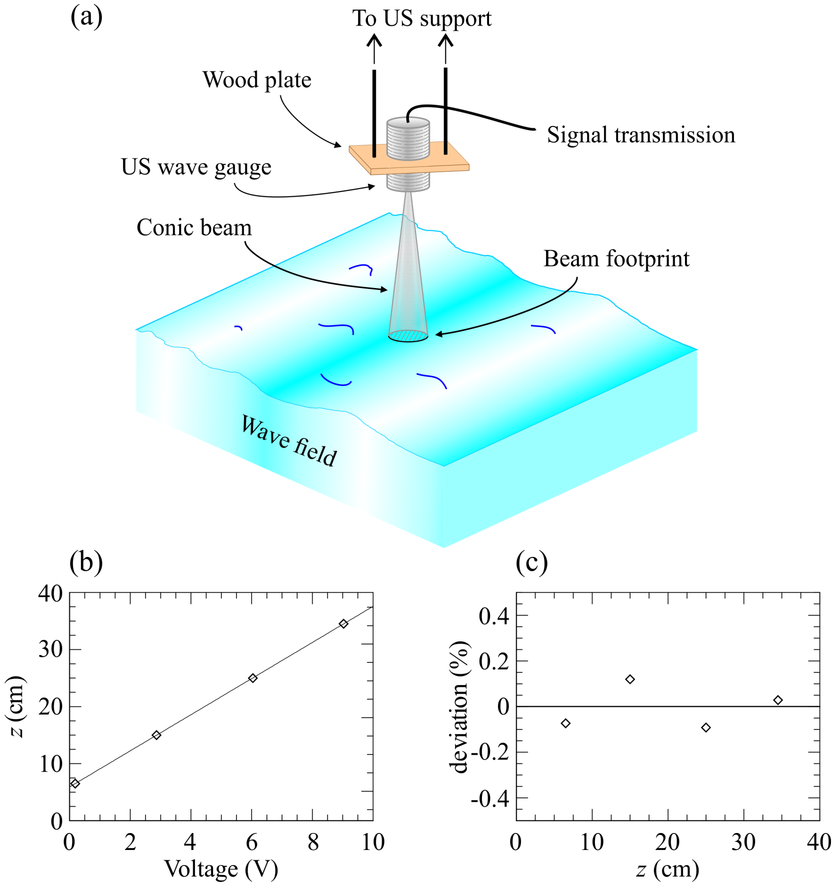

Figure 2.4: Schematic description of an ultrasound probe (US). (a) A working US in the field of measurement . (b) A US calibration curve, measured points (diamonds) linearly interpolated (solid line). (c) Deviations of the experimental points from the calibration curve, in percentage.

For the experimental activity, the eight US were displaced in two configurations along the wave flume: the first had a larger spacing between the US, and aimed at measuring the spatial variation of the wave field in the entire channel (configuration *a*); the second, with a narrow spacing, aimed to analyse the wave field in closer sections (configuration *b*). Each US had its own support, a transversal steel cylinders with diameter $\phi \approx 4\,\text{cm}$ positioned 30 or 90 cm above the still water level. The description of the wind profile distortion due to US supports, in the range considered for air velocity measures ($0 - 30\,\text{cm}$ above the still water level), concerns the air velocity profile and is discussed later in this Chapter.

### 2.3.2 Uncertainty in free surface measures

The uncertainty on US derives mainly on its reproducibility. In the working range $60 - 350\,\text{mm}$, the maximum error due to reproducibility and technical resolution is $0.0015 \times 360 + 0.18 = 0.72\,\text{mm}$. Another source of error can be the misalignment between the US probe and the vertical. It can be shown that an inclination of 1°, which is feasible in laboratory experiments, yields at most to an overestimation of $350(1/\cos 1^\circ - 1) = 0.05\,\text{mm}$. By considering all the possible sources of error, the maximum instrumental error which we expect in our experiments is $\approx 0.8\,\text{mm}$.

### 2.3.3 Data analysis

#### Pre-processing

US are suitable tools for detecting water surface elevation, since they are non-invasive and have good accuracy. However, a pre-processing of the raw signal is always recommended to improve the quality of the acquired data.

US raw signals can be affected by outliers due, for example, to the proximity of the probes and to the steepness of the water surface, which are common conditions for tests in wave channels. To avoid this inconvenient in our data, the raw signal acquired during the experiment was filtered in two steps: first, a moving-average was applied in the time domain, then the same despiking algorithm used for LDV measurements was used in order to remove the remaining outliers.

### Reflection analysis

Reflection plays a relevant role in water waves, in particular during laboratory activities, where the finite length of the experimental apparatus may have a strong influence on the wave field. In general, it is more appropriate to speak about partial reflection, since during experiments usually part of the wave energy is absorbed by passive or active systems.

The evaluation of the partial reflection conditions during the experiments is an essential part of the work of this thesis, because we want to investigate the influence that different reflection conditions exert both on velocities and levels of the flow field. Reflection parameters are estimated by using the Baquerizo's method (see Baquerizo, 1995). It is an extension of the method by Mansard & Funke (1980) and separates incident and reflected waves by means of three US set in different positions along the flume. For certain wave gauges spacings (not discussed here), the method may have large uncertainties, but the configurations which could give that problems were known and avoided. The three sensors used to estimate the reflection parameters were taken adjacent to the LDV measurement section. The method can be applied to regular and irregular waves, and for irregular waves the analysis is based on a narrow band around the peak frequency ($0.5 < f/f_{peak} < 1.5$) of the signals, which is the frequency with the highest power spectral density. The software used for the reflection analysis evaluates: i) the reflection coefficient $K_r$, defined as the ratio between the reflected and the incident wave energy; ii) the phase shift $\Delta\varphi = \varphi_i - \varphi_r$, which represents the difference between the initial phase of the incident and the reflected waves; iii) the incident wave height $H_i$.

For progressive waves (i.e., in the absence of reflection), $K_r$ and $\Delta\varphi$ are trivially null. In case of perfect reflection, for instance when waves impact on a fixed impermeable vertical wall, boundary conditions yield $K_r = 1$ and $\Delta\varphi = 0$, which means that one antinode is at the wall section. A non-null phase shift $\Delta\varphi \neq 0$ causes a shift of nodes and antinodes along $x$, see equation (1.12). In our application of the Baquerizo's method, the phase shift reveals the distances between the first US used for reflection analysis and the nearest antinode.

In all the present experiments with waves generated by paddle and wind (intrinsically are random waves), the analysis of the spectrum gave $f_{peak} \approx 1/T$ in the limits of data uncertainty and resolution, confirming that the process is dominated by the paddle waves with a minor contribution of the wind generated waves. The wave period $T$ is evaluated by spectral analysis and the wavelength $L$ derives from the linear dispersion relation $\omega^2 = gk \tanh kh$. We were aware of the fact that the wave speed (or length) may be affected by wind or wind generated current, but the comparison between the theoretical model, whose wave length $k$ was calculated from the linear dispersion relation, and the experimental measurements suggested that the linear dispersion relation was sufficiently accurate to be used in our analysis.

### Periodic and wind wave characteristics

The analysis of the paddle- and wind-waves characteristics can be performed in time and frequency domain.

In time domain, the signal is split into three components (a time-averaged, a phase-averaged and a fluctuating component), using the triple decomposition technique described in §2.2.3. The mean (time-averaged) component represents residual currents developed in the wave flume (even in the absence of wind), the phase-averaged contribution is attributed to the action of the periodic (paddle) wave, and the fluctuating contribution is attributed to the action of the wind. A zero – (up)crossing analysis is performed taking the mean water level as zero. In this way we can obtain the average, the root mean square, the significant, the minimum and the maximum wave height and period, for paddle waves and wind waves separately.

In frequency domain, it is not necessary to apply the triple decomposition technique as before. The Fast Fourier Transform of US data is used to have the spectrum of the signal, i.e. the distribution of the wave

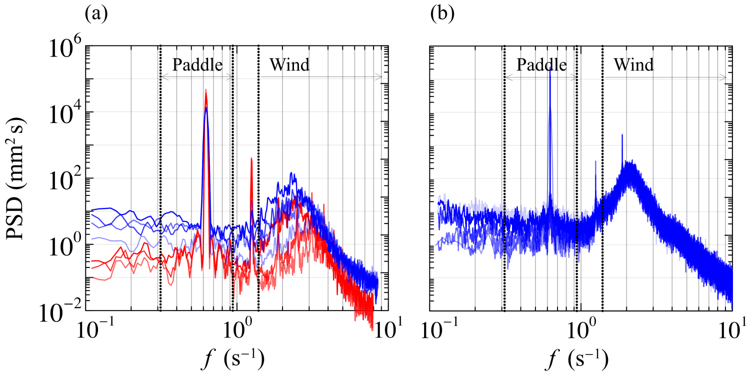

Figure 2.5: Paddle and wind waves spectra. The periodic component is in the frequency band $0.5 < f/f_{peak} < 1.5$, while the fluctuating component is in the frequency domain $f > 2.22\,f_{peak}$. (a) Paddle waves plus following wind (PpW), in blue experiments PpW1–4 (active absorption) and in red experiments PpW5–7 (passive absorption). (b) Paddle waves with opposing wind (PoW), experiments PoW1–5.

energy density over the frequency. In this case, paddle waves and wind waves are separated by using a spectrum filter. In particular, the periodic component is obtained by filtering the spectrum in the frequency band $0.5 < f/f_{peak} < 1.5$, while the fluctuating component is extrapolated by a high-pass filter with a threshold of $2.22\,f_{peak}$. In figure 2.5, it is shown the spectrum windowing for paddle and wind-generated waves, with no overlap between the two components. Following this procedure, we can estimate wave height, crest, trough and period of the paddle waves and the wind waves.

From the comparison between the statistical (in time) and spectral (in frequency) analyses, the differences individuated were not significant. Thus, the results of the spectral analysis was used to characterize wave height and period.

Also the mean water level can be evaluated experimentally, either for filtered or unfiltered signals. The time average of US signal yields the experimental mean water level $\overline{\zeta}$, which is compared with the theoretical model derived in §1.2.1.

### Theoretical phase celerity of wind-generated waves

The theoretical phase celerity of a potential wave at the first order is represented by the linear dispersion relation $\omega^2 = gk \tanh kh$. Once the angular frequency $\omega$ is known, $k$ is obtained from the dispersion relation and the phase celerity computed as $c = \omega/k$. Since the spectral analysis allows the separation of the wind from the periodic component, as a first approximation we assume that wind-generated waves propagate with the peak frequency of the high-pass-filtered spectrum (the periodic component is disregarded).

However, in order to use the linear dispersion relation derived from potential theory, we must be sure that the hypotheses of the linear wave theory still hold. This is not true for random waves, so the previous dispersion relation is corrected considering non-linear effects of sheared currents measured in the wave flume. To include the effects of the mean flow, the phase celerity is calculated according to the model by Swan & James (2000). They developed an analytical relation through a perturbation analysis, where the wave steepness $\epsilon = ka$ is the small parameter determining the power series expansions. The technique is valid for small amplitude waves and for all current profiles, and deals with weak currents. For the experiments of this work, the current profile is approximated by a third-order polynomial as:

$$\overline{u}(z) = Az^3 + Bz^2 + Cz + D, \tag{2.19}$$

where the coefficients $A$, $B$, $C$ and $D$ are obtained from best fitting of the experimental velocities. In equation (2.19), no-slip condition is imposed at the bottom. For the particular case represented by equation (2.19), the phase celerity calculated from Swan & James (2000) results:

$$c = \sqrt{\frac{g}{k} \tanh kh} + D + c_1, \tag{2.20}$$

$$c_1 = -\frac{C}{2k} \tanh kh + \frac{B}{2k^2} - \frac{3A}{4k^3} \tanh kh - \frac{C}{4k \tanh kh} \operatorname{sech}^2(kh), \tag{2.21}$$

where $c_1$ is a second order correction due to non-linear interactions between wave and current.

### Experimental phase and group celerities of wind waves

The experimental phase celerity of the wind waves, as well as the group celerity, can be evaluated through the US signals. The cross-correlation technique reported in Longo (2012) is used. The temporal lag $\Delta\tau$ between two adjacent sensors is evaluated from the highest peak of the cross-correlation function. Since the distance $\Delta x$ between the two sensors is known, the phase celerity between two probes is computed as $c_{\exp}(x) = \Delta x/\Delta\tau$. It represents the averaged value of the phase celerity (with $x$ representing the medium point) between the two US.

The experimental group celerity is calculated from the Hilbert transform of the cross-correlation function between two US signals. For narrow-bandwidth wind waves, the time lag of the wave group $\Delta\tau_g$ refers to the maximum of the cross-correlation envelope (see Bendat & Piersol, 2000). Then, the experimental wave group celerity is evaluated as $c_{g,\exp}(x) = \Delta x/\Delta\tau_g$ (see figure 2.6).

In order to use the cross-correlation technique, the following conditions should hold: i) a strong coherence is reached between signals of two adjacent probes (as a rigid translation of waves with constant shape); ii) non-linear interactions are negligible. These two assumptions are respected also for wind waves, within the experimental uncertainties, when US spacing is sufficiently limited (of the order of half the wind wave length). That condition has been verified by comparing the probe spacing $\Delta x$ with the wind wave length $L_{peak}$ associated to the peak frequency, assuming as an approximation the linear dispersion relation.

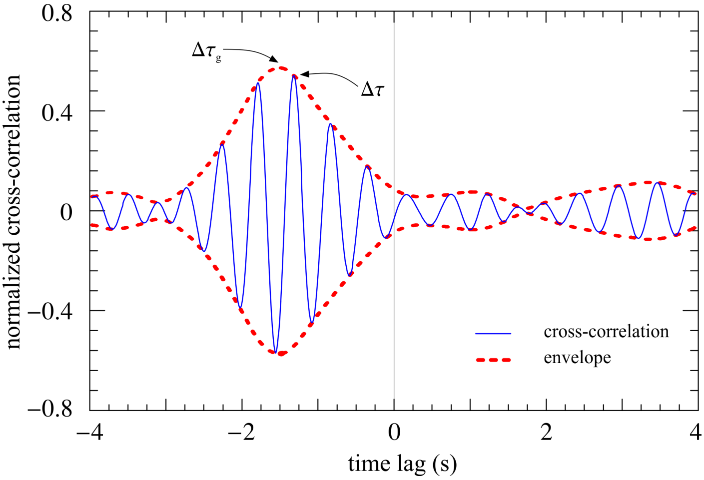

Figure 2.6: Normalised cross-correlation (solid line) between two subsequent US measurements for one of the experiments, and the envelope (dashed line). $\Delta\tau$ is the time lag of the cross-correlation function, to be used for the experimental phase celerity evaluation, and $\Delta\tau_g$ is time lag of the envelope (see Bendat & Piersol, 2000).

## 2.4 Wind

A Pitot tube was installed approximately at a mid section of the flume to measure four wind velocity above the free water surface. The signal was acquired for $\approx 60\,\mathrm{s}$ with a data rate of 1 kHz. For each wind velocity, six points were measured in the vertical coordinate $z$, whose zero is the still water level. Four values of rotation rates (revolutions per minute, RPM = 40, 60, 80, 100%) of the wind generators, controlled by a software, are converted in wind velocity measured by the Pitot tube (in $m\,s^{-1}$), at each vertical point.

During some initial experiments, the US supports were at 30 cm above the still water level (condition US-down). As wind approaches the quote of the US supports, the resulting air velocity profile diverges from the expected log-profile of air blowing over water. Thus, for the following experiments, the supports were located at 90 cm above the still water level, where their presence was much less significant (condition US-up). The air speed profiles for the two cases are shown in figure 2.7.

The air velocity shows a logarithmic profile for the US-up condition, while the US-down condition has a log-profile only close to the air-water interface. The log-law used for interpolation is the Prandtl-Karman distribution $U(z) = u_{*a} \log(z/z_0)$, where the parameters $u_{*a}$ and $z_0$ are the friction velocity and the aerodynamic roughness length, respectively. Since most of the interaction processes take place at the air-water boundary layer, i.e. in proximity of water, we choose $u_{*a}$ to characterize the wind velocity according to the log-law distribution. The logarithmic profile shows good agreement with the measured points and $u_{*a}$ looks representative for the wind speed in both US-down and -up conditions (see figure 2.8). For some experiments, a different value of RPM was chosen for wind generation. In that case, the reference velocity was calculated by linear interpolation from the two closer values.

The uncertainty in the measurements of the Pitot tube derives from the formula used to obtain the air velocity $U$:

$$U = C_c \sqrt{V - V_0}, \tag{2.22}$$

where $C_c = 14.267\,\mathrm{m\,s^{-1}V^{-1}}$ is the calibration coefficient, $V$ (in volts) gives the differential pressure when wind is generated, and $V_0$ (in volts) is the Pitot signal when the wind generator is off. If we assume $C_c$ as a constant, we calculate the uncertainty propagation on $U$ as:

$$\frac{\Delta U}{U} = \frac{1}{2}\left(\frac{\Delta V + \Delta V_0}{V - V_0}\right), \tag{2.23}$$

where $\Delta U$, $\Delta V$ and $\Delta V_0$ are uncertainties on $U$, $V$ and $V_0$, respectively. If we estimate $\Delta V$ and $\Delta V_0$ from the standard deviation $\sigma$ of the signal with a probability fixed at 95%, we have $\Delta V = 2\sigma_V$ and $\Delta V_0 = 2\sigma_{V_0}$. The standard deviation is calculated from ensemble average of the signal, with 1000 values for each ensemble. The relative uncertainty for all the measured points, with different velocity and elevation, are reported in Figure 2.9. It is

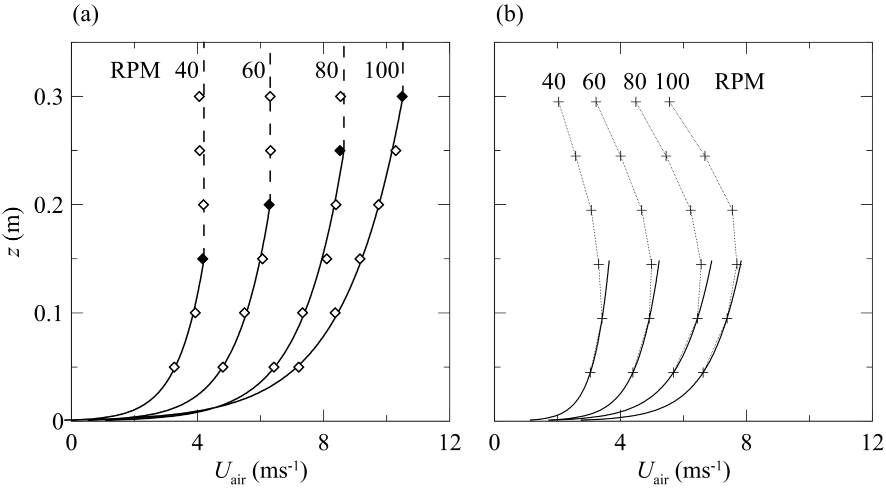

Figure 2.7: Velocity profile for different rotation rates: RPM = 40, 60, 80, 100% of the maximum rotation rate of the two fans which generated wind (RPM stand for "revolutions per minute"). (a) Air velocity profile with US supports 90 cm above the still water level (US-up). Solid lines represent the wind-log profile, while the dashed lines are the asymptotic velocities (uniform above the log-profile). Diamonds represent experimental values; filled symbols indicates the vertical coordinate where the log-profile stops and the constant profile starts. (b) Air velocity profile with US supports 30 cm above the still water level (US-down). Solid lines are the log-profile (considering only the two points closer to the water); symbols are experimental values. The log-law used for both figures is the Prandtl-Karman distribution $U(z) = u_{*a} \log(z/z_0)$, where $u_{*a}$ is the friction velocity and $z_0$ the aerodynamic roughness length.

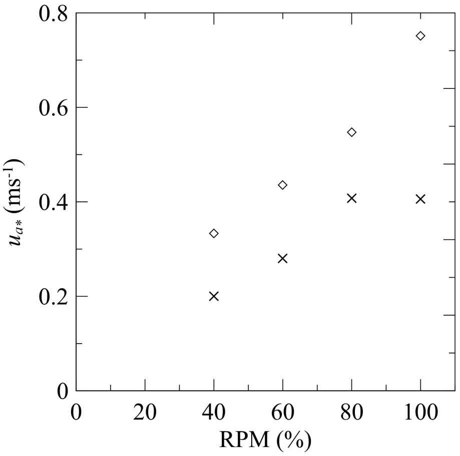

Figure 2.8: Estimated friction velocity $u_{*a}$ as a function of the rotation rate. Symbols represent experiments: diamonds are estimated in US-up condition, while crosses in US-down condition.

evident that uncertainties are bigger near the water surface for US-up, while for US-down (where we expect more fluctuations near the US supports) uncertainties are bigger at $z \approx 30\,\mathrm{cm}$. The mean relative uncertainties on the measured value for US-up and US-down are 8% and 15%, respectively.

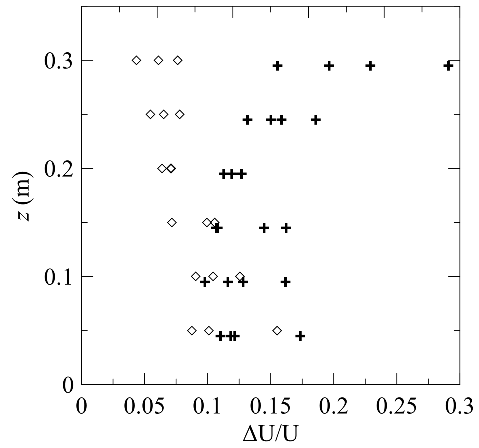

Figure 2.9: Relative air velocity uncertainty $\Delta U/U$ as function of the height above the still water level $z$. Diamonds represent US-up condition, while crosses represent US-down condition.

## 2.5 Scalings

### 2.5.1 Dynamic scaling

A correct dynamic scaling between laboratory (the model) and field (the prototype) requires the analysis of the similarity. The problem we are analyzing can be described in terms of nine variables: velocity, length, time, density, viscosity, tension surface, pressure, fluid compressibility and gravity acceleration. A group of three of the variables are independent and the problem can be expressed as a function of six non dimensional groups, namely Reynolds, Froude, Weber, Strohual, Euler, Mach numbers (see, e.g., Massey, 1971). The similarity requires the equality of these groups between the model and the prototype, hence three degrees of freedom are left. However, by using water in the laboratory experiments and in the presence of the same gravity acceleration, five constraints are added (viscosity, density, tension surface, bulk compressibility have the same values if dealing with the same fluids in the model and in the prototype) and the complete dynamic similarity is forbidden. A partial similarity is achieved by neglecting Reynolds number in the hypothesis that it has minor effects (especially in the air boundary layer), neglecting the Weber number in the hypothesis that curvature of the air-water interface is limited (i.e., there is a limited steepness $ka$ of the waves), neglecting the Mach number in the hypothesis that aerated breaking does not occur. In these conditions a Froude similarity can be adopted, with a length and a pressure scales equal to $\lambda$, a velocity and a time scales equal to $\sqrt{\lambda}$. Strouhal and Euler similarity is also satisfied. By assuming that $\lambda = 1 : 16$, an incident wave height $H_i = 5\,\mathrm{cm}$ and period $T = 1.6$ (a laboratory condition used in this thesis) is modelling a swell with height $H_i = 0.80 \pm 0.02$ m and $T = 6.4$ s ruffled by a local wind of 38 $\mathrm{m\,s^{-1}}$.

We notice that the Reynolds and the Weber number independence is not exactly fulfilled, and some scale effects are expected in transforming the experimental outcomes into field values, with a distortion larger for decreasing length scale $\lambda$. Also the Mach number irrelevance is not guaranteed in the presence of breaking or micro-breaking, possibly with air inclusion in the water.

We think that uncertainty in reflection conditions in the field (close to the coast) and directional waves could outweigh the scaling errors, and that laboratory experiments are still a good approximation of what happens in the field, even though it is out of the scope of this thesis to conduct a rigorous analysis on that topic.

### 2.5.2 Scales

We choose to scale all velocities with respect to $H_t T^{-1}$, where $H_t$ the total wave height and $T$ is the period of the regular wave. When LDV probe is co-located with a wave gauge (all tests except for one), $H_t$ represents root mean square value $H_{\mathrm{rms}}$ from the statistics of the corresponding sensor. For the other cases (different LDV sections), the total wave height $H_t$ is evaluated as (see Vílchez *et al.*, 2017; Baquerizo & Losada, 1999*b*; Baquerizo *et al.*, 1997):

$$H_t = H_{i,\mathrm{rms}} \sqrt{1 + K_r^2 + 2K_r \cos(2kx + \Delta\varphi)}, \tag{2.24}$$

where $H_{i,\mathrm{rms}}$ is the root-mean-square height of the incident wave.

For some experiments, the theoretical and experimental mean water levels $\overline{\zeta}$ are scaled with $a_i^2 k K_r$, where $a_i = H_i/2$ is the incident wave amplitude, in order to obtain a non-dimensional wave amplitude equal to 1.

## 2.6 Uncertainties

Quantifying errors and uncertainties related to measurements is crucial in research activities, especially in laboratory. In this work, we evaluate uncertainty for theoretical relations and for experimental acquisitions in two different ways: i) an ensemble average for measured data, ii) a Montecarlo simulation for analytical expressions.

### 2.6.1 Uncertainty of the measured data

Free surface levels are acquired during each LDV measurements, hence a series of ten independent measures for each experiments is available. It yields the evaluation of the statistical estimators (mainly average and variance) for the parameters of interest as ensemble averages. This procedure is followed for wave characteristics and also for reflection parameters.

For the data referred to single horizontal and vertical velocities, we split the sample into ten sub-samples, with the statistical estimators evaluated as ensemble average. For velocity correlation (which gives normal and shear stresses), we consider the product between horizontal and vertical velocities as a new variable, then follow the same procedure of a single velocity measure. The mean values are used as best estimators for the theoretical curves.

### 2.6.2 Uncertainty of the theoretical values: the Montecarlo simulation

The theoretical model developed in Chapter 1 reports the analytical form of the investigated quantities, i.e. the water level, velocities and stresses. For all the mathematical relations, the confidence interval is evaluated through a Montecarlo simulation with a population of $10^4$ samples.

In applying Montecarlo analysis to our experiments, gravity acceleration $g$ and wave number $k$ are considered as constant values, while reflection parameters ($H_i$, $K_r$ and $\Delta\varphi$) and $h$ are considered stochastic with a Gaussian distribution. Mean and variance of the reflection parameters are related to the average and standard deviation of the measured values, respectively (uncertainty evaluation for experimental values is treated in §2.6.1).

## 2.7 Realization of the experiments

The experimental study covers the following cases in a two-dimensional wave field: only-Paddle waves (P), Paddle-plus-Wind waves propagating in the same direction (PpW) and Paddle-opposing-Wind waves (PoW). Table 2.1 describes the main characteristics of the experiments. Several reflective conditions, wind velocities and paddle waves were tested to obtain a broad range of data. However, the characteristic of each experiment did not change during one acquisition. Each experiment started after reaching a stationary condition, and lasted 330 s.

During the P experiments, only the two paddles were activated to generate and absorb either a first or a second order Stokes wave. For some experiments, the reflective conditions imposed to the system varied and the LDV probe position was fixed. For others, the reflective conditions were fixed and the LDV probe position was changed, in order to investigate the spatial variation of the velocity field. One experiment was realized with a passive absorption system (a dissipative linear beach), due to a temporary default of the active absorbing system.

For PpW waves experiments, a first order Stokes wave was generated and absorbed, and wind varied for each test. For some tests, a passive absorption system was used to change randomly the reflective conditions. The LDV section was maintained in the same position for all the experiments. The protocol of the experiments was the following: the two wavemakers were activated first, and the two fans were turned on after that a station-

| Expt | Main characteristics |
|---|---|
| Paddle | $1^{\mathrm{st}}/2^{\mathrm{nd}}$ order paddle wave, active/passive absorption, different $K_r$, same LDV section.<br>$1^{\mathrm{st}}$ order paddle wave, active absorption, same $K_r$, different LDV section. |
| Paddle plus Wind | $1^{\mathrm{st}}$ order paddle wave, active/passive absorption, same $K_r$, different wind, same LDV section. |
| Paddle opposing Wind | $1^{\mathrm{st}}$ order paddle wave, active absorption, different $K_r$, same wind, same LDV section.<br>$1^{\mathrm{st}}$ order paddle wave, active absorption, same $K_r$, same wind, different LDV section. |

Table 2.1: General description of the experiments.

ary wave field was obtained (a few minutes). US and LDV acquisitions were started only when both wavemakers and wind flow were active and stable.

All the PoW experiments had the same wind conditions. The paddle wave was always monochromatic with constant period and height. For some experiments, the reflective conditions fixed and the LDV probe section was changed along the channel. For other experiments, the reflective conditions imposed to the system varied but the LDV section was fixed. The same protocol already described for PpW experiments was followed. In addition, in the PoW experiments the acquisition of the US signals started well before the activation of the fans, in order to observe the evolution of the water surface (including the reflection parameters) with and without wind.

# Chapter 3

# Paddle waves and paddle waves plus following wind

In this Chapter, only-paddle waves and paddle waves ruffled by wind blowing in the same direction of propagation of the waves are studied. The waves propagate on a flat bottom, are non-breaking and regular. The analysis conducted here is based on the observation of the free surface displacement and the fluid velocity.

Free surface elevation measurements are used for data analyses and comparison. A reflection analysis necessary to obtain the reflection parameters is conducted on the basis of free surface data in three sections, following the method described in §2.3.3. A phase average of the free surface yields the wave shape for the different experiments. By high-passing the free surface elevation, the separation between wind waves and swell is obtained and the statistics for wind waves are performed and analysed. The mean water level, which is derived theoretically in §1.2.1, is compared agains the one obtained from the experiments.

Velocity data collected through the LDV technique are used for several analyses. The mean horizontal and vertical velocities are calculated by time-averaging the LDV data over an integer number of waves. An out–of–quadrature of the periodic (wave) velocity components derived from the theoretical analysis of Chapter §1; is experimentally investigated and confirmed. Reynolds wave normal stresses are also analysed and compared to the theoretical values. The Reynolds turbulent normal and shear stresses are calculated from the fluctuating components of the velocity, and a quadrant analysis is performed to characterize some features of the turbulent structure. The Reynolds wave stress tensor is studied to compare the measured and theoretical principal stresses and the angle of the principal axes, while the Reynolds turbulent stress tensor is estimated, with the computation of the principal stresses and the angle of the principal axes.

A discussion on the results closes the Chapter.

## 3.1 Experiments

The experiments were conducted in the CIAO of the IISTA, Universidad de Granada. For these experiments, only-paddle and wind-plus-paddle generated waves were analysed, with air blowing in the same direction of paddle waves propagation (defined as "following wind"). The control system of the wave generator was used to change the reflection coefficient and the phase shift between incident and reflected components.

A Pitot tube was used for measurements of the wind speed above the free surface, while water surface levels were acquired with eight ultrasound probes located along the flume. In the water side, fluid velocities were measured with the fiber-optics probe of a two-component Laser Doppler Velocimeter. The facility and the instruments used for the acquisitions are described in detail in Chapter §2.

The experiments analysed in this Chapter are listed in Table 3.1, and the parameters were obtained through the statistical analysis of the free surface measurements and reflection analysis.

Paddle waves (P) and paddle waves with following wind (PpW) were generated in the wave flume for a total of eighteen experiments.

First, eleven P experiments were conducted. Tests P1–7 were carried out with the larger US spacings configuration represented in figure 2.1($a$), while the remaining four tests (P3$a$–$e$) were conducted with the narrower

| Expts | $u_{*a}$ ($\mathrm{cm\,s^{-1}}$) | $x$ (cm) | $H_i$ (cm) | $H_t$ (cm) | $T$ (s) | $K_r$ | $\Delta\varphi$ (rad) |
|---|---|---|---|---|---|---|---|
| P1 | 0 | 70 | $5.5 \pm 0.1$ | $6.1 \pm 0.1$ | 1.6 | $0.11 \pm 0.01$ | $3.14 \pm 0.04$ |
| $2^p$ | 0 | 76 | $7.5 \pm 0.3$ | $8.6 \pm 0.1$ | 1.6 | $0.33 \pm 0.01$ | $2.23 \pm 0.02$ |
| $3a$ | 0 | 76 | $5.7 \pm 0.1$ | $4.5 \pm 0.1$ | 1.6 | $0.27 \pm 0.01$ | $0.91 \pm 0.03$ |
| 4 | 0 | 76 | $5.9 \pm 0.2$ | $3.0 \pm 0.1$ | 1.6 | $0.56 \pm 0.01$ | $0.69 \pm 0.04$ |
| $5^s$ | 0 | 76 | $7.9 \pm 0.1$ | $3.6 \pm 0.1$ | 2 | $0.74 \pm 0.01$ | $0.72 \pm 0.01$ |
| $6^s$ | 0 | 76 | $7.4 \pm 0.1$ | $4.2 \pm 0.1$ | 2 | $0.50 \pm 0.01$ | $0.83 \pm 0.01$ |
| $7^s$ | 0 | 76 | $7.1 \pm 0.1$ | $6.1 \pm 0.1$ | 2 | $0.18 \pm 0.01$ | $1.40 \pm 0.11$ |
| $3b$ | 0 | 122 | $5.7 \pm 0.1$ | $6.7 \pm 0.1$ | 1.6 | $0.25 \pm 0.01$ | $0.87 \pm 0.09$ |
| $3c$ | 0 | 105 | $5.6 \pm 0.1$ | $5.7 \pm 0.1$ | 1.6 | $0.25 \pm 0.01$ | $0.86 \pm 0.01$ |
| $3d$ | 0 | 90 | $5.6 \pm 0.1$ | $5.2 \pm 0.1$ | 1.6 | $0.25 \pm 0.01$ | $0.94 \pm 0.09$ |
| $3e$ | 0 | 58 | $5.6 \pm 0.1$ | $4.2 \pm 0.1$ | 1.6 | $0.25 \pm 0.01$ | $0.93 \pm 0.05$ |
| PpW1 | 24.0 | 70 | $5.2 \pm 0.1$ | $6.2 \pm 0.1$ | 1.6 | $0.11 \pm 0.01$ | $2.97 \pm 0.09$ |
| 2 | 34.4 | 70 | $5.4 \pm 0.1$ | $6.4 \pm 0.1$ | 1.6 | $0.12 \pm 0.01$ | $2.88 \pm 0.10$ |
| 3 | 40.8 | 70 | $5.3 \pm 0.1$ | $6.2 \pm 0.1$ | 1.6 | $0.11 \pm 0.01$ | $2.67 \pm 0.06$ |
| 4 | 40.7 | 70 | $5.5 \pm 0.1$ | $6.5 \pm 0.1$ | 1.6 | $0.11 \pm 0.01$ | $2.58 \pm 0.03$ |
| $5^p$ | 38.4 | 76 | $7.6 \pm 0.1$ | $8.9 \pm 0.1$ | 1.6 | $0.34 \pm 0.01$ | $2.23 \pm 0.02$ |
| $6^p$ | 43.6 | 76 | $7.2 \pm 0.1$ | $8.1 \pm 0.1$ | 1.6 | $0.30 \pm 0.01$ | $2.05 \pm 0.02$ |
| $7^p$ | 54.7 | 76 | $6.9 \pm 0.1$ | $7.9 \pm 0.1$ | 1.6 | $0.30 \pm 0.01$ | $1.95 \pm 0.01$ |

Table 3.1: Statistical parameters of the present experiments, P are "Paddle generated waves" and PpW "Paddle plus Wind generated waves". $u_{*a}$ is the air friction from Pitot measures, $x$ is the LDV measurement section along the channel (with respect to the first sensor used for reflection analysis, i.e. US3), see Figure 2.1$a$. $H_i$ stands for the incoming wave height, $H_t$ represents the total wave height as defined in equation (2.24), $T$ is the wave period, $K_r$ and $\Delta\varphi = \varphi_i - \varphi_r$ are the reflection coefficient and the phase shift, respectively. Experiments P3$a$–$e$ were done with the same regular wave and reflective conditions but different sections of fluid velocity measurement ($x = 76, 122, 105, 90, 58\,\mathrm{cm}$, respectively). Superscripts $s$ and $p$ stand for a second order generation and a passive absorption, respectively. All the other experiments were conducted with an active absorption system and a first order generation.

US spacings of figure 2.1(*b*). During tests P1, P3*a*–*e* and P4, monochromatic paddle waves were generated with active absorption. Tests P2 differs from the other tests with only-paddle waves generation because it was performed with a passive absorption system, consisting of a dissipative beach with linear profile inclined $\approx 45°$ to the bottom. Tests P5–7 were conducted for regular second order paddle waves, to check the method used here for reflection evaluation one order higher. Tests P3*a*–*e* refer to a wave with the same characteristics (amplitude, period and reflection parameters), but different position of the LDV measurements along $x$.

Then, seven tests with regular waves ruffled by wind (Expts PpW1–7) were carried out. All the PpW experiments were realized in the larger US spacing configuration, see figure 2.1(*a*). Experiments PpW1–4 had the same reflection conditions of experiment P1 (active absorption), while experiments PpW5–7 had the same reflection conditions of P2 (dissipative beach).

The LDV measurements section was co-located with a US sensor for all the P and PpW tests, except for experiment P3*e*). Measurements of each experiment lasted 330 s, a time interval judged sufficient for achieving the consistency of the statistical estimators in our experiments. The quantity $H_t T^{-1}$, where $H_t$ is the total wave height and $T$ is the wave period, is chosen to scale all the velocities (see §2.5.2).

## 3.2 Analysis of the results

### 3.2.1 Wave shape

The first representative image of the wave field is the shape of the wave. Thus, we performed a phase average of the water surface to reproduce the wave shape in each test. Figure 3.1 shows the phase-averaged water surface for P and PpW experiments at the LDV position, and represents the wave shape in each test where the velocity field is measured. The wave profile of the paddle waves (P) has, in general, a limited variability, with a standard deviation of less than a tenth millimeter. In the presence of wind, i.e. for experiments PpW, the variability is more pronounced and standard deviations are of several centimeters (the order of magnitude of the wind waves riding the regular waves). We also notice a larger standard deviation as wind velocity increases, that is what we observe in experiments PpW1 to 4 and PpW5 to 7, respectively. Furthermore, the asymmetry between trough and crest shape increases for increasing $H_i/L$.

### 3.2.2 Wind waves statistics

The separation of the wind-induced component of the signal (wind waves) is performed by applying a high-pass filter of the spectrum in the frequency domain (see §2.3.3). In this way, we can estimate some main statistics of the waves attributed to the wind for experiments PpW1–7. Figure 3.2 shows the fetch-related growth of wave crests, troughs and heights. We notice that for PpW1–4 (active absorption), wind waves grow for increasing fetch and wind intensity. In addition, wave troughs and crests are almost symmetric at lower wind speeds, while wave crests are slightly more pronounced for higher wind speeds at larger fetches. For experiments PpW5–7, wind waves height is constant at different fetches. The explanation can be that wind waves are fully developed, with the balance between the momentum transfer between air and water in equilibrium, or a balance is reached between the net momentum transfer from wind to wave and from wave to water (through wave breaking, for example). The analysis could also be affected by some limits of the triple decomposition technique, that could fail in separating adequately the wind waves from the paddle waves in these experiments.

### 3.2.3 Mean water level

A first assessment of the analytical model is based on the comparison between the theoretical and experimental mean water level. We theoretically obtain the mean water level by means of equation (1.24), while the experimental mean water level (MWL) is evaluated by averaging the US signals as described in §2.3.3. Figure 3.3 shows the results for P2–6 and for PpW5–7 experiments. We highlight that, for a finite-length flume, the experimental mean water level (MWL) is very hard to be evaluated with accuracy, as a

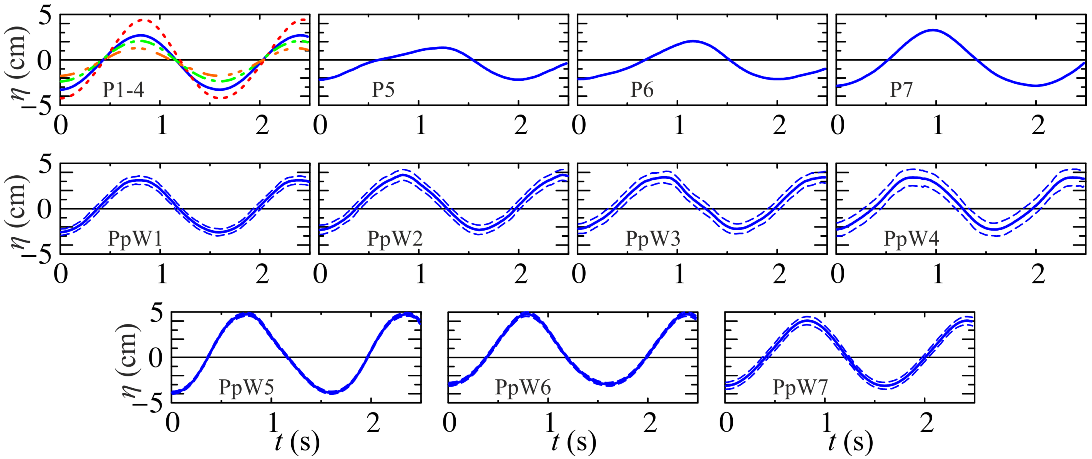

Figure 3.1: The wave profile of the experiments at the LDV position, obtained from the phase average of the free surface data. Solid lines are phase-averaged values, while the dashed curves indicate one standard deviation.

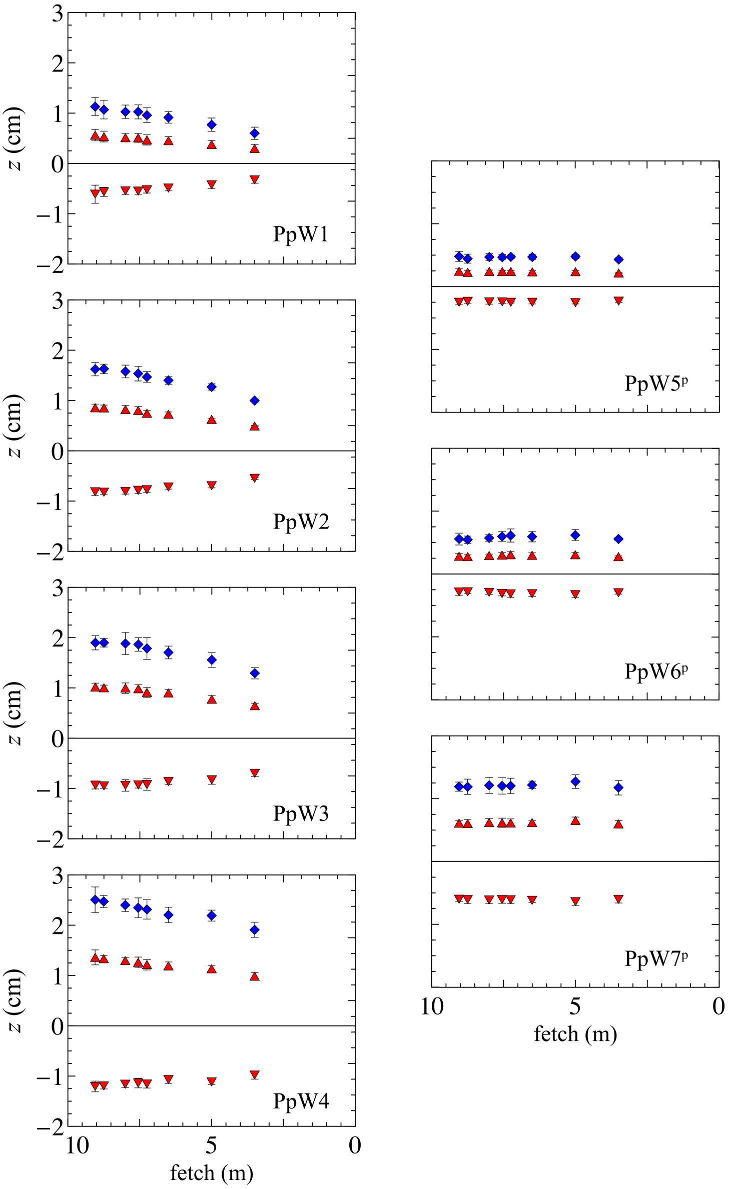

Figure 3.2: Wave height (blue diamonds) for wind waves, estimated from the triple decomposition of the free surface. Up-pointing and down-pointing red triangles represent crests and troughs, respectively. Fetch origin is at the inflow section of the wind (the end of the baffle in Figure 2.1*a*)

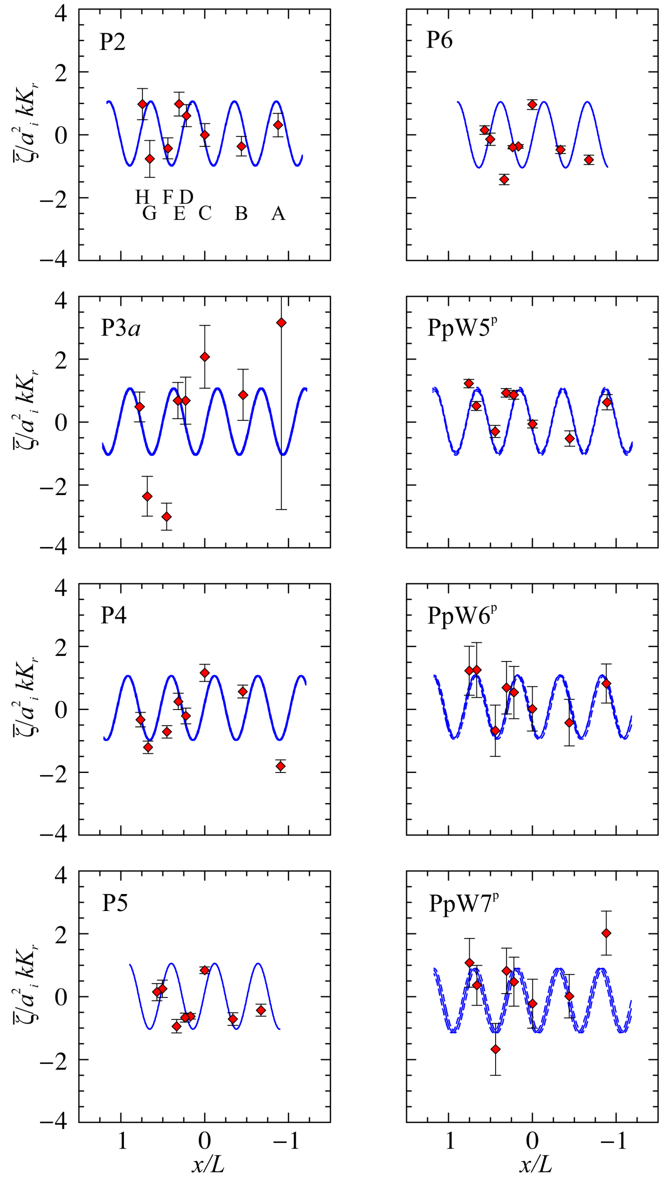

Figure 3.3: Theoretical mean water level calculated from equation (1.24) (solid line), and experimental values (symbols). Letters A-H in the upper left panel represent the location of the ultrasound probes. Error bars are two standard deviations.

consequence of several factors. Above all: (i) the analytical model considers an indefinite fluid domain along $x$, while in reality the boundary conditions due to the finite length of the channel, which is less than 5 experimental wave lengths, have a strong influence on the MWL values; (ii) water may accumulate locally in between or behind the part delimited by the two paddles, since there is no feedback system to fully respect mass conservation in the fluid domain where the probes are located. Even considering these two limits of the experimental conditions, the comparison is again fairly good, with a peak–to–peak value well predicted by the theory and with a satisfactory overlap between theory and experiments.

One recommendation could be finer spatial resolution (or moving gauge) to reduce aliasing, that is exactly what has been done for experiments with opposing winds (analyzed in chapter 4).

### 3.2.4 Mean velocity

Time averaging the LDV signal yields the mean component of the horizontal and vertical velocities $\overline{u}$ and $\overline{w}$, respectively.

Figure 3.4 shows the results of the mean velocities for P experiments (paddle waves). The horizontal mean velocity $\overline{u}$, which represents the mean current in the wave flume, is negative and $\approx 0.5 \cdot H_t T^{-1}$ for most experiments. The measured values of the mean vertical velocity $\overline{w}$ are in general negative (except for P1), even though the trend is not well defined in the vertical. We notice that the trend of experiment P2 differs significantly from the others; since it was the one realized with passive absorption among the P experiments, we attribute to the experimental absorption condition that particular behaviour.

In the presence of following wind (figure 3.5), the horizontal velocity is positive, i.e. cocurrent with the wind, near the free surface, while becomes negative at lower levels. The trend of the measured vertical velocities can be resumed in this way: $\overline{w}$ is negative near the surface and becomes positive toward the bottom. The behaviour of both horizontal and vertical velocities is somewhat expected, since the wind acts on the surface with a shear stress which causes positive horizontal velocity, and a pressure normal to

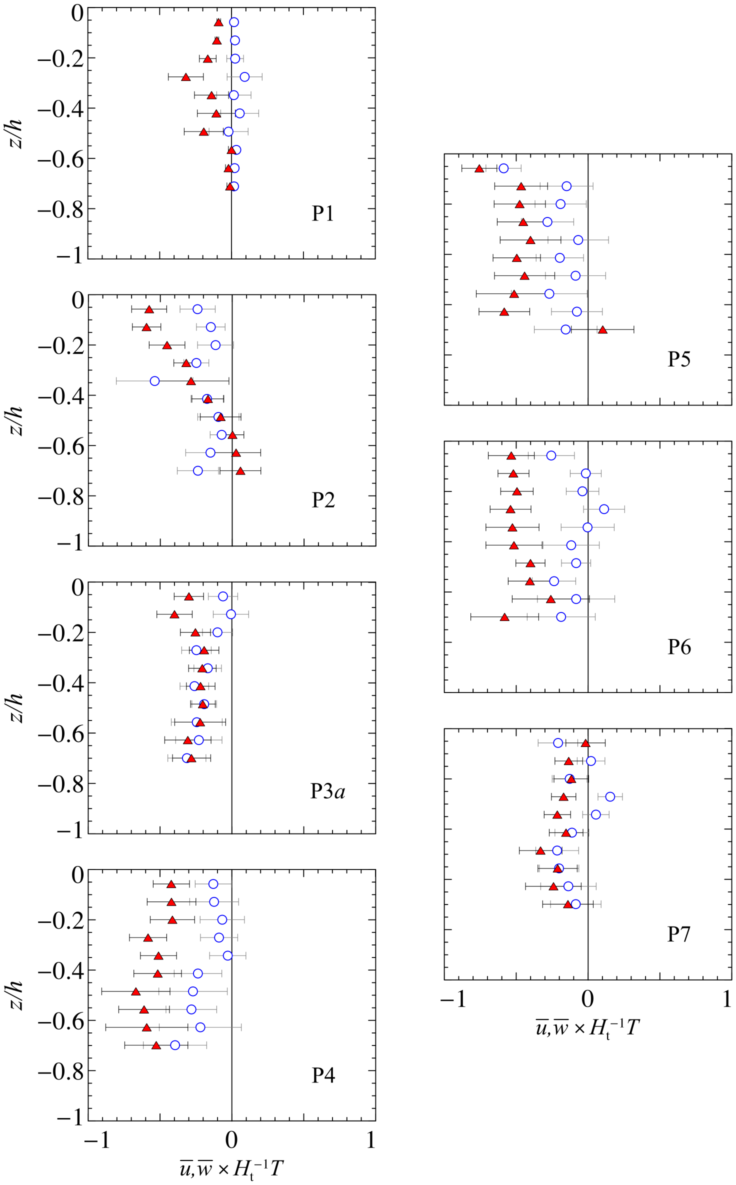

Figure 3.4: Experiments P1–7, paddle waves. Mean horizontal $\overline{u}$ (red filled triangles) and vertical $\overline{w}$ (empty circles) velocities, non dimensional with respect to the velocity scale $H_tT^{-1}$, where $H_t$ is the total local wave height and $T$ the wave period. Error bars are one standard deviation.

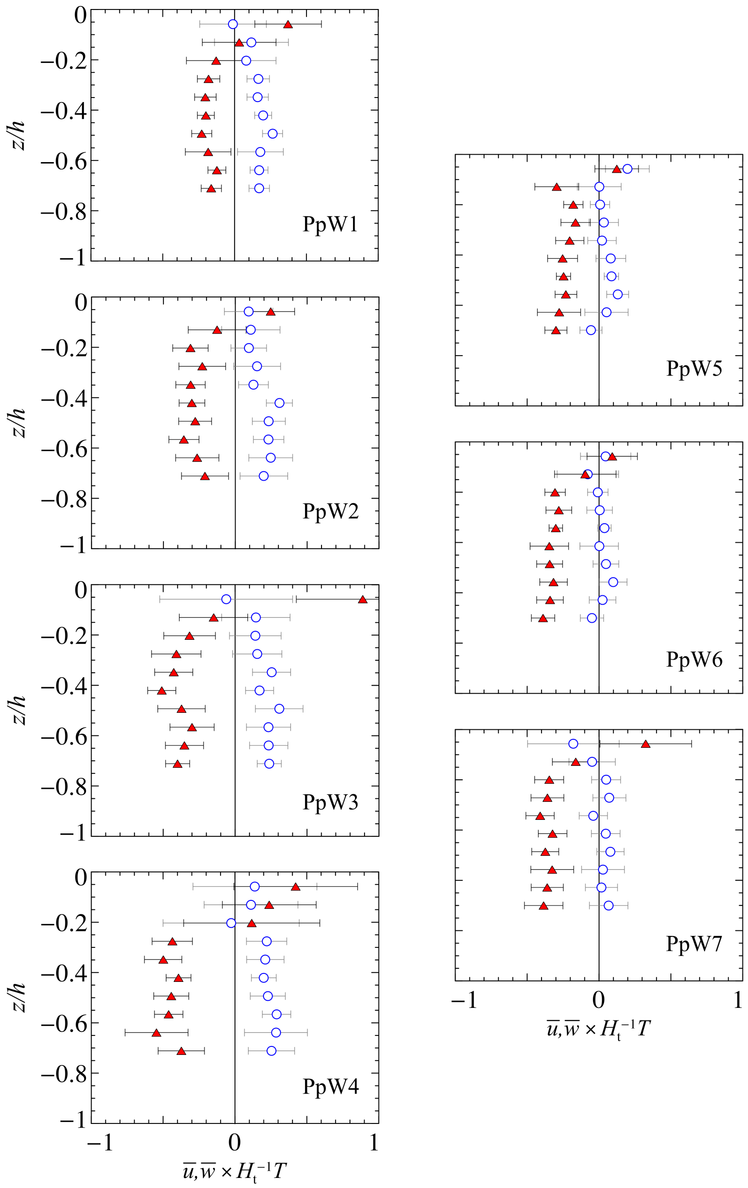

Figure 3.5: Experiments PpW1–7, paddle waves with following wind. Mean horizontal $\overline{u}$ (red filled triangles) and vertical $\overline{w}$ (empty circles) velocity, non dimensional with respect to $H_t T^{-1}$, where $H_t$ is the total local wave height and $T$ the wave period. Error bars are one standard deviation.

the free surface. Pressure gradients are related usually to forces, and at the interface forces can act on the fluid also in the vertical direction causing acceleration which in time means a non-null vertical velocity. In particular, if the normal pressure is directed in average toward the bottom (negative $z$), near the surface the fluid is accelerated producing negative vertical velocities. At lower levels, for mass conservation the signs have to be inverted. Furthermore, other factors can influence both the horizontal and vertical mean velocity, as the presence of cells inside the flume or secondary circulation in the transverse direction, perpendicular to $x$ and $z$, which can develop for the finite length of the channel. The wind waves which develop are superimposed to the paddle waves and have a wave length of less than $\approx 10\,\mathrm{cm}$. Thus, they influence the orbital motion for $\approx 5\,\mathrm{cm}$, less than 10% of the still water depth.

### 3.2.5 Variability of the Reynolds wave shear stress

The presence of reflection causes additional effects in the water field. Among the others, the correlation between the horizontal and vertical velocities induces the Reynolds wave shear stress $-\overline{\widetilde{u}\widetilde{w}}$, with theoretical values calculated from equation (1.13) in Chapter §1 and experimental values obtained from the data analysis described in §2.2.3.

Figures 3.6–3.7 show the comparison between the theoretical and experimental $-\overline{\widetilde{u}\widetilde{w}}$ in the vertical for P and PpW waves, respectively. For the great majority of the experimental points, we observe the overlap between the 95% confidence limits of the theoretical relation and the error bars. Results from P experiments show that covariance can be either positive or negative, quite large or small, depending on the phase lag between the incident and the reflected wave components and on the reflection coefficient. PpW experiments show only a negative profile of the covariance, but we expect that by changing the measurement section along the channel we would have obtained different intensity and eventually even sign of $-\overline{\widetilde{u}\widetilde{w}}$. Our expectations derive from theoretical prediction of the vertical profile of the Reynolds wave shear stress according to equation (1.13), which indicates that the $-\overline{\widetilde{u}\widetilde{w}}$ can assume positive or negative values depending on the reflective conditions (the parameters $K_r$ and $\Delta\varphi$) and the velocity measurements section along the channel (coordinate $x$ of Table 3.1). The physical meaning of a different sign in the Reynolds wave shear stress is a change in the direction of the momentum transfer, that is from the wave to the wind when $-\overline{\tilde{u}\tilde{w}} < 0$. The fact that some tests show a negative profile, while others (like P5 and P6) exhibit positive vertical profiles, is coherent with theoretical predictions. As a consequence, when reflection is present even with low intensity, a single section is not representative of the entire wave field (as illustrated also in Olfateh *et al.*, 2017). We still remind that the theory does not involve wind action, thus we are not surprised that some points near the interface in experiments PpW (PpW4, PpW5 and PpW6 in figure 3.7) are not well aligned with the theoretical predictions.

At this point, that would be useful to link back to the literature review, in order to check if there is consistency or not with the present study. Figure 3.8 shows the comparison between the Reynolds wave shear stress of the present thesis and some previous experimental works involving monochromatic and wind waves. We can see that the order of magnitude of the scaled stresses are similar and, as expected, the sign can vary as a consequence of the spatial variability of the velocity covariance $\overline{\tilde{u}\tilde{w}}$.

Since the velocity covariance is modulated along $x$, our theoretical model required further checks by repeating the LDV velocity measurements at different sections along the flume (tests P3$a$–$e$). We chose to keep the same nominal reflective conditions of test P3$a$ to assess if only the spatial variation was responsible for change in the vertical profile of $-\overline{\tilde{u}\tilde{w}}$. Figure 3.9 reports the results of experiments P3$a$–$e$ at different $z$ levels. It shows that the covariance $-\overline{\tilde{u}\tilde{w}}$ has a clear spatial variability along $x$ (see Olfateh *et al.*, 2017).

### 3.2.6 Reynolds wave and turbulent stresses

The normal components $\overline{\tilde{u}\tilde{u}}$ and $\overline{\tilde{w}\tilde{w}}$ of the Reynolds wave covariance tensor can be theoretically derived and measured from data analysis. Figures 3.10 and 3.11 report the results of the Reynolds wave normal stresses in the vertical (note the semi-log scale) for P and PpW experiments, respectively,

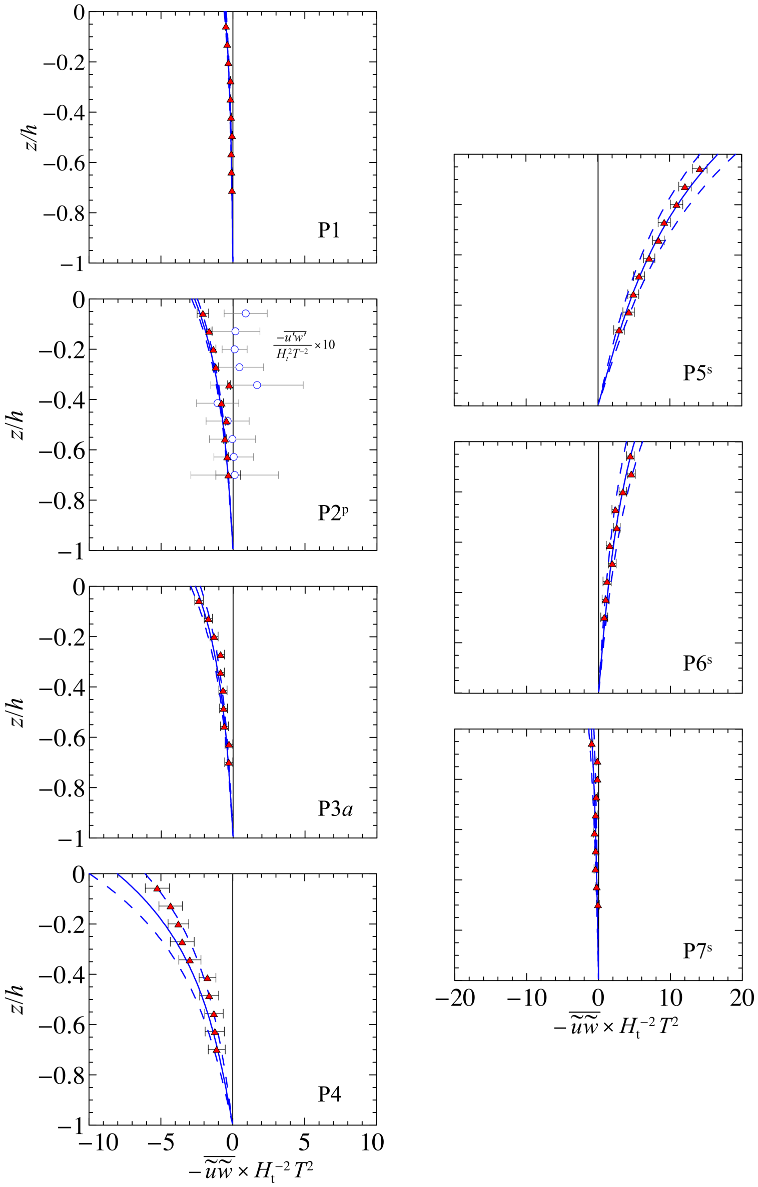

Figure 3.6: Experiments P1–7, paddle waves. Measured (triangles) and theoretical (solid lines) shear stress $-\overline{\widetilde{u}\widetilde{w}}$ compared in the vertical, non dimensional with $H_t^2T^{-2}$. For test P2 also the turbulent shear stress (circles) is shown, note the different scale. Error bars are one standard deviation, dashed lines 95% confidence limits.

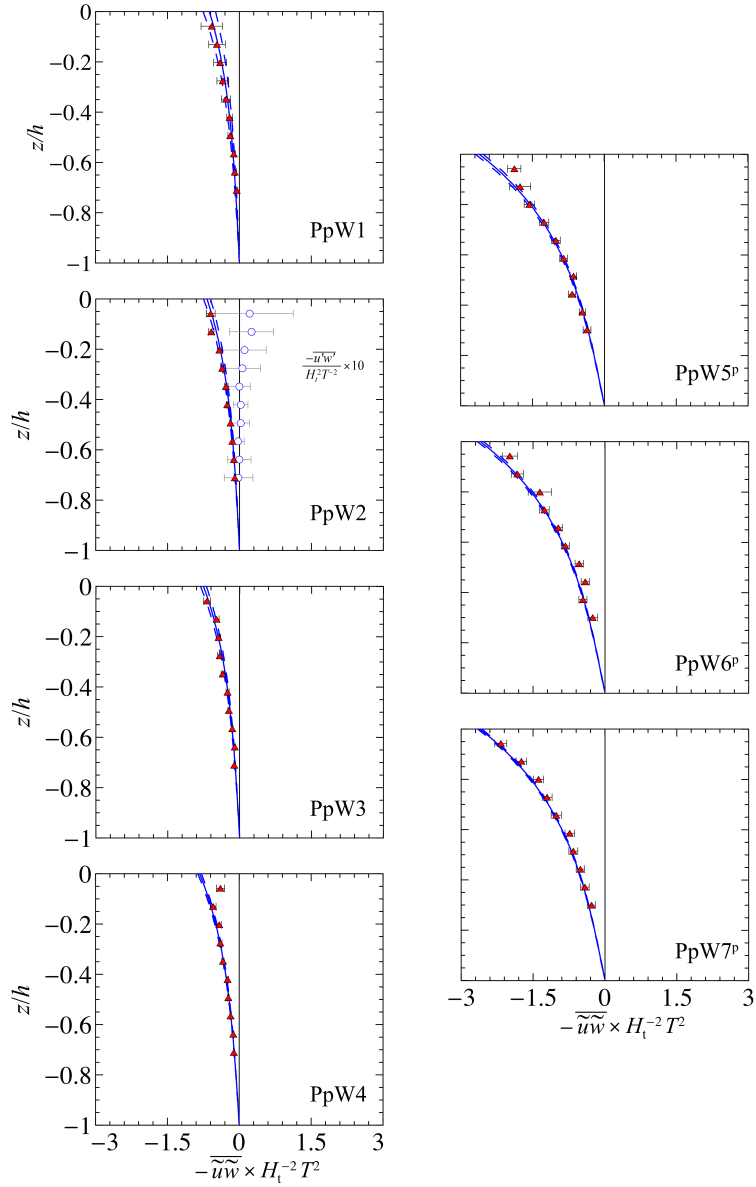

Figure 3.7: Experiments PpW1–7, paddle waves plus following wind. Comparison between theoretical (solid lines) and measured (triangles) $-\overline{\tilde{u}\tilde{w}}$, non dimensional with $H_t^2T^{-2}$. For experiment PpW2 also the turbulent shear stress (circles) is shown, note the different scale. Error bars are one standard deviation, dashed lines 95% confidence limits.

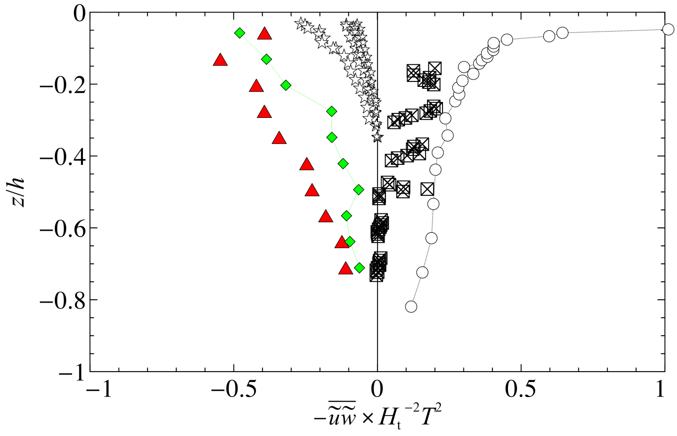

Figure 3.8: Comparison of the vertical profile of the experimental non-dimensional Reynolds wave shear stress $-\overline{\tilde{u}\tilde{w}}$ with previous works. ○ Longo & Losada (2012), only wind waves; ⊠ Olfateh *et al.* (2017), paddle waves plus following wind; ☆ Cheung & Street (1988), paddle waves plus following wind; ◆ present experiment P1, paddle waves without wind; ▲ present experiment PpW4, paddle waves plus following wind.

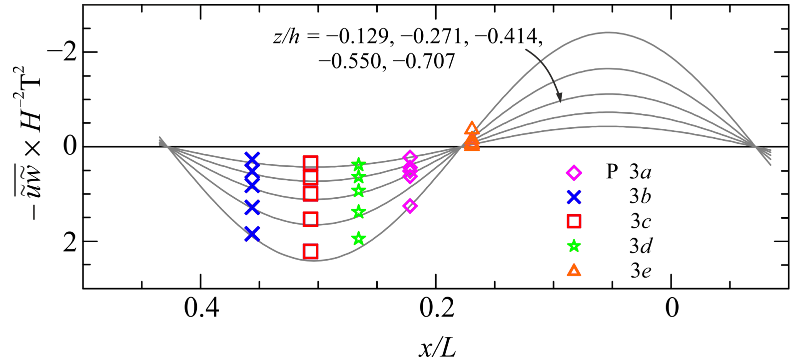

Figure 3.9: Experiments P3$a$–$e$, paddle waves (same reflection, different LDV position). Spatial variation of the velocity covariance $-\overline{\tilde{u}\tilde{w}}$ along $x$, at different $z$. Symbols are experimental points, while solid lines are the theoretical values. Only one level in two is shown for a better visualization.

while figure 3.12 shows the results for P3a–e experiments (same reflective conditions, different LDV measurement section). The experimental values show good agreement with the analytical trend within the experimental uncertainties; however, when approaching the free surface, the normal stresses tend to be overestimated by the theory, in particular for the horizontal components of the PpW experiments. This can be attributed to the presence of wind, which enhances turbulence at the interface between air and water. As a consequence, in the surface boundary layer the measured Reynolds wave stresses do not strictly respect the theoretical model, since the analytical formulation developed in this thesis takes into account only the wave

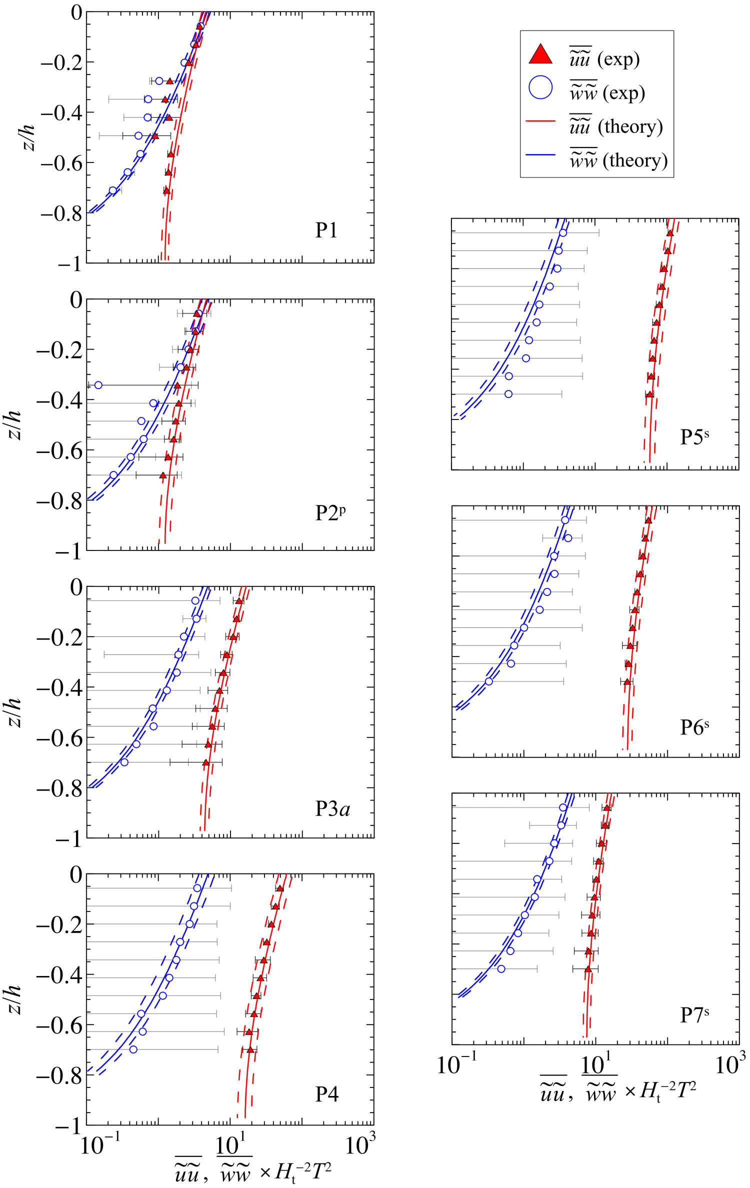

Figure 3.10: Experiments P1–7, paddle waves. Comparison between measured (symbols) and theoretical (solid lines) Reynolds wave normal stresses (note the semi-log scale). Red and blue colors stand for $\overline{\tilde{u}\tilde{u}}$ and $\overline{\tilde{w}\tilde{w}}$, respectively. Error bars are two standard deviations, dashed lines 95% confidence limits.. All the values are non dimensional with respect to $H_t^2 T^{-2}$.

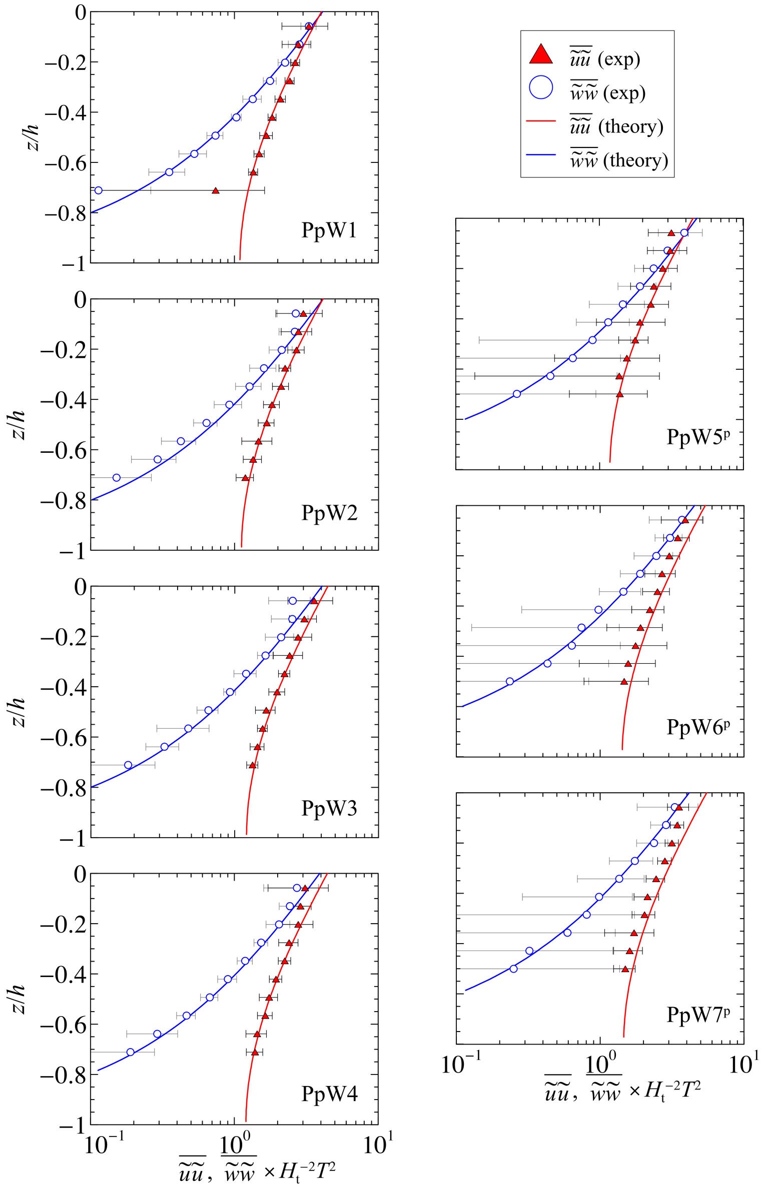

Figure 3.11: Experiments PpW1–7, paddle waves plus following winds. Comparison between measured (symbols) and theoretical (solid lines) Reynolds wave normal stresses (note the semi-log scale). Red and blue colors stand for $\overline{\widetilde{u}\widetilde{u}}$ and $\overline{\widetilde{w}\widetilde{w}}$, respectively. Error bars are two standard deviations. All the values are non dimensional with respect to $H_t^2T^{-2}$.

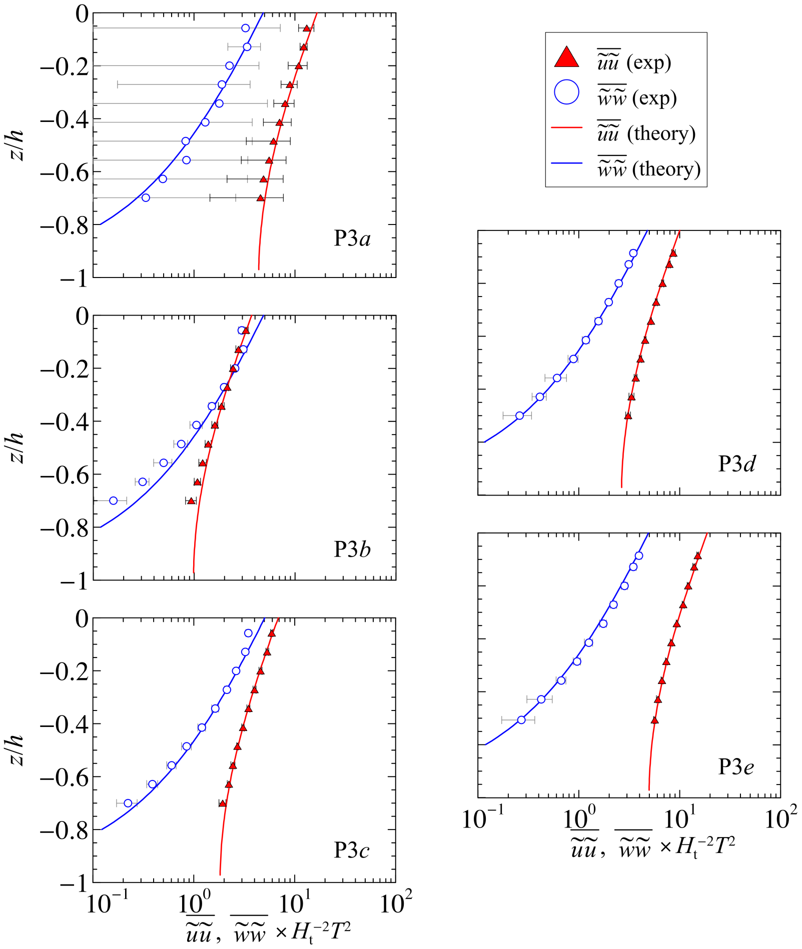

Figure 3.12: Experiments P3$a$–$e$, paddle waves. Comparison between measured (symbols) and theoretical (solid lines) Reynolds wave normal stresses, note the semi-log scale. Red and blue colors stand for $\overline{\widetilde{u}\widetilde{u}}$ and $\overline{\widetilde{w}\widetilde{w}}$, respectively. Error bars are two standard deviations. A confidence interval at 95% of the theoretical values was calculated, but not shown for a better visualization of the results. All the values are non dimensional with respect to $H_t^2T^{-2}$.

potential terms and does not consider any further contribution.

The measured Reynolds turbulent stresses are calculated from the velocity covariance analysis of the turbulent components (see 2.2.3). Figures 3.13 and 3.14 show the normal components $\overline{\widetilde{u'u'}}$ and $\overline{\widetilde{w'w'}}$ of the Reynolds wave stress tensor for P and PpW experiments, respectively. For only-paddle waves, turbulence is almost isotropic with $\overline{\widetilde{u'u'}}$ as the dominant term (exception for test P7$^{\mathrm{s}}$), and the non-dimensional stresses increase for increasing reflection coefficient. For paddle-waves with following wind, the interpretation is different for experiments with active absorption (PpW1–4) and for experiments with passive absorption (PpW5–7). For experiments PpW1–4, both the normal stresses $\overline{\widetilde{u'u'}}$ and $\overline{\widetilde{w'w'}}$ are significantly higher near the surface, while decreasing at lower water levels, as expected since the forcing (wind) acts at the water surface. For experiments PpW5–7, $\overline{\widetilde{u'u'}}$ and $\overline{\widetilde{w'w'}}$ are almost uniform in the vertical. We do not have a definite explanation: it can have a physical meaning (turbulence propagates in all the fluid domain) or can be attributed to a contamination of the fluctuating component during the triple decomposition.

Figures 3.15 and 3.16 report the Reynolds turbulent shear stress $\overline{\widetilde{u'w'}}$. For only-paddle waves (Figure 3.15), the shear stress components are null in average along the vertical, that is what we should expect in the absence of wind. In this case, the variability of the experimental data increases for increasing reflection coefficient. For paddle-waves in the presence of following wind (Figure 3.16), we distinguish again between PpW1–4 and PpW5–7 experiments: these last ones do not show a clear trend of the turbulent shear stress $\overline{\widetilde{u'w'}}$, which varies around the zero. From the experimental results, it is clear that passive and active absorptions induce different flow field in the measurements, at least in our experiments. We think that passive absorption can affect more the flow field, since it subtracts energy to the wave non-uniformly along $x$, inducing further effects as water mass accumulation (and release) or residual currents which are not taken into account in the present analysis. On the other hand, the active absorption system is uniform in space (a piston which compensates the incoming wave), thus we

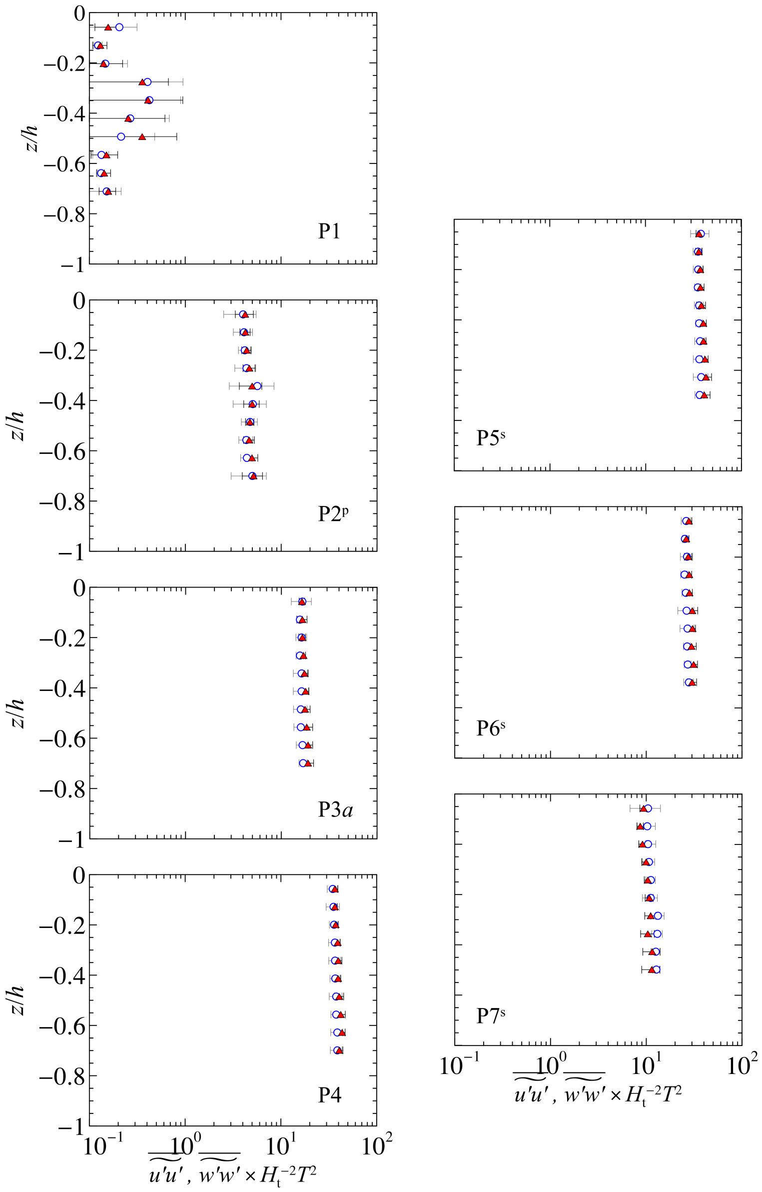

Figure 3.13: Experiments P1–7, paddle waves. Measured Reynolds turbulent normal stresses: red filled triangles are $\overline{\widetilde{u'u'}}$ and blue empty circles are $\overline{\widetilde{w'w'}}$, respectively. Error bars are two standard deviations. All the values are non dimensional with $H_t^2T^{-2}$.

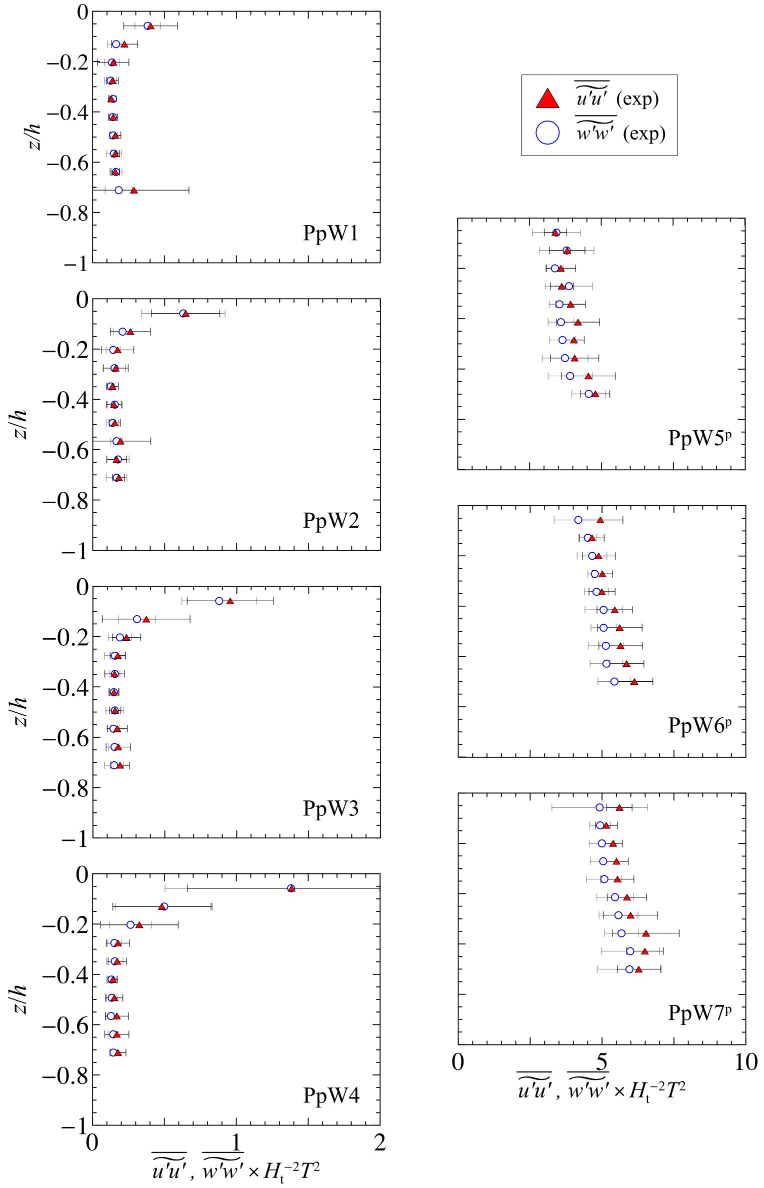

Figure 3.14: Experiments PpW1–7, paddle waves plus following wind. Measured Reynolds turbulent normal stresses: red filled triangles are $\widetilde{\overline{u'u'}}$ and blue empty circles $\widetilde{\overline{w'w'}}$, respectively. Error bars are two standard deviations. All the values are non dimensional with $H_t^2 T^{-2}$.

think that its effects on the wave field should be less visible.

We notice that the term $\overline{\widetilde{u'w'}}$ is at least one order of magnitude smaller than the Reynolds wave shear stress $\overline{\tilde{u}\tilde{w}}$. These results should be correct and expected far from the surface boundary layer, where turbulence induced by fluctuations at the interface can be dominant even in the absence of breaking (see Longo, 2010, 2011).

On the other hand, tests PpW1–4 show that $\overline{\widetilde{u'w'}}$ is negative at the surface and tends to zero at lower water levels, which is what we should expect. More precisely, we should expect that the negative shear stress at the surface is due to a positive $u'$ and a negative $w'$, which means that the momentum transfer on average is from air to the water. A quadrant analysis is mandatory to clarify the turbulence structure and to obtain this information.

### 3.2.7 Quadrant Analysis

A quadrant analysis is performed for paddle waves plus following wind (PpW) in order to extrapolate further information about the structure of the momentum exchange due to turbulence. The technique is described in 2.2.3 and allows the categorisation of the Reynolds turbulent shear stress contributions on the basis of the fluctuating velocities $u'$ and $w'$. The combined signs of the fluctuating components determines four quadrants representing each one a different type of motion, see figure 2.3. Events which take place in the first and third quadrants are defined as sweeps and ejections, respectively, while events which belong to second and fourth quadrants are referred to as inward and outward interactions.

Figure 3.17 shows the vertical profiles of the quadrant-contributions shear stress for tests with paddle plus wind generated waves (Expts PpW1–7). The major contributions to the turbulent field derive from the event-averaged shear stresses $S_2$ and $S_4$, which represent outward and inward interactions, respectively. This result is different from what usually happens at near-wall or air turbulent boundary layers, where the main turbulence production is generally due to ejection and sweeps (first and third quadrant, respectively), but it is in agreement with previous studies in the

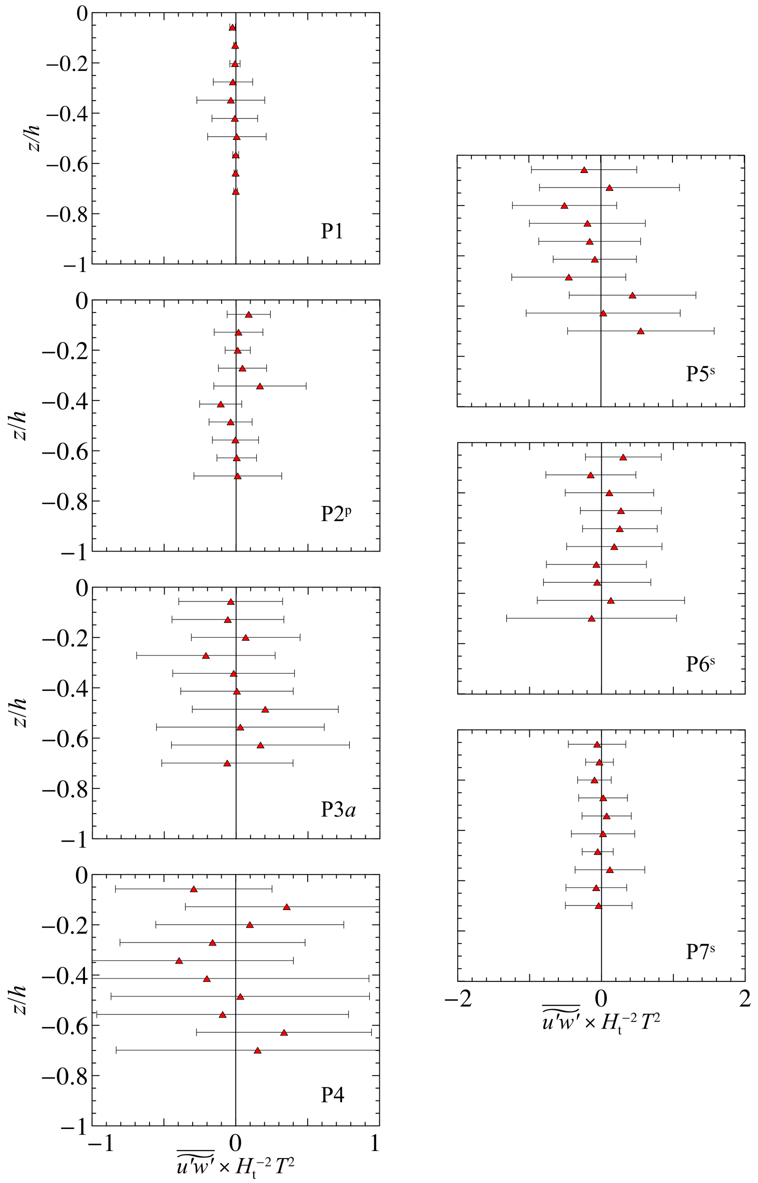

Figure 3.15: Experiments P1–7, paddle waves. Symbols (red filled triangles) are the measured Reynolds turbulent shear stress. Error bars are two standard deviations. All the values are non dimensional with $H_t^2 T^{-1}$.

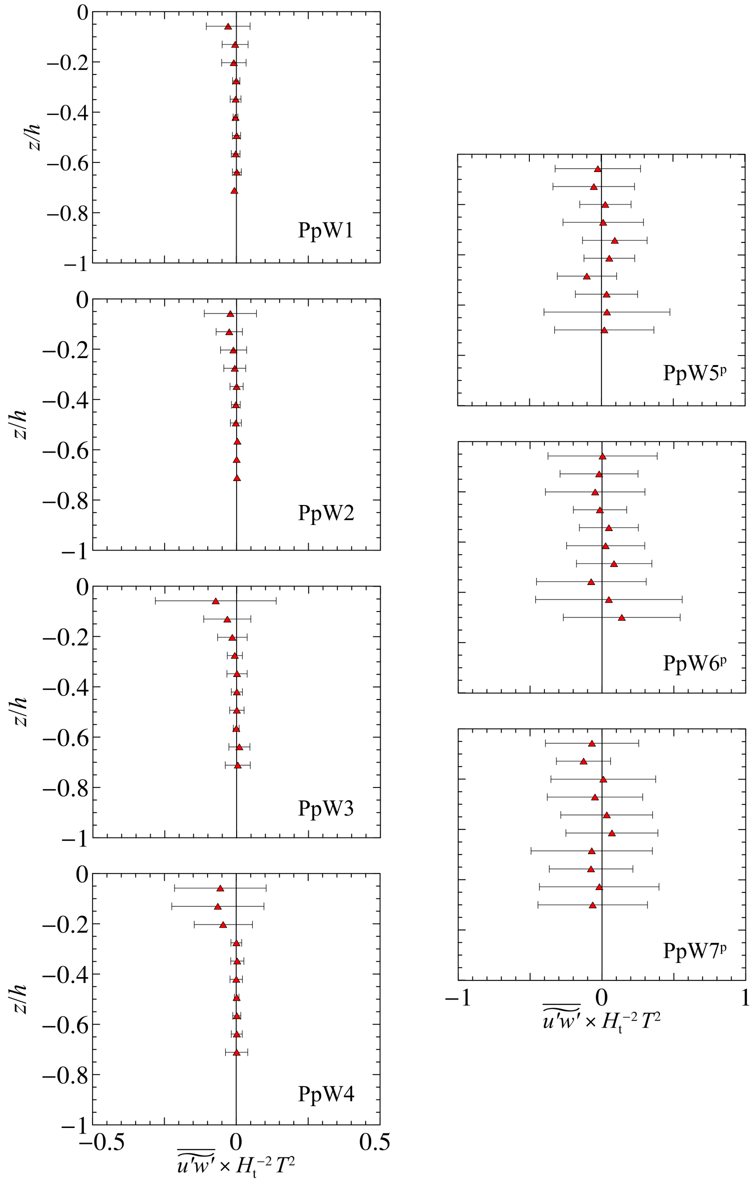

Figure 3.16: Experiments PpW1–7, paddle waves plus following wind. Symbols (red filled triangles) are the measured Reynolds turbulent shear stress. Error bars are two standard deviations. All the values are non dimensional with $H_t^2 T^{-2}$.

water boundary layer for air-sea interaction observations (see, e.g., Longo & Losada, 2012; Longo *et al.*, 2012). We notice again the different behaviour between experiments with an active absorption system (PpW1–4) and experiments with passive absorption (PpW5–7): in the first case, the turbulent shear stress of each quadrant is more effective toward the surface and goes to zero at lower levels; in the second case, the vertical profile is almost uniform, with a slight increase from the top to the bottom.

The time-averaged Reynolds shear stress from each quadrant are also calculated as function of the parameter $M$, which determines the threshold above which events are considered. Figure 3.18 shows the results for experiment PpW4, with different levels of concentration $C_M^j$ superimposed to the time-averaged shear stress, decomposed in quadrants and without decomposition (total). We notice that the main contribution to the total shear stress derives from the quadrants $\mathrm{Q}_2$ and $\mathrm{Q}_4$, with a major momentum transfer from the air to the water side.

### 3.2.8 Reynolds stress tensor principal axes

The Reynolds stress tensors are further investigated by analysing the principal components of each tensor. The analysis is conducted separately for both the wave and the turbulent stress components.

Through the diagonalization of the Reynolds wave stress tensor, we can obtain the theoretical principal stresses $\widetilde{\sigma}_{\mathrm{max}}$ an $\widetilde{\sigma}_{\mathrm{min}}$. Their analytical form is computed from equation (1.27), with parameters from Table 3.1, while the experimental values are evaluated from the relation of equation (1.26), obtained from data analysis.

The ratio of the maximum to the minimum principal stress gives insights about the isotropy of both the diagonalized wave and turbulent stress tensors. We can compare the theoretical and experimental value of the ratio $\widetilde{\sigma}_{\mathrm{max}}/\widetilde{\sigma}_{\mathrm{min}}$ at each point along the vertical, where $\widetilde{\sigma}_{\mathrm{max}}$ and $\widetilde{\sigma}_{\mathrm{min}}$ are the maximum and minimum stress, respectively. We can also calculate the experimental principal stresses of the Reynolds turbulent stress tensor, $\sigma'_{\mathrm{max}}$ and $\sigma'_{\mathrm{min}}$. which is equivalent to the Reynolds wave stress tensor but involves turbulent velocities. We can use the relation (1.31) to evaluate the

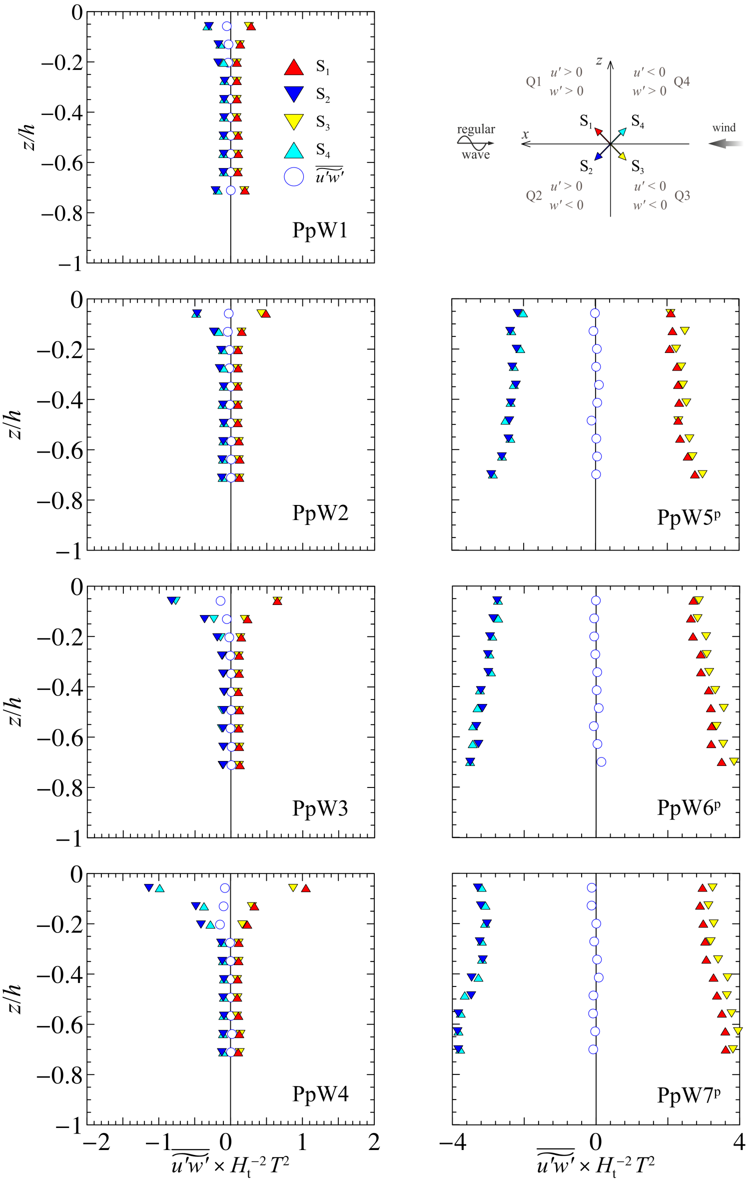

Figure 3.17: Experiments PpW1–7. The event-averaged shear stress $S_j$ for the $j$th quadrant (triangles) and the total shear stress (circles).

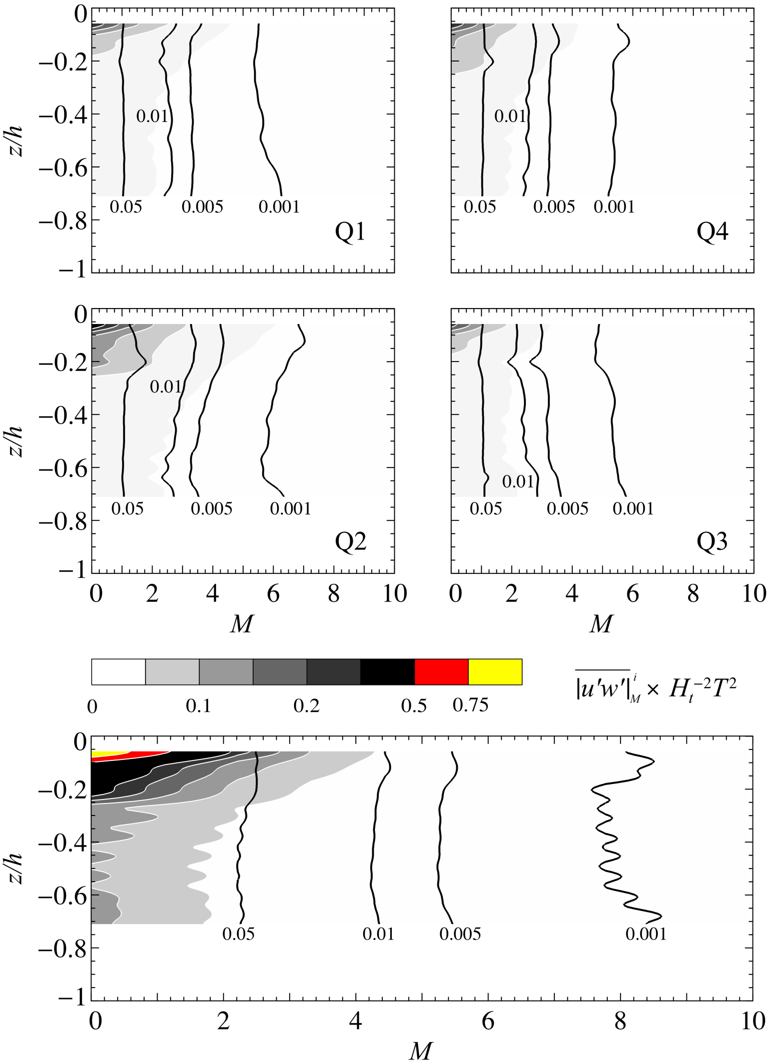

Figure 3.18: Experiment PpW4. Time-averaged Reynolds shear stress in each quadrant decomposed (upper panels) and without decomposition (lower panel), as a function of the threshold parameter M. The isolines of the duration fraction (concentration) are superimposed.

experimental values of $\sigma'_{\max}$, $\sigma'_{\min}$ and their ratio $\sigma'_{\max}/\sigma'_{\min}$.

Figures 3.19 and 3.20 show the results of the ratio $\sigma_{\max}/\sigma_{\min}$ along the vertical, for paddle waves (P) and paddle waves plus following wind (PpW), respectively. All figures report both the wave and turbulent Reynolds principal stresses. The experimental and theoretical values of the Reynolds wave principal stresses ratio $\widetilde{\sigma}_{\max}/\widetilde{\sigma}_{\min}$ show good agreement in all the experiments and report and increasing anisotropy of the diagonalized wave stress tensor for increasing reflection. The turbulent principal stresses ratio $\sigma'_{\max}/\sigma'_{\min}$ is almost uniform in the vertical and slightly larger than 1, and for paddle waves plus following wind with active absorption (figure 3.20, experiments PpW1–4) it tends to increase from bottom to the surface.

Figure 3.21 reports the ratio $\sigma_{\max}/\sigma_{\min}$ along the vertical for experiments 3*a*–*e*, which represent the same reflective conditions for different LDV measurement sections. We notice again the goodness of the theoretical fitness, and the dependence of the periodic and also turbulent principal stresses ratio on the LDV measurements section.

The angle between the reference system $x$-$z$ and the axes of the principal stresses (also called principal angle, for simplicity) is defined for both wave and turbulent principal stresses in §1.3. The theoretical wave principal angle $\widetilde{\alpha}_{p,\mathrm{th}}$ is represented by equation (1.29), while the experimental values $\widetilde{\alpha}_{p,\mathrm{exp}}$ (for wave) and $\alpha'_{p,\mathrm{exp}}$ (for turbulence) are calculated from the relations (1.28) and (1.32), respectively.

Figures 3.22 and 3.23 show the vertical profile of principal angle $\alpha_p$ along the vertical for paddle waves (P) and paddle waves plus following wind (PpW), respectively. The vertical profile show the modulation induced by the different partially-reflective conditions, and also the different shape of the theoretical curves.

Figure 3.24 refers to experiments P3*a*–*e*, i.e. paddle waves in the absence of wind with same reflective conditions but different sections of LDV measurement. All figures show good agreement between theory and experiments and report again that also the varying sections of measurements yield a modulation of the principal angles of the wave stress tensor, as observed for the other quantities of interest in the previous sections.

The fluctuating principal angle $\alpha'_{exp}$ is quite disperse in the vertical;

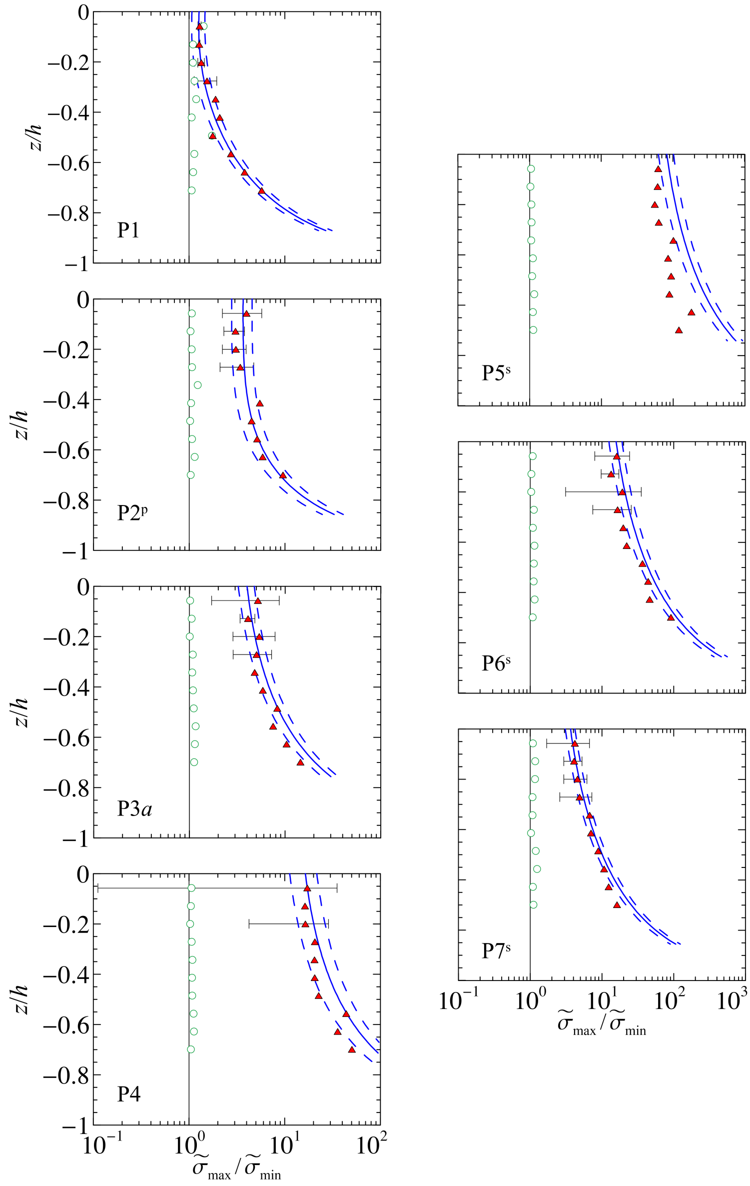

Figure 3.19: Experiments P1–7, paddle waves. Ratio of the maximum to the minimum principal stress $\sigma_{\max}/\sigma_{\min}$. Triangles and circles are periodic and fluctuating measurements, respectively, with error bars equal to two standard deviations. Solid lines are theoretical values from equation (1.27), while dashed lines are confidence intervals to 95%.

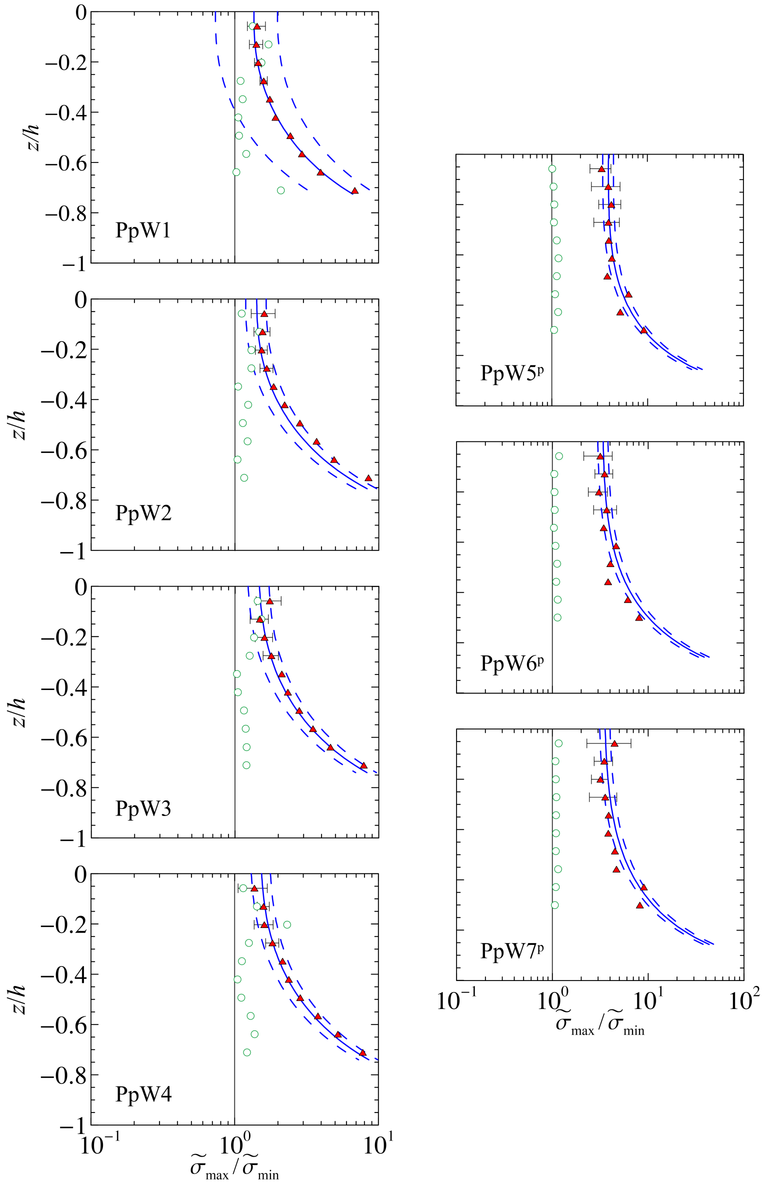

Figure 3.20: Experiments PpW1–7, paddle waves with following wind. Ratio of the maximum to the minimum principal stress $\sigma_{\max}/\sigma_{\min}$. Triangles and circles are periodic and fluctuating measurements, respectively, with error bars equal to two standard deviations. Solid lines are theoretical values, dashed lines are confidence intervals to 95%.

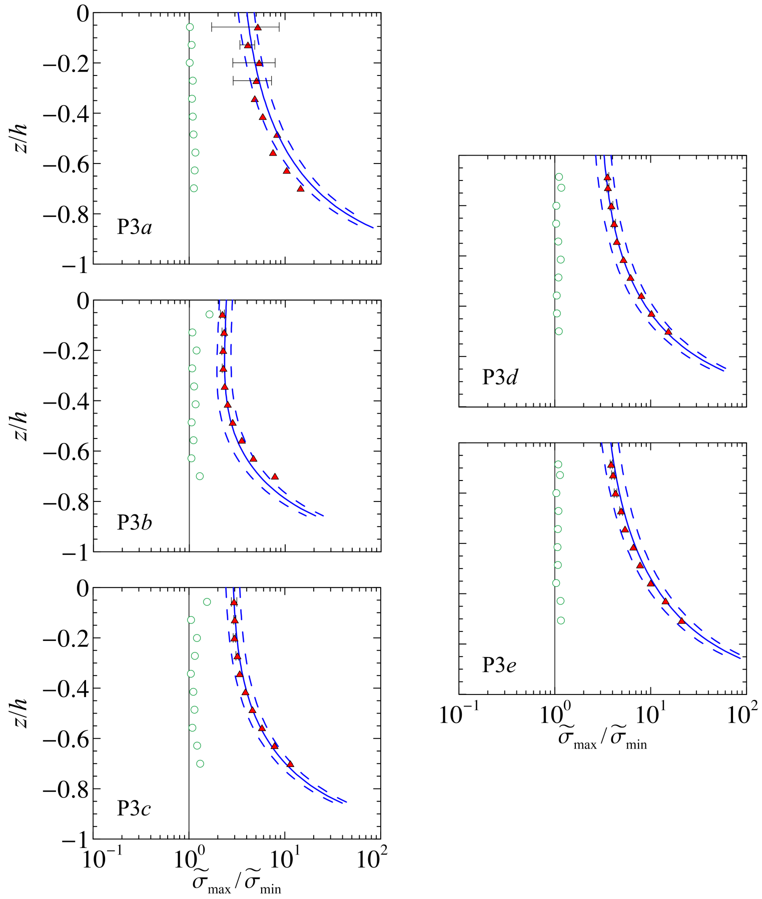

Figure 3.21: Experiments P3$a$–$b$, paddle waves (same reflection, different LDV position). Ratio of the maximum to the minimum principal stress $\sigma_{max}/\sigma_{min}$. Triangles and circles are periodic and fluctuating measurements, respectively, with error bars equal to two standard deviations. Solid lines are theoretical values, dashed lines are confidence intervals to 95%.

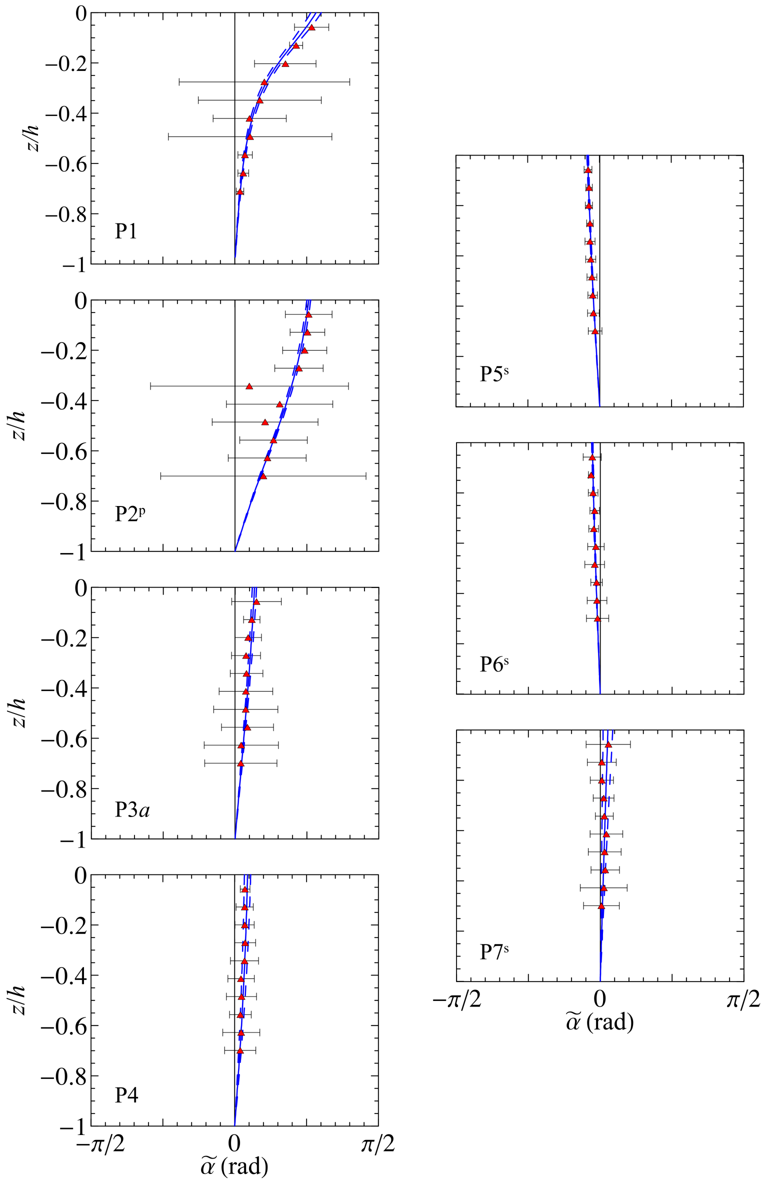

Figure 3.22: Experiments P1–7, paddle waves. Principal angles $\widetilde{\alpha}_p$ for Reynolds wave stress tensor. Red triangles are experimental values, with error bars equal to two standard deviations. Solid lines are theoretical values from equation (1.29), while dashed lines are confidence intervals to 95% level.

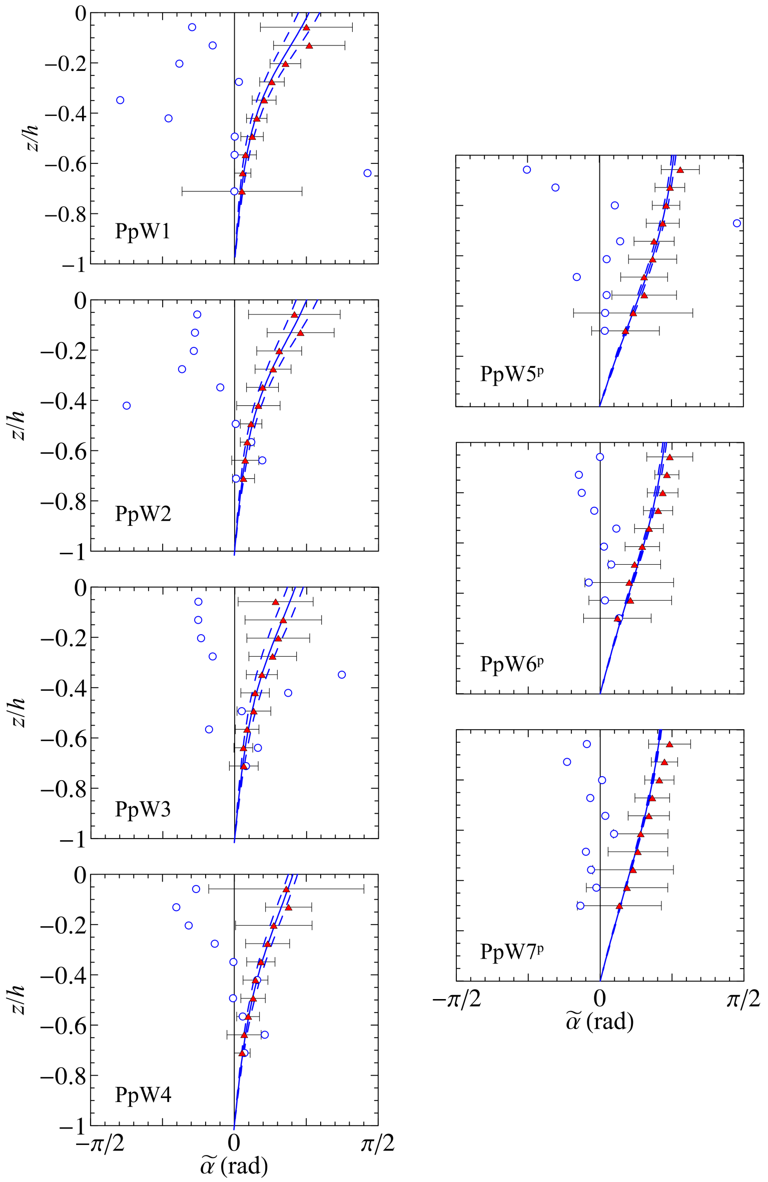

Figure 3.23: Experiments PpW1–7, paddle waves with following wind. Wave and turbulent principal angles $\widetilde{\alpha}_p$ and $\alpha'_{exp}$, respectively. Triangles and circles are periodic and fluctuating experiments, respectively, while solid lines are theoretical values. Error bars are two standard deviations, dashed lines are confidence intervals to 95% level.

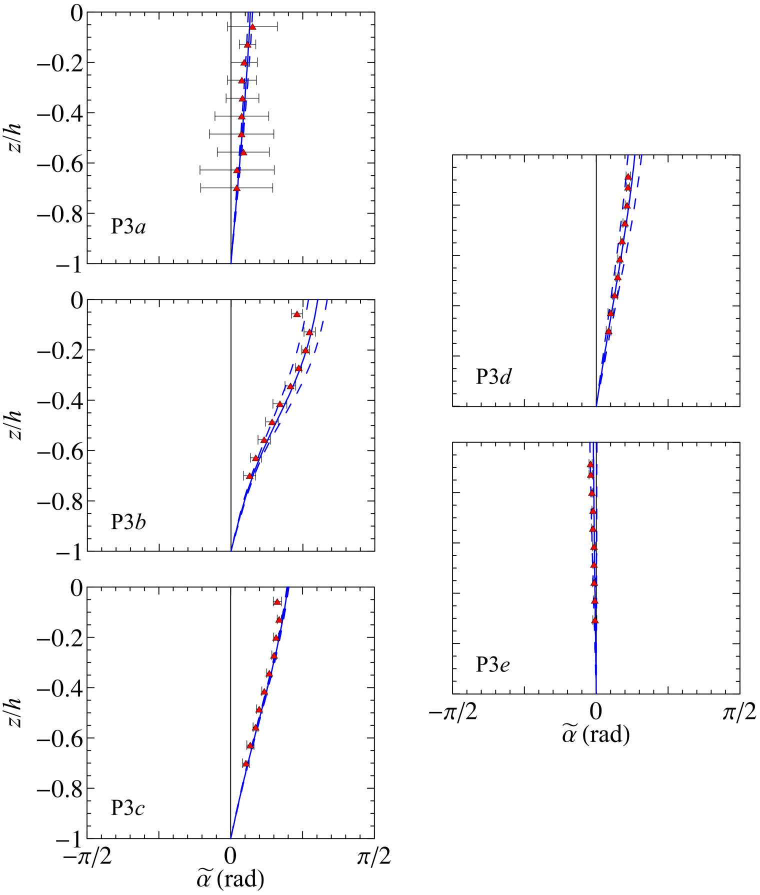

Figure 3.24: Experiments P3$a$–$e$, paddle waves (same reflection, different LDV position). Wave principal angles $\widetilde{\alpha}_p$. Red triangles are experiments, solid lines are theoretical values. Error bars are two standard deviations. Solid lines are theoretical values, dashed lines are confidence intervals to 95% level.

however, the general trend suggests that $\alpha'_{exp}$ tends to $-\pi/4$ in proximity of the water surface, and goes to zero towards the bottom (see figure 3.25).

The angle of $\pm\,\pi/4$ radians indicates the dominance of a uniform shear rate current near the free surface which is characterised by principal axes of the tensor of the velocity deformation having the same $\pm\,\pi/4$ orientation. The turbulence is still significantly isotropic, but the Reynolds stress tensor is rotated in order to gain the highest efficiency in getting energy from the mean flow field.

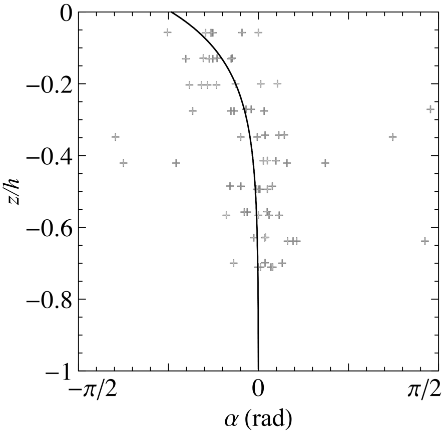

Figure 3.25: Experiments PpW, paddle waves with following wind. Symbols are the experimental turbulent principal angles $\alpha'_{exp}$. Solid lines is an empirical fitting of the experimental data.

## 3.3 Discussion of the results

We analyse experiments of paddle waves (P) and paddle waves plus following wind (PpW) in partially reflective conditions.

Free surface data show the importance of a correct reflection analysis in determining the reflection parameters $K_r$ (reflection coefficient) and $\Delta\varphi$ (phase shift between the incident and the reflected wave). The wave shape is regular for P and PpW experiments, and in the presence of wind it shows large variability (due to the generation of wind waves) and an increasing asymmetry between troughs and crests. Wind waves grow with increasing fetch length and increasing wind speed, suggesting a net energy transfer from the air side to the water side in the presence of following wind.

The observations show a spatial variation of the experimental mean water level, which can be theoretically derived and justified in terms of the radiation stress concept. We expect that also vorticity, diffusion, currents profiles are affected by partial reflection and phase shift. Hence, the free surface elevation modification induced by reflection is only one and not even the most relevant effect.

A theoretical model (described in Chapter §1) is developed to take into account the effects of partial reflection on momentum transfer. We have experimentally analyzed the vertical profiles and the horizontal variability of the Reynolds wave shear stress $-\overline{\tilde{u}\tilde{w}}$ for P and PpW experiments, under partial reflection conditions. The analysis includes the phase shift between the incident and the reflected wave, which is a novelty.

We have found that reflection plays a dominant role in modulating the Reynolds wave shear stress, which is zero only for progressive waves. Reynolds wave shear stress is usually much larger than Reynolds turbulent shear stress, even for very small reflection coefficient. As a consequence, the transport properties usually attributed to turbulence, can also be considered as a characteristic of reflected waves in a fluid domain mostly non-turbulent.

As a caveat for experimental analysis, the technique for separating periodic motion (“waves”) from “turbulence” becomes quite important to avoid pseudo-turbulence artefacts due to leakage from the organized to the fluctuating motion. Having a clear idea of the effects of partial reflection helps in the correct separation.

Reflection controls the spatial variability of the mean quantities and creates a sequence of sign-alternating vertical profiles for the Reynolds wave shear stress. The horizontal spatial average of Reynolds wave shear stress is expected to give a null contribution only if it is extended for several wave lengths and for rigorously homogeneous conditions. These conditions seldom occur in the laboratory and are absent in the field, hence a phase resolved analysis of the mean quantities is compulsory.

The experimental analysis is also extended to the mean velocities. The sheared horizontal current in the presence of wind has a vertical profile which is typical of wind-induced currents, since it is positive near the surface, i.e. co-current with the wind, and negative toward the bottom to satisfy mass conservation. The theoretical analysis and the experimental confirmation is also performed for the normal components of the Reynolds wave stress tensor. It emerges that the partial reflection exerts a major influence on the horizontal normal stress $\overline{\tilde{u}\tilde{u}}$, while the vertical component

$\overline{\widetilde{w}\widetilde{w}}$ is almost independent with respect to the reflective conditions.

The Reynolds turbulent shear and normal stresses are measured and manifest themselves smaller of one order of magnitude (or more) than their wave-induced counterparts. Experimental observations suggest that partial reflection induces an increment of turbulence in the flow field. In order to get more insights about the turbulence structure, a quadrant analysis is performed in the water domain and the results indicate a major contribution of the inward and outward interactions, with an overall net momentum transfer from the air side to the water side due to the turbulent shear stress.

A complete analysis of the Reynolds stress tensors (wave and turbulent) is conducted to define the principal stresses and the principal angle. The measured values indicate that the Reynolds wave stress tensor is well described by the theoretical model and is influenced by the reflection parameters. The Reynolds turbulent stress tensor is experimentally investigated and reveals the different behaviour of the turbulent stresses in the presence and in the absence of wind, highlighting the importance of a correct description of the interaction between swell waves and wind at the interface.

# Chapter 4

# Paddle waves with opposing wind

In this Chapter, we analyse regular waves generated by paddles in partially-reflective conditions, under the action of wind blowing in the opposite direction.

The first aim is to check again the model developed in Chapter §1: the Reynolds wave shear stress is again calculated in the vertical both theoretically and experimentally, as well as the mean water level and the total wave height.

Since free surface data were acquired (within the same experiment) with and without wind, it is possible to compare directly the effects of opposing wind action on the wave field, in particular on the reflective conditions.

Statistics of the fluctuating components of the free surface data (i.e., the wind waves) are calculated as function of the fetch length and for different reflective conditions. The dispersion relation model suggested by Swan & James (2000), which includes the shear of the current induced by the wind in the wave flume, is then compared with the experimental phase and group celerities of the wind waves.

The Reynolds wave stress tensor is analysed by using the theoretical model and by means of data analysis, in order to compare the analytical and experimental results. The experimental Reynolds turbulent stresses are also reported. Some insights on the turbulent flow of the wind waves are investigated through the quadrant analysis and the joint probability density functions of the non-dimensional horizontal and vertical fluctuating velocities. This technique yields the determination of the dominant events in the process and the direction of momentum transfer at the interface between air and water.

## 4.1 Experiments

Eight experiments were performed with parameters listed in Table 4.1. All the experiments have the same nominal characteristics of the paddle wave and the same wind speed and direction. For the first five experiments PoW1-5 (the acronym PoW standing for "Paddle waves with opposing Wind") the LDV system was located in the same $x$ position and the absorption conditions were varied for each experiment. The last three experiments (PoW2$b$-$c$-$d$) had the same wave statistics and reflective conditions of test PoW2$a$; however, the LDV probe was positioned in a different section $x/L$ along the flume, in order to evaluate the spatial variations of velocities correlations and stresses. Before starting the LDV acquisitions, five minutes of only-paddle generated waves (without wind) were used to measure the water surface displacement. That procedure was followed for each test with the aim of estimating the effect of wind on the flow field, in particular on reflective conditions and free surface statistics, compared to no-wind conditions.

| Expts | $u_{*a}$ ($\mathrm{cm\,s^{-1}}$) | $x/L$ | $H_i$ (cm) | $H_t$ (cm) | $T$ (s) | $K_{r,w}$ | $\Delta\varphi$ (rad) |
|---|---|---|---|---|---|---|---|
| PoW1 | 75.2 | -0.27 | $3.8 \pm 0.1$ | $6.3 \pm 0.1$ | 1.6 | $0.745 \pm 0.003$ | $3.92 \pm 0.03$ |
| $2a$ | 75.2 | -0.27 | $4.3 \pm 0.1$ | $6.3 \pm 0.1$ | 1.6 | $0.595 \pm 0.004$ | $3.95 \pm 0.03$ |
| 3 | 75.2 | -0.27 | $5.4 \pm 0.1$ | $5.7 \pm 0.1$ | 1.6 | $0.306 \pm 0.007$ | $4.21 \pm 0.04$ |
| 4 | 75.2 | -0.27 | $5.4 \pm 0.1$ | $5.1 \pm 0.1$ | 1.6 | $0.12 \pm 0.01$ | $4.57 \pm 0.06$ |
| 5 | 75.2 | -0.27 | $5.3 \pm 0.1$ | $4.9 \pm 0.1$ | 1.6 | $0.066 \pm 0.006$ | $5.78 \pm 0.17$ |
| $2b$ | 75.2 | -0.23 | $4.3 \pm 0.1$ | $7.7 \pm 0.1$ | 1.6 | $0.608 \pm 0.004$ | $3.95 \pm 0.03$ |
| $2c$ | 75.2 | -0.19 | $4.3 \pm 0.1$ | $8.5 \pm 0.1$ | 1.6 | $0.607 \pm 0.005$ | $3.92 \pm 0.03$ |
| $2d$ | 75.2 | -0.14 | $4.3 \pm 0.1$ | $8.6 \pm 0.1$ | 1.6 | $0.606 \pm 0.004$ | $3.91 \pm 0.03$ |

Table 4.1: Parameters of the experiments, PoW stands for "Paddle waves with opposing Wind". $u_{*a}$ is the air friction from Pitot measures, $H_i$ is the incoming wave height, $H_t$ is the total wave height, $T$ is the period of the paddle oscillation, $K_r$ and $\Delta\varphi$ are the reflection coefficient and the phase shift, respectively. The relative coordinate $x/L$ indicates the LDV measurement section (position) with respect to US8 (see Figure 2.1b). Experiments 1–5 have same paddle nominal incident wave height $H_i$ and period $T$, and same wind speed, but different reflective conditions. Experiments $2a$–$d$ have same paddle, wind and reflective conditions, but different LDV position.

## 4.2 Analysis of the results

### 4.2.1 Free surface data

For each PoW experiment, free surface data were acquired in two conditions: (i) with paddle waves (no wind), (ii) with paddle waves plus opposing wind. Phase average of the free surface data and reflection analysis were performed in both situations in order to compare the results and to identify the effects of the wind on the periodic wave component.

Figure 4.1 shows the phase-averaged wave profile for experiments PoW1-5 at different sections; for clarity, only sensors US1-3-5-8 are reported. In the absence of wind, the wave shape is regular with null (or very little) deviations; for lower reflection, it is almost uniform along the flume, while it is modulated in amplitude for increasing reflection coefficients $K_r$. When opposing wind is present, the wave profile shows larger deviations (of the order of wind waves height), but for lower reflection the mean wave shape is still regular. We notice that: (i) for higher reflective conditions, i.e. larger reflection coefficient $K_r$, there is a modulation of the wave height stronger than in the absence of wind, and in general an attenuation of the wave height; (ii) the mean wave profile is almost identical in both conditions (with and without wind) for lower $K_r$, but at increasing reflection a significant distortion of the wave shape is observed.

A quantitative evaluation of the wave profile can be obtained through the analysis of total wave height, considering the periodic component of the free surface. The total wave height $H_t$, resulting from the interaction between the incident and the reflected waves, can be derived theoretically at different sections from the envelope of the free surface level, which at the first order is calculated from equation (1.12) as

$$\widetilde{\eta}(x,t) = a_i[\cos(kx - \omega t) + K_r \cos(kx + \omega t + \Delta\varphi)], \tag{4.1}$$

where $a_i = H_i/2$ is the incident wave amplitude, $K_r$ the reflection coefficient and $\Delta\varphi$ the phase shift between the incident and the reflected wave. The reflection parameters $K_r$ and $\Delta\varphi$ are evaluated from the reflection analysis described in §2.3.3. The difference between the minima and the maxima of

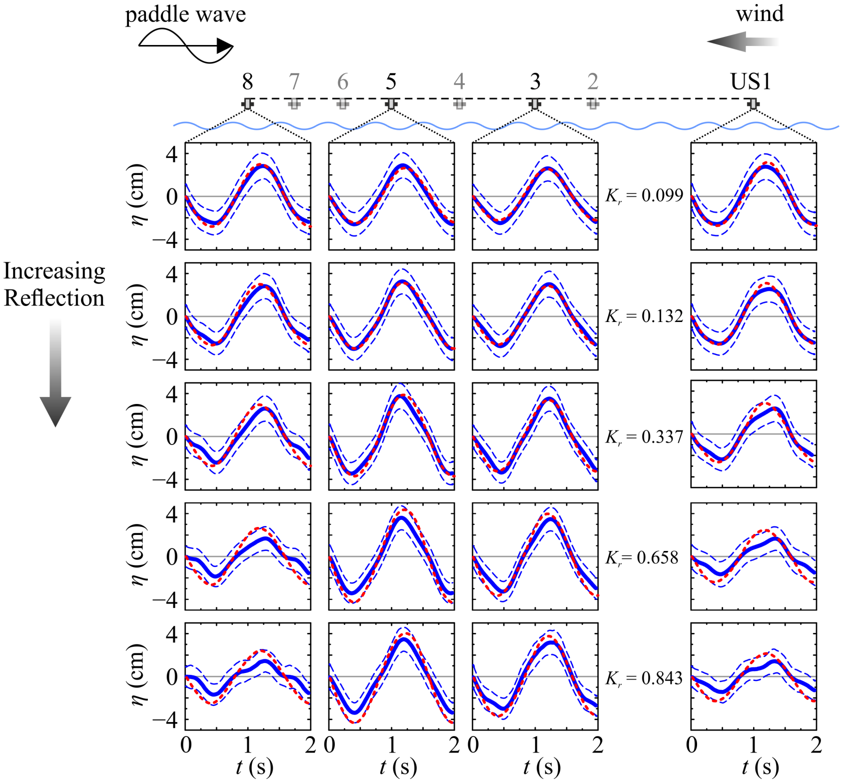

Figure 4.1: Phase-averaged wave profiles for different reflective conditions. Red dotted lines refer to paddle waves (in the absence of wind), blue solid lines refer to paddle waves with opposing wind (dashed lines are one standard deviation in the presence of wind). Only signals for sensors US1-3-5-8 are shown for clarity. $K_r$ is the reflection coefficient calculated in the absence of wind.

the envelope represents the total wave height $H_t$ at different sections along the flume.

The experimental $H_t$ of the periodic component is obtained by band-passing the spectrum of the US signal in the range $0.5 < fT < 1.5$, where $T$ is the measured wave period of the paddle wave (coincident with the imposed value) and $f$ is the frequency of the spectrum. The total wave height is measured also for only-paddle waves (in the absence of wind) for the same experiments. Figure 4.2 shows the total wave amplitude $a_t = 1/2\, H_t$ as function of the non-dimensional coordinate $x/L$, where the wave length $L$ is calculated from linear dispersion relation $\omega^2 = gk \tanh kh$ applied to the peak frequency of the spectrum. The results show a good agreement between theory and experiments; it emerges that reflection modulates the wave amplitude along the channel for both conditions (with and without wind), and also for small values of $K_r$ and $\Delta\varphi$. In particular, opposing wind causes an attenuation of the wave height and a shift of nodes and antinodes position along the flume, with respect to only-paddle waves (no wind).

The comparison between no-wind and wind conditions confirms that the presence of wind influences also the reflection parameters $K_r$ and $\Delta\varphi$. This influence is investigated as function of the reflective conditions. In particular, figure 4.3 shows the difference of the phase shift $\Delta\varphi_w - \Delta\varphi$ and the reflection coefficient $K_{r,w} - K$ between no-wind (no subscript) and wind (subscript "w") conditions. We notice that an opposing wind induces: (i) an attenuation of $K_r$, which increases for higher reflective conditions ($K_r - K_{r,w}$ decreases for increasing $K_r$); (ii) a positive shift of $\Delta\varphi_w - \Delta\varphi$, which denotes a phase lag of $\approx -\pi/8$ radians and is almost independent on $K_r$.

The analytical description of the wave field derived in Chapter §1 predicts a spatial variation of the mean water level by means of the radiation stress concept, which represents the depth-averaged excess of momentum due to the presence of the wave. The theoretical mean water level is represented by equation (1.24) and reads

$$\bar{\eta} = k a_i^2 K_r \coth(2kh) \cos(2kx + \Delta\varphi) + \text{const}, \tag{4.2}$$

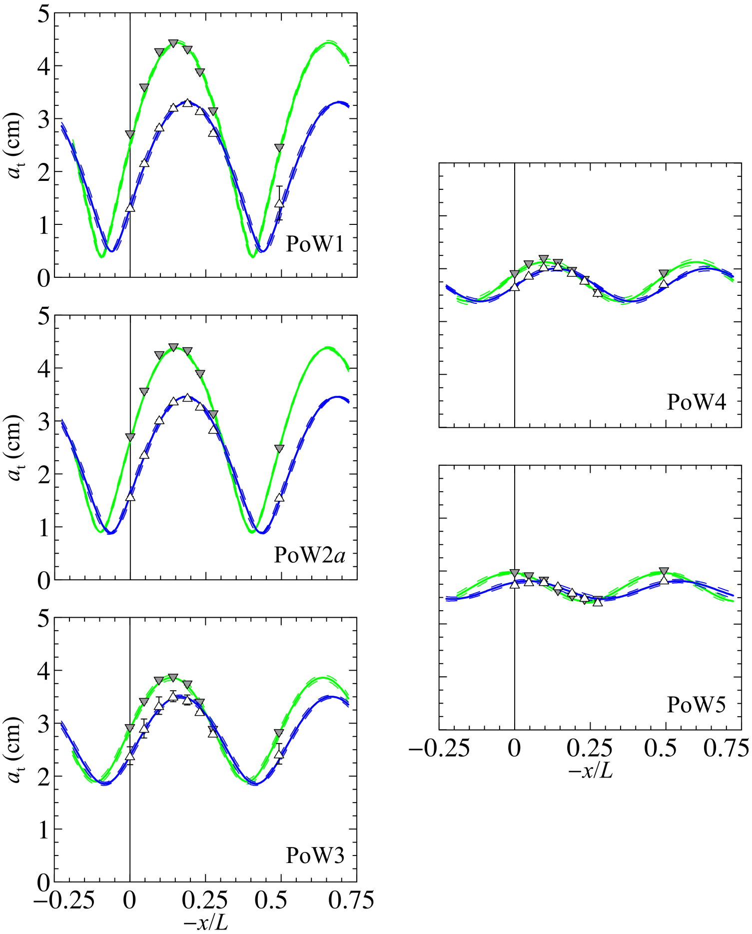

Figure 4.2: Spatial modulation of the wave amplitude $a_t = H_t/2$, experiments PoW1-5 (different reflective conditions, same LDV section). Lines refer to the theory for waves without wind (green lines) and waves with opposite wind (blue lines). Symbols are experimental values for no-wind (down-pointing grey triangles) and wind (up-pointing blank triangles) conditions, with error bars equal to two standard deviations.

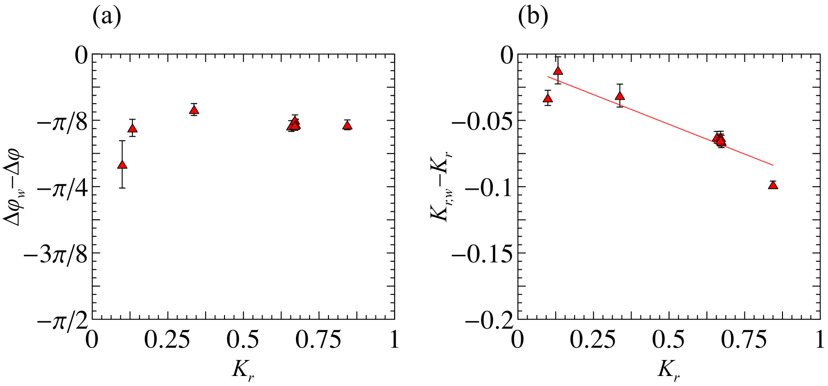

Figure 4.3: Influence of opposing wind on the paddle waves reflection parameters for varying reflection. *a*) Variation of the phase shift $\Delta\varphi_w - \Delta\varphi$ in the presence of wind; *b*) Attenuation of the reflection coefficient $K_r$ in the presence of wind, solid line is a linear interpolation of the experimental data (symbols). Subscript "w" indicates the presence of wind, no subscript indicates the absence of wind. Error bars are two standard deviations.

where the constant is imposed by mass conservation.

Figure 4.4 shows the comparison theoretical mean water level (MWL) and the experimental values. In our analysis, the experimental values, which are the time average of the free surface data. Most measurements show a displacement of the same order of the instrumentation accuracy ($\approx$ 0.8 mm), nonetheless the spatial modulation induced by reflection is remarkable and results in agreement with theoretical predictions.

### Statistics of wind waves

The wind waves component of the free surface data is extrapolated through a high-pass filter applied to the power density spectrum (see §2.3.3). A zero-crossing analysis of the resulting signal is performed in each US measurements section and yields the main statistics of the wave height and period. In particular, the analysis is carried out for the root-mean-squared wave height $H_{\text{rms}}$, for the mean wave height $H_{\text{m}}$ and period $T_{\text{m}}$, and for

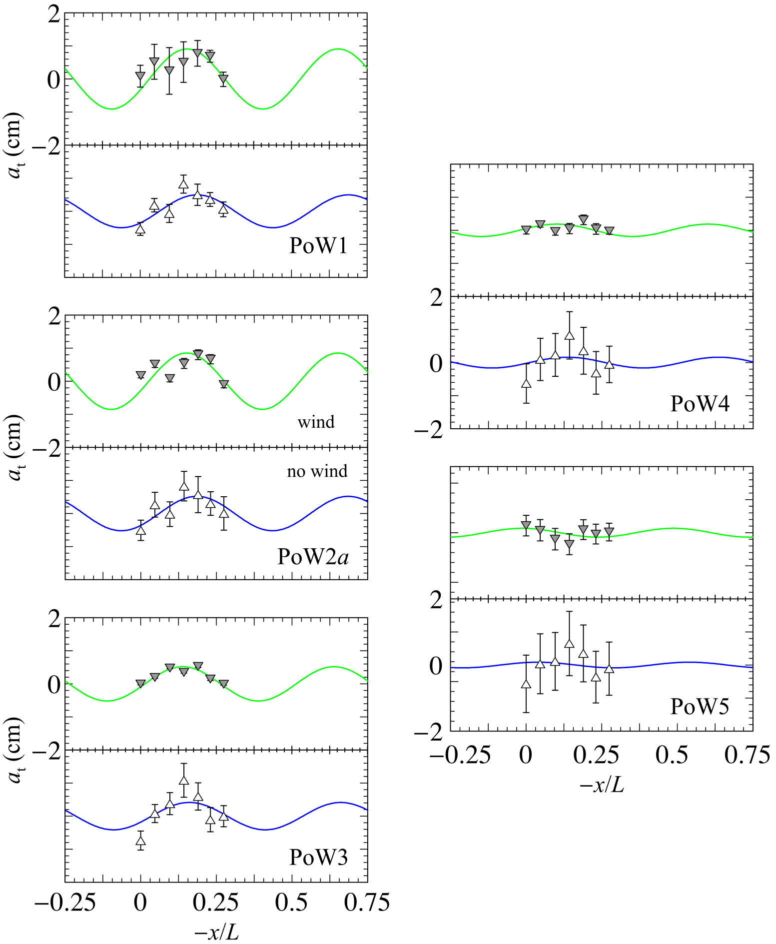

Figure 4.4: Theoretical (solid lines) and experimental (symbols) mean water level $\bar{\eta}$, experiments PoW1–5. Theoretical lines derive from equation (4.2) for mean water level, using reflection parameters for no-wind (green) and wind (blue) conditions. Symbols represent mean water level for paddle-generated waves in the absence of wind (down-pointing grey triangles) and paddle-opposing wind waves (up-pointing blank triangles). Error bars are two standard deviations.

$H_{1/3}$, $T_{1/3}$, $H_{1/10}$ and $T_{1/10}$, which represent the average of the one third and one tenth maximum wave height and period, respectively.

Figure 4.5 shows a separate analysis of the mean peak period $T_{\mathrm{m}}$ as function of the fetch. The growth of the wave peak period is well defined for all the tests and monotonic, coherently with the results of figure 4.7b).

Some insights on the trend of the wind waves height are gained by separately analysing the root mean square height. Figure 4.6 shows $H_{\mathrm{rms}}$ as function of the fetch for each experiment. In this case, the general behaviour suggests an initial growth of the wind waves height, with a subsequent reduction. Probably it happens for two reasons: i) US sensors might not be far enough to capture the fetch wave growth; ii) due to the wind conditions, wind-generated waves are fully-developed in the measurement sections and experience micro-breaking, dissipating energy.

Figures 4.7a) and 4.7b) report the results of all the statistics for wind waves height and period. The pattern of the wind waves height is not very clear, and a wave growth or decay is not evident at different fetch lengths. However, the statistical estimators grow from the mean height $H_{\mathrm{m}}$ to $H_{1/10}$. The trend of the only-wind wave peak period $T$ as function of $x$ is more evident: the experimental points grow almost monotonically for $T_{\mathrm{m}}$, $T_{1/3}$ and $T_{1/10}$, and the values of $T_{1/3}$ and $T_{1/10}$ converge at the maximum fetch.

A comparison between the wind wave root mean square height and mean peak period for different experiments exhibits a dependence on reflective conditions. Figures 4.8 and 4.9 report $H_{\mathrm{rms}}$ and $T_{\mathrm{m}}$ as function of the reflection coefficient $K_r$. The root mean square height appears to decrease for increasing reflective conditions, but not monotonically; the experimental points suggest that a maximum wind wave height is reached around $K_r \approx 0.25$, even though it varies at different US measurement sections (i.e., at different fetch). An initial increasing and later decreasing of the experimental values is observed also for the wind wave mean peak period $T_{\mathrm{m}}$, even though in this case the maximum is reach for $K_r \approx 0.6$.

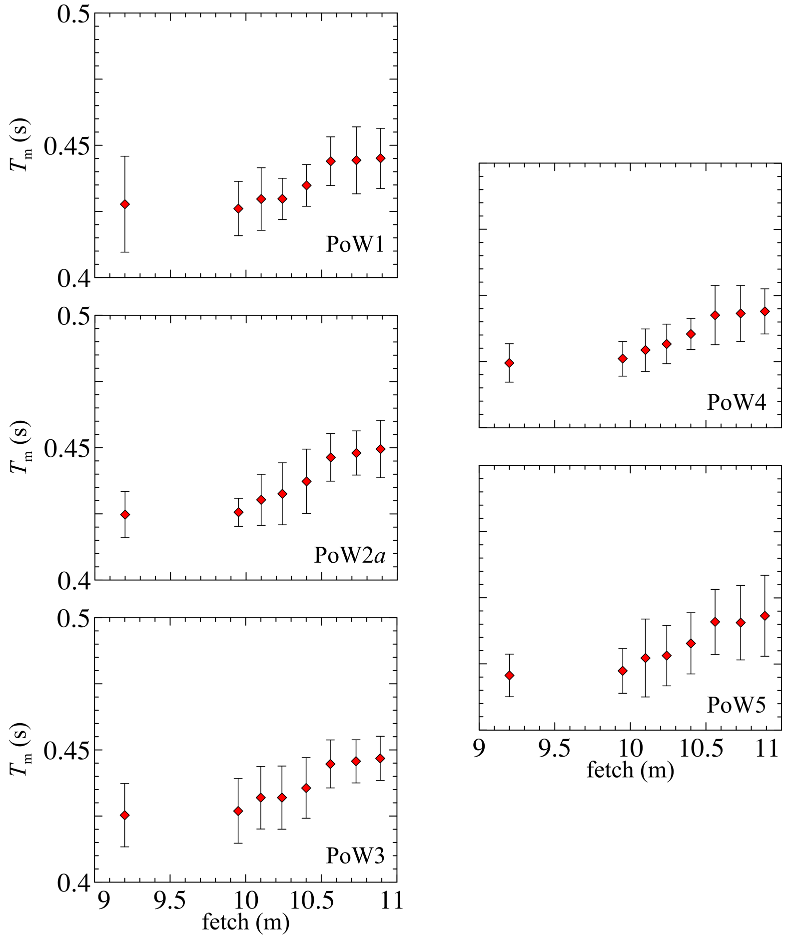

Figure 4.5: Mean peak period $T_{\mathrm{m}}$ as a function of the fetch length. Symbols are experimental points, error bars are two standard deviations.

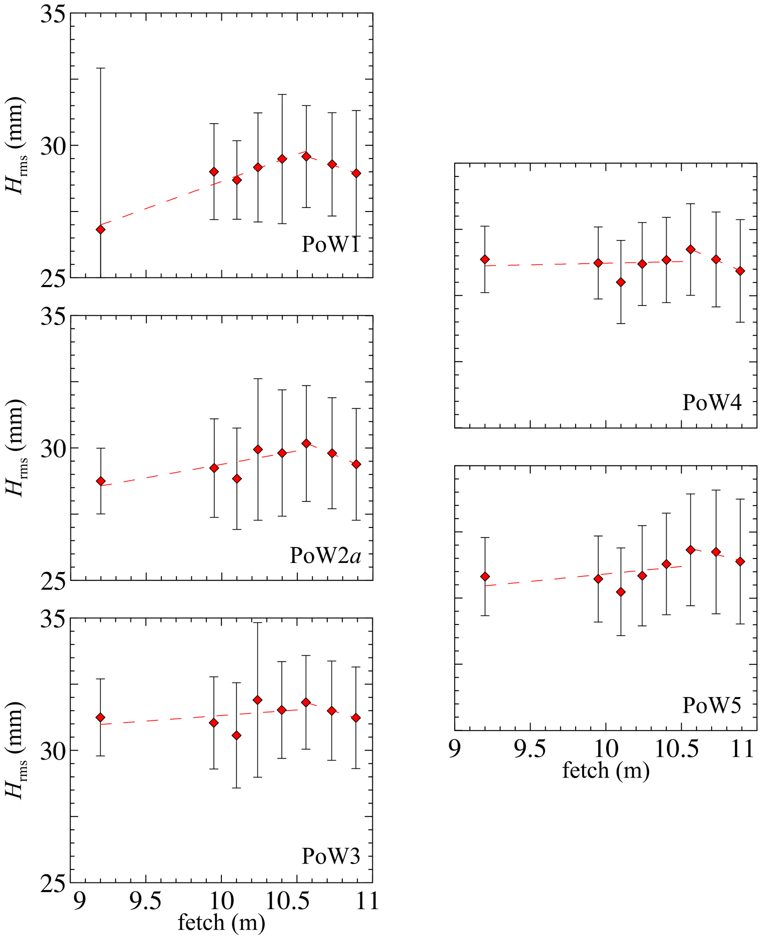

Figure 4.6: Root mean square wave height $H_{rms}$ as a function of the fetch length. Symbols are experimental points, dashed lines are the general trend. $H_{rms}$ slightly increases with fetch and then starts to decrease, possibly due to micro-breaking which dissipates part of the wave energy.

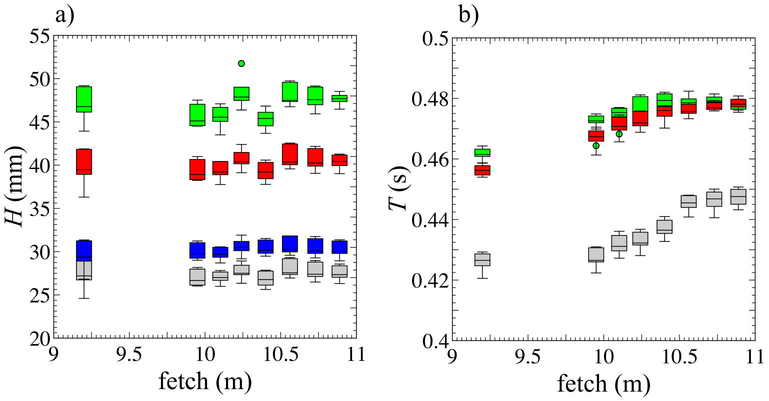

Figure 4.7: Experimental wind waves height (a) and peak period (b), as a function of the fetch length, represented by box plot whiskers, which indicate the minimum value and the maximum values, the upper and the lower quartiles and the median. Grey box represents mean wave height $H_\mathrm{m}$ and period $T_\mathrm{m}$, blue box represents the root mean square wave height $H_\mathrm{rms}$, red box and green box represent the average of the one third ($H_{1/3}$ and $T_{1/3}$) and one tenth ($H_{1/10}$ and $T_{1/10}$) maximum wave height and peak period, respectively. Circles are outliers.

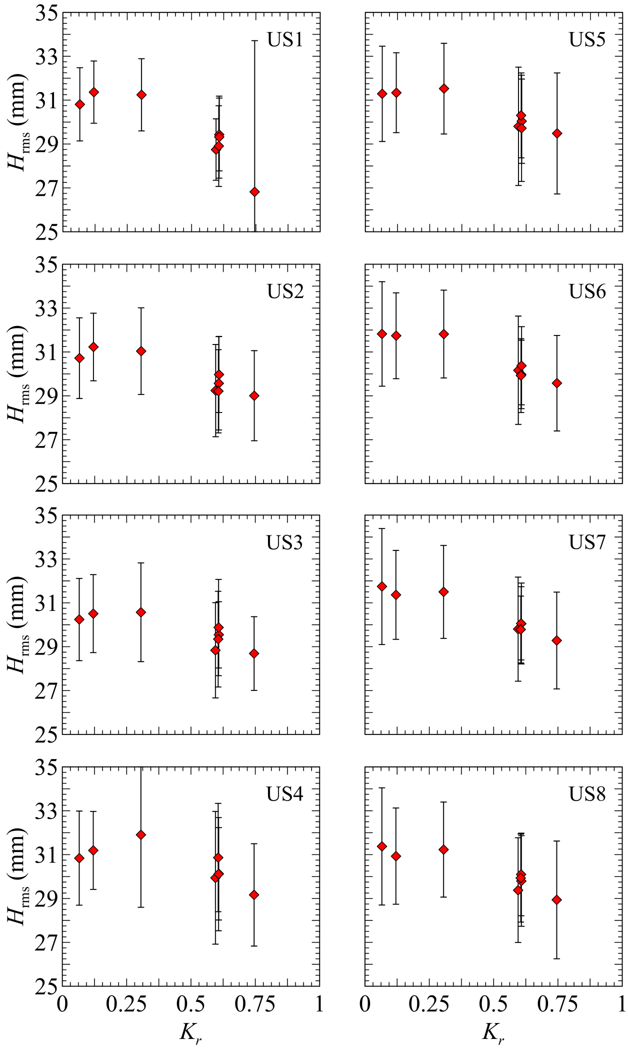

Figure 4.8: Experimental root mean square wave height $H_{\rm rms}$ (symbols) at each US section, as function of the reflection coefficient $K_r$. Error bars stand for a confidence interval at 95%.

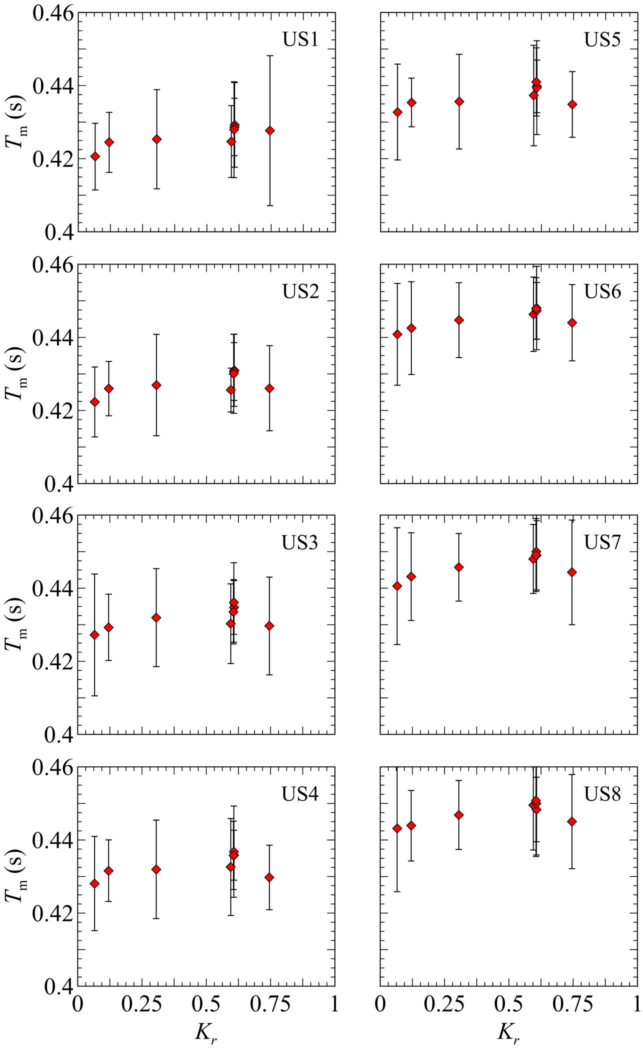

Figure 4.9: Experimental mean peak period $T_m$ (grey diamonds) at each US section, as function of the reflection coefficient $K_r$. Error bars stand for a confidence interval at 95%.

### Phase and group celerities of wind waves

The analysis of the wind wave phase celerity $c$ is performed both theoretically and experimentally. The triple composition technique assumes a linear superposition of the mean, the periodic and the fluctuating component. For free surface data, it means that wind waves are linearly combined with the periodic component (which is represented by the paddle wave) and propagate with their own phase celerity. In this sense, we neglect nonlinear direct interaction between the periodic and fluctuating components.

The experimental evaluation of the phase celerity is conducted through the cross-correlation of the signals of two adjacent US sensors, while the theoretical phase celerity is evaluated by using the analytical model by Swan & James (2000). The group celerity $c_g$, which indicates the speed of propagation of the wave energy packets, is evaluated experimentally and represents the delay of the maximum of the cross-correlation envelope.

The main parameters (US sensor, mean position, mean phase celerity, peak frequency, wave number and mean group celerity) are calculated for all the tests; as an example, in Table 4.2 we report the results for PoW1.

Figure 4.10 reports a graphic vision of the phase celerity as a function of the wave number $k$ for experiments PoW1–5 (different reflective conditions), with a comparison between theoretical and experimental values. The classical linear dispersion relation always underestimates the experimental values. It is a consequence of the fact that the linear dispersion relation does not take into account the influence of the sheared current beneath the free surface. In fact, results show also that considering the nonlinear influence of the current profile (through the model defined by Swan & James, 2000) results a good interpretation of the experimental points, which fit the theoretical profile within the experimental uncertainties.

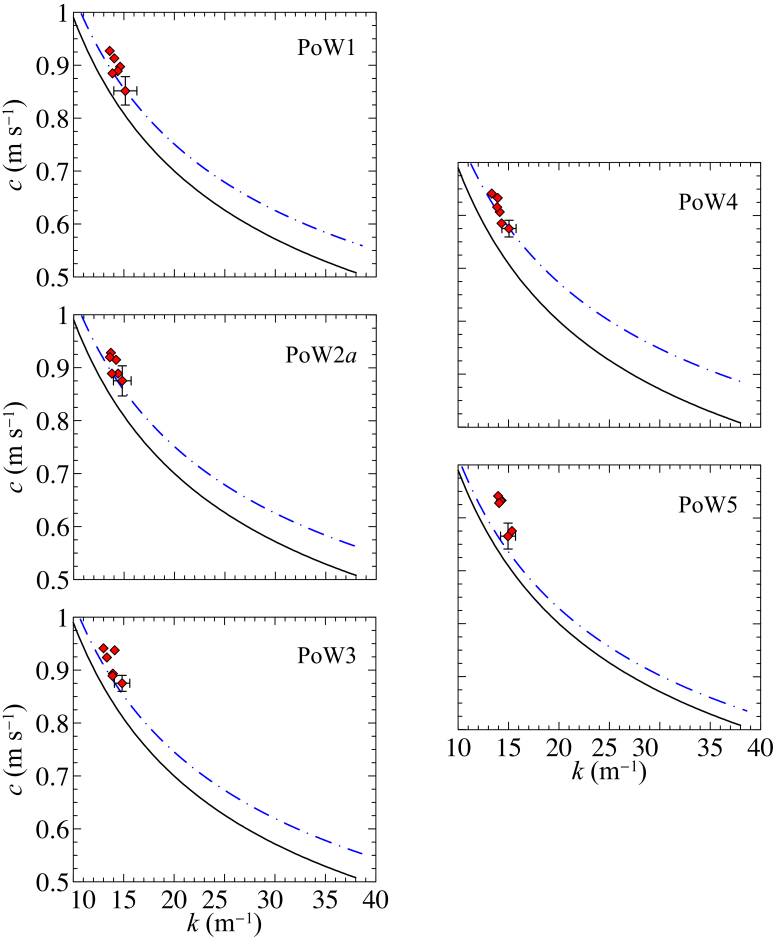

Figure 4.10: Experiments PoW1–5, paddle waves with opposing wind (different reflection, same LDV position). Theoretical (solid and dashed lines) and experimental (symbols) phase celerities $c$. The black solid line indicates $c$ derived from linear dispersion relation $\omega^2 = gk \tanh kh$, while the colored dashed line represents the phase celerity derived by Swan & James (2000). The experimental phase celerity error bars are one standard deviation.

| Section | $x$ (m) | $c_{\text{ave}}$ ($\mathrm{m\,s^{-1}}$) | $f_{peak}$ $\mathrm{s^{-1}}$ | $k_{peak}$ $\mathrm{m^{-1}}$ | $c_{g,\text{ave}}$ ($\mathrm{m\,s^{-1}}$) |
|---|---|---|---|---|---|
| U2 | -0.94 | - | - | - | - |
| | | $0.90 \pm 0.03$ | 1.91 | $14.6 \pm 0.8$ | $0.69 \pm 0.04$ |
| U3 | -0.79 | $0.87 \pm 0.03$ | | | |
| | | $0.85 \pm 0.03$ | 1.94 | $15.1 \pm 1.1$ | $0.64 \pm 0.01$ |
| U4 | -0.65 | $0.87 \pm 0.03$ | | | |
| | | $0.89 \pm 0.01$ | 1.89 | $14.4 \pm 0.9$ | $0.67 \pm 0.04$ |
| U5 | -0.49 | $0.91 \pm 0.03$ | | | |
| | | $0.93 \pm 0.02$ | 1.84 | $13.6 \pm 0.7$ | $0.72 \pm 0.02$ |
| U6 | -0.33 | $0.92 \pm 0.03$ | | | |
| | | $0.91 \pm 0.03$ | 1.87 | $14.0 \pm 0.8$ | $0.81 \pm 0.03$ |
| U7 | -0.16 | $0.89 \pm 0.03$ | | | |
| | | $0.88 \pm 0.01$ | 1.86 | $13.9 \pm 0.6$ | $0.83 \pm 0.03$ |
| U8 | 0 | - | - | - | - |

Table 4.2: Mean phase and group celerities for wind waves of PoW1. The position $x$ indicates the fetch of US measurements, while $c_{\text{ave}}$ is the phase celerity evaluated through a cross-correlation analysis. The frequency peak $f_{peak}$ is the peak of the spectrum of the wind-generated waves (after that the periodic component is removed), the wave number $k_{peak}$ is computed as $2\pi f_{peak}/c_{\text{ave}}$, and the group celerity $c_{g,\text{ave}}$ is evaluated from the envelope of the cross-correlation between two adjacent signals.

### 4.2.2 Horizontal and vertical mean velocity

The separation of the of the horizontal $\overline{u}$ and vertical $\overline{w}$ mean flow is performed by time averaging the LDV signal.

In the presence of opposing wind, the horizontal velocity is positive, i.e. cocurrent with the wind, near the free surface, while becomes negative at lower levels. It is true for all the experiments conducted, for different reflective conditions and same LDV measurement section (experiments PoW1–5, figure 4.11) and for same reflective conditions and different LDV measurement sections (experiments PoW2$a$–$e$, figure 4.12). The measured vertical velocities tend to negative values in proximity of the free surface, while it is always positive toward the bottom. The same behaviour was observed for experiments PpW (paddle waves plus following wind, see §3.2.4); we expect positive currents in direction of the wind near the surface, and a non-null vertical velocity due to the normal pressure of the atmospheric forcing. Mass conservation and the finite length of the channel imply that horizontal and vertical flows have to change signs in order to be in balance. Also longitudinal and transversal circulation, due to the action of wind and to the finite length of the channel, can influence both the horizontal and the vertical velocity. The combination of a positive horizontal and a negative vertical mean velocity near the free surface suggests a net momentum transfer (due to the mean components) from the air side (wind) to the water.

### 4.2.3 Reynolds wave and turbulent stresses

Once the mean velocity is subtracted to the LDV signals, a phase average yields the periodic component for both horizontal $\widetilde{u}$ and vertical $\widetilde{w}$ velocity. Thus, the fluctuating velocities (horizontal $u'$ and vertical $w'$) are obtained as the remaining of the LDV signal after phase and time averages.

If the same operations of time and phase average are performed to the momentum equations, we can divide the contribution of the Reynolds wave stress tensor, with components $\overline{\widetilde{u}\widetilde{u}}$, $\overline{\widetilde{w}\widetilde{w}}$ and $\overline{\widetilde{u}\widetilde{w}}$, and the Reynolds turbulent stress tensor, with components $\overline{\widetilde{u'u'}}$, $\overline{\widetilde{w'w'}}$ and $\overline{\widetilde{u'w'}}$.

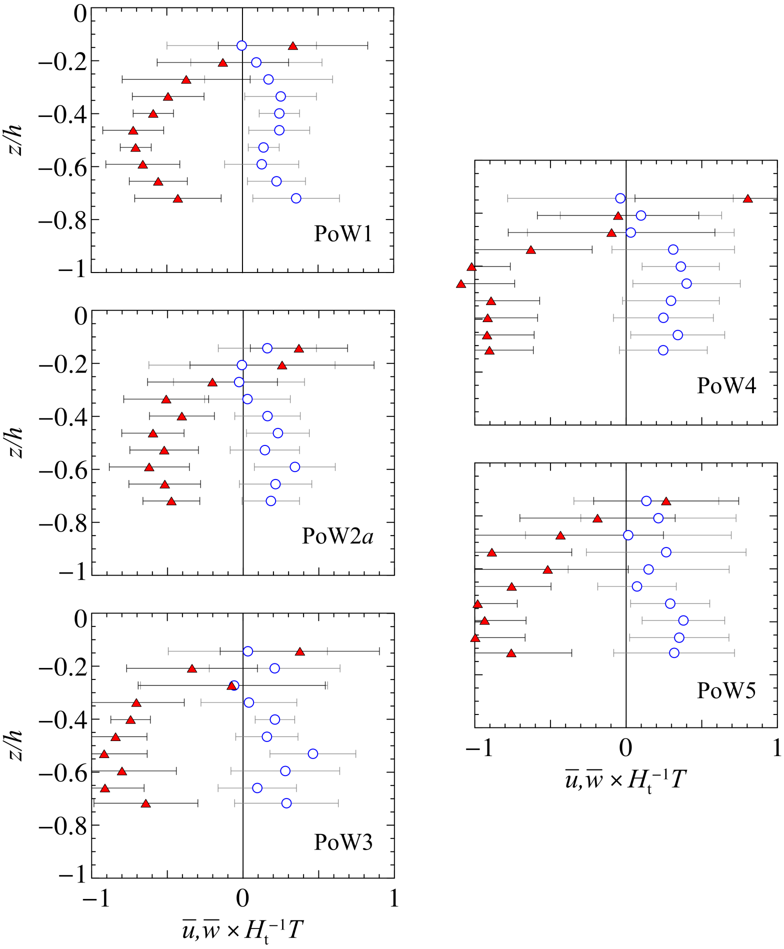

Figure 4.11: Experiments PoW1–5, paddle waves with opposing wind (different reflective conditions, same LDV section). Mean horizontal $\overline{u}$ (red filled triangles) and vertical $\overline{w}$ (empty circles) velocities, non dimensional with respect to the velocity scale $H_t T^{-1}$. Error bars are one standard deviation.

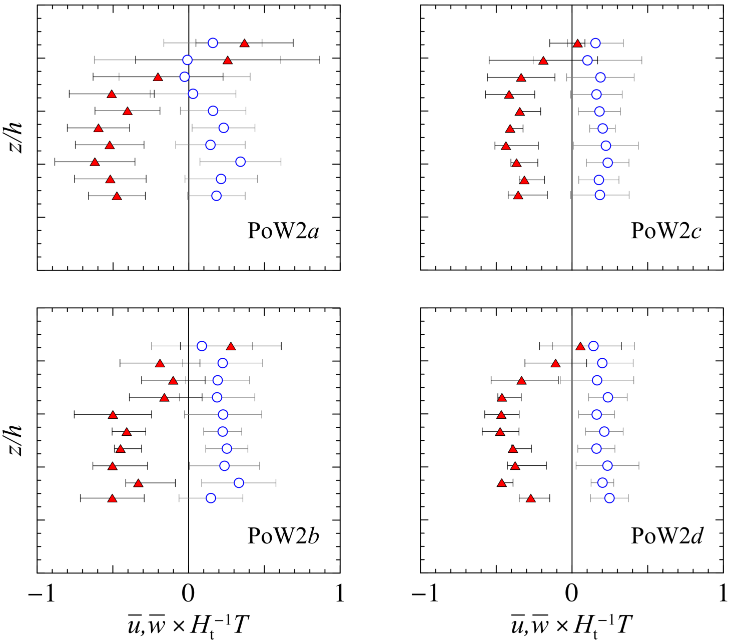

Figure 4.12: Experiments PoW2*a*–*d*, paddle waves with opposing wind (same reflective conditions, different LDV measurement sections). Mean horizontal $\overline{u}$ (red filled triangles) and vertical $\overline{w}$ (empty circles) velocity, non dimensional with respect to $H_tT^{-1}$. Error bars are one standard deviation.

The theoretical model of Chapter §1 gives the tools to analyse the Reynolds wave stresses. From (1.13), the vertical profile of the Reynolds wave shear stress can be expressed at the first order as

$$-\overline{\tilde{u}\tilde{w}} = gka_i^2 \frac{\sinh\left[2k\left(z+h\right)\right]}{\sinh\left(2kh\right)} K_r \sin(2kx + \Delta\varphi). \tag{4.3}$$

We highlight the importance of the term $-\overline{\tilde{u}\tilde{w}}$, since for progressive waves it is null and appears with partial reflection conditions. We have shown in Chapter §3 that neglecting this term, also for small values of the reflection coefficient and phase shift, could lead to significant errors in the interpretation of the data in laboratory and field campaigns.

Figure 4.13 shows the comparison between theoretical and experimental values of $-\overline{\tilde{u}\tilde{w}}$, for different reflective conditions (experiments (PoW1–5). Figure 4.14, reports the results of $\overline{\tilde{u}\tilde{w}}$ for experiments 2*a*–*d*, which were done in similar reflective conditions but different LDV measurement sections in order to observe the spatial variation. As found in the previous Chapter (§3) and also in literature (see Olfateh *et al.*, 2017), the Reynolds wave shear stress $\overline{\tilde{u}\tilde{w}}$ determines momentum transfer with different sign and intensity, depending on reflective conditions and measurement position in $x$, and its value is also predictable with an appropriate reflection analysis.

We remind that the reflection analysis (see 2.3.3) is based on the US signals. Since we had two different US acquisitions for each experiment, one with only paddle waves (no wind) and one with paddle waves plus opposing wind, two different vertical profiles of the theoretical $\overline{\tilde{u}\tilde{w}}$ are calculated. The reflection parameters used to obtain a good theoretical fit with the experimental velocity correlation are those with paddle waves plus opposing wind; for only-paddle waves the vertical profile changes significantly. It is a further checked that the presence of opposing wind modifies the reflection coefficient $K_r$ and the phase shift $\Delta\varphi$, as reported in §4.2), and it affects also the wave shear stress (thus the net momentum transfer at the interface between air and water).

The terms $\overline{\tilde{u}\tilde{u}}$ and $\overline{\tilde{w}\tilde{w}}$ represent the diagonal components (i.e., the normal stresses) of the second-order Reynolds wave stress tensor, represented in equation (1.25). Their theoretical relation derives from the solution of

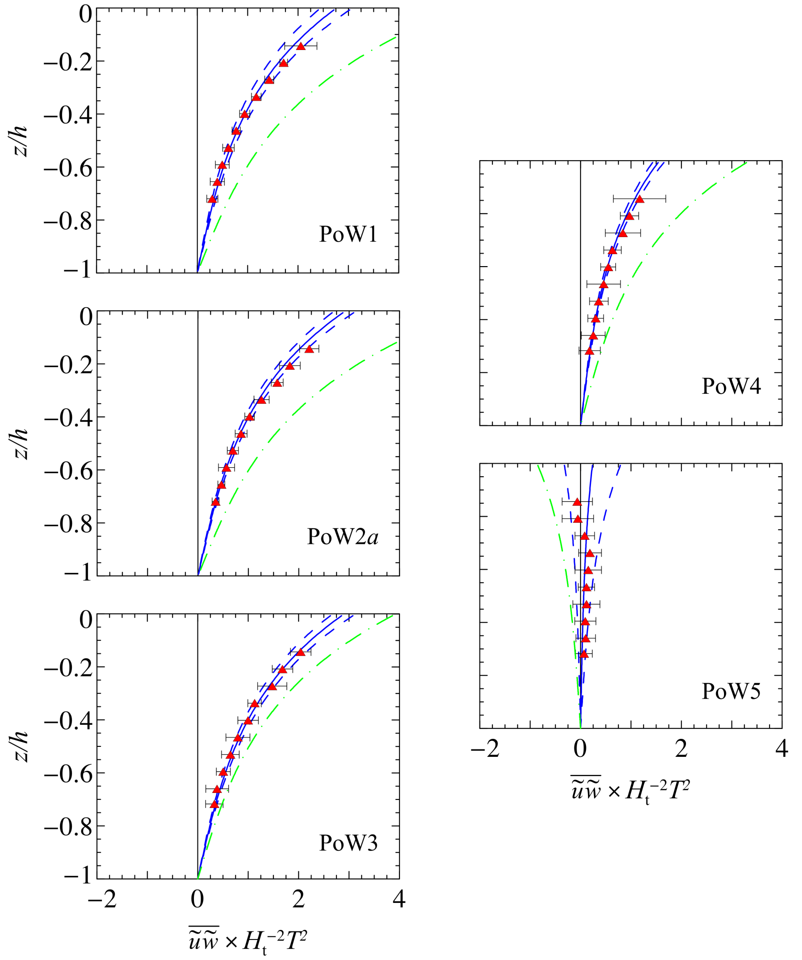

Figure 4.13: Experiments PoW1–5, paddle waves with opposing wind (different reflective conditions). Vertical profile of the wave velocity covariance $\overline{\widetilde{u}\widetilde{w}}$. Solid lines represent theoretical velocity correlation at first order, while symbols are experimental data. Dashed lines are confidence interval with probability of 95%. In blue, reflection parameters $K_r$ and $\Delta\varphi$ are evaluated in the presence of wind, while in green they are evaluated without wind.

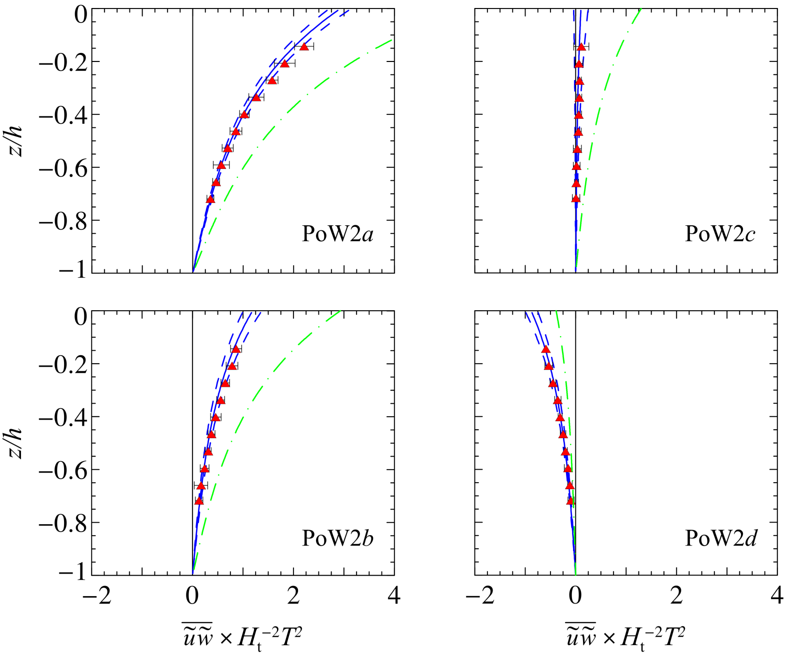

Figure 4.14: Experiments PoW2$a$–$d$, paddle waves with opposing wind (same reflection conditions, different LDV section). Vertical profile of the Reynolds wave shear stress $\overline{\tilde{u}\tilde{w}}$. Solid lines represent theoretical velocity correlation at first order, symbols are experimental data. Dashed lines are confidence interval with probability of 95%, error bars two standard deviations. In blue solid line, reflection parameters $K_r$ and $\Delta\varphi$ are evaluated in the presence of wind, while in green dash-dotted line $K_r$ and $\Delta\varphi$ are evaluated without wind.

the analytical model of Chapter §2; in particular, the horizontal wave normal stress $\overline{\tilde{u}\tilde{u}}$ is the time average of the product of the horizontal velocity of equation (1.10), and at the first order reads

$$\overline{\tilde{u}\tilde{u}} = gka_i^2 \frac{\cosh\left[k\left(z+h\right)\right]}{\sinh\left(2kh\right)}\left[1+K_r^2-2K_r\cos(2kx+\Delta\varphi)\right]. \tag{4.4}$$

Analogously, time averaging the product of the vertical velocity of equation (1.11) yields the vertical wave normal stress $\overline{\tilde{w}\tilde{w}}$, which at the first order results

$$\overline{\tilde{w}\tilde{w}} = gka_i^2 \frac{\sinh\left[k\left(z+h\right)\right]}{\sinh\left(2kh\right)}\left[1+K_r^2+2K_r\cos(2kx+\Delta\varphi)\right]. \tag{4.5}$$

Figures 4.15 and 4.16 show the wave normal stresses of the wave-induced Reynolds stress tensor for experiments PoW1–5 (different partial reflection conditions, same LDV position) and $2a$–$d$ (same partial reflection conditions, different LDV positions), respectively. Both the Reynolds wave normal stresses $\overline{\tilde{u}\tilde{u}}$ and $\overline{\tilde{w}\tilde{w}}$, show good agreement with the theoretical model within the statistical and experimental uncertainties. The results show also that reflection induces a spatial variation of the normal stresses (they are both modulated along $x$) and exerts a stronger modulation on the horizontal component $\overline{\tilde{u}\tilde{u}}$ than on the vertical normal stress $\overline{\tilde{w}\tilde{w}}$.

Figure 4.17 reports the Reynolds turbulent shear stress $\overline{\widetilde{u'w'}}$ for experiments PoW1–5 (different reflective conditions and same LDV measurement section). Results show that opposing wind causes a negative turbulent shear stress near the surface, which suggest a momentum transfer downwards (from air to water). Furthermore, the turbulent shear stress goes to zero at $\approx 0.5\, z/h$, i.e. half the water column. For decreasing reflection (from PoW1 to 5), the turbulent shear stress is larger and reach lower water levels.

Since the forcing of the process at the surface is the wind action, we are not surprised that also for paddle waves with opposing wind the Reynolds turbulent shear stress yields a momentum transfer from the wind to the wave.

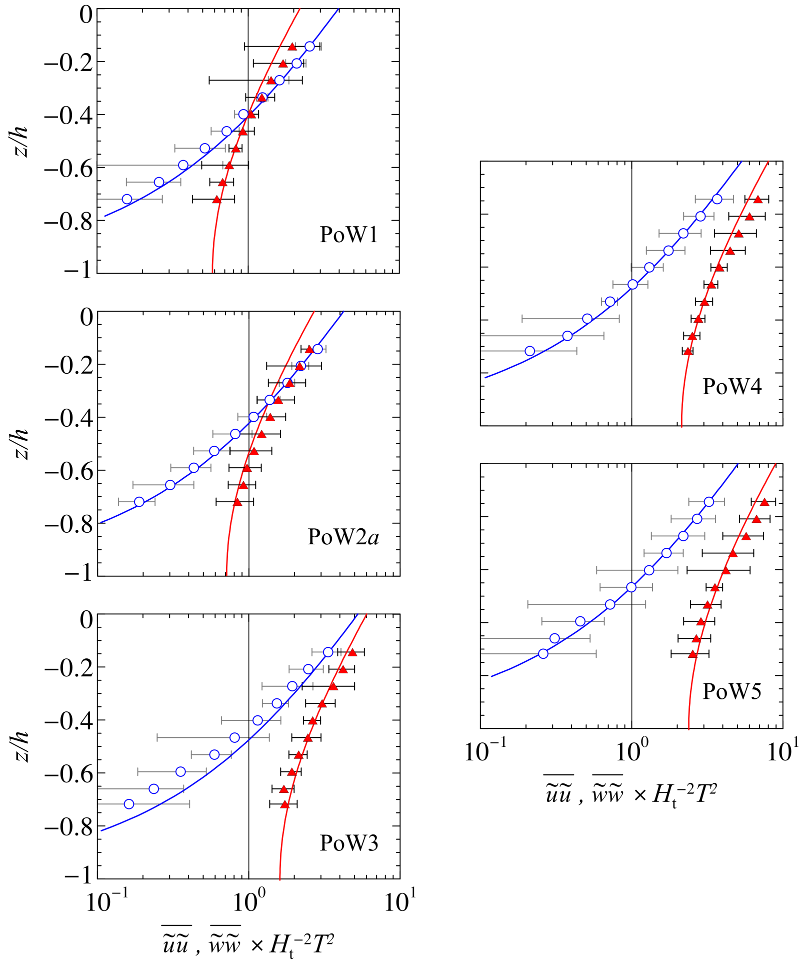

Figure 4.15: Experiments PoW1–5 (different reflective conditions, same LDV section): vertical profile of the Reynolds wave normal stresses. Symbols are experimental the horizontal $\overline{\tilde{u}\tilde{u}}$ (blue stars) and vertical $\overline{\tilde{u}\tilde{u}}$ (red triangles) components, solid lines are theoretical values. Error bars are two standard deviations.

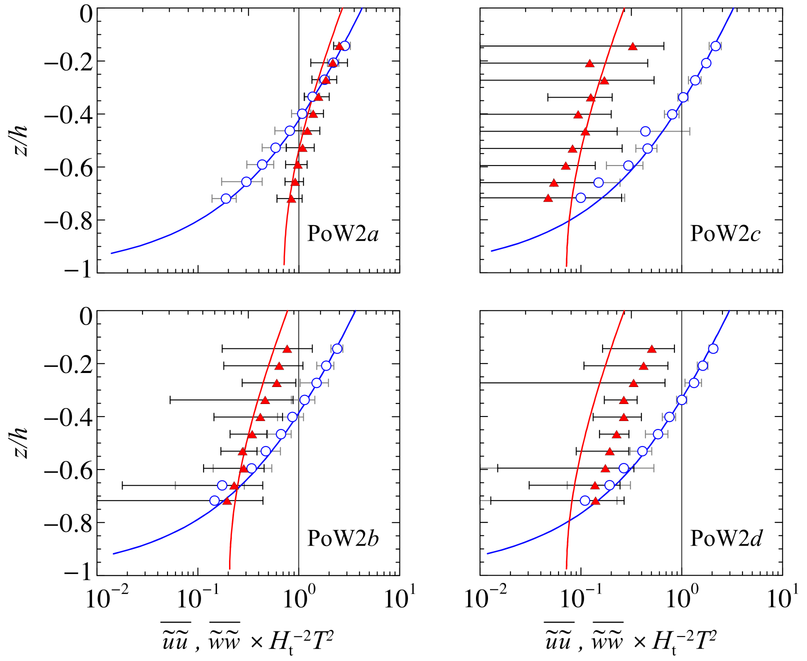

Figure 4.16: Experiments PoW2$a$–$d$ (same reflection, different LDV sections): vertical profile of the Reynolds wave normal stresses. Symbols are experimental the horizontal $\overline{\widetilde{u}\widetilde{u}}$ (blue stars) and vertical $\overline{\widetilde{u}\widetilde{u}}$ (red triangles) components, solid lines are theoretical values. Error bars are two standard deviations.

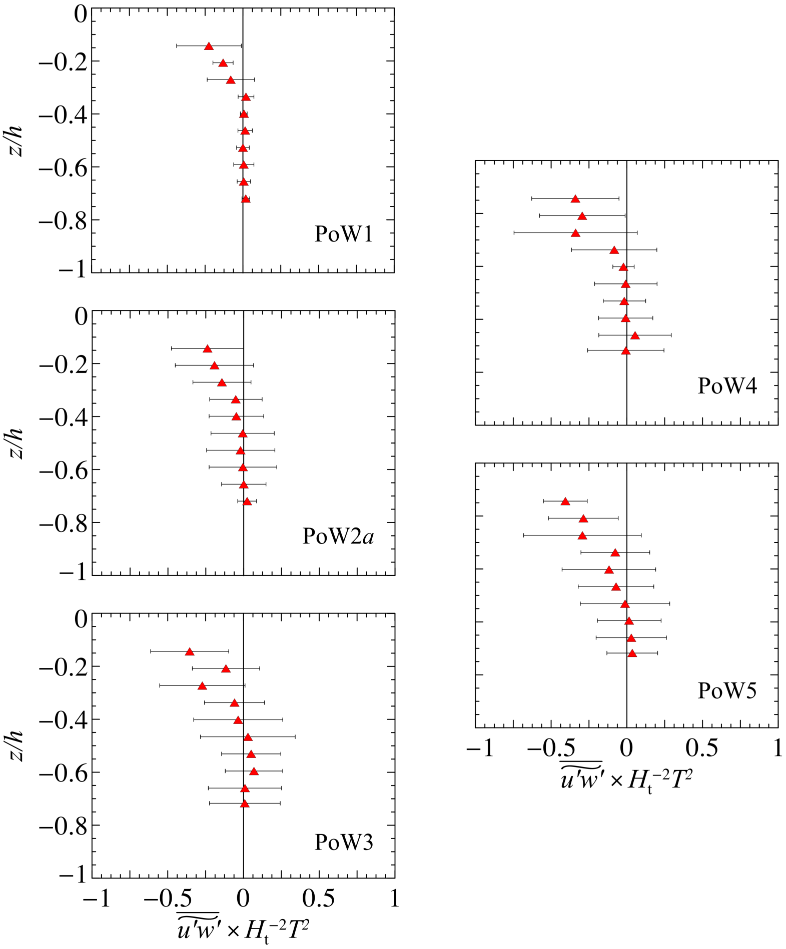

Figure 4.17: Experiments PoW1–5, paddle waves with opposing wind (different reflective conditions, same LDV position): turbulent Reynolds shear stress $\widetilde{u'w'}$ along the vertical. Symbols are experimental data, error bars are two standard deviations.

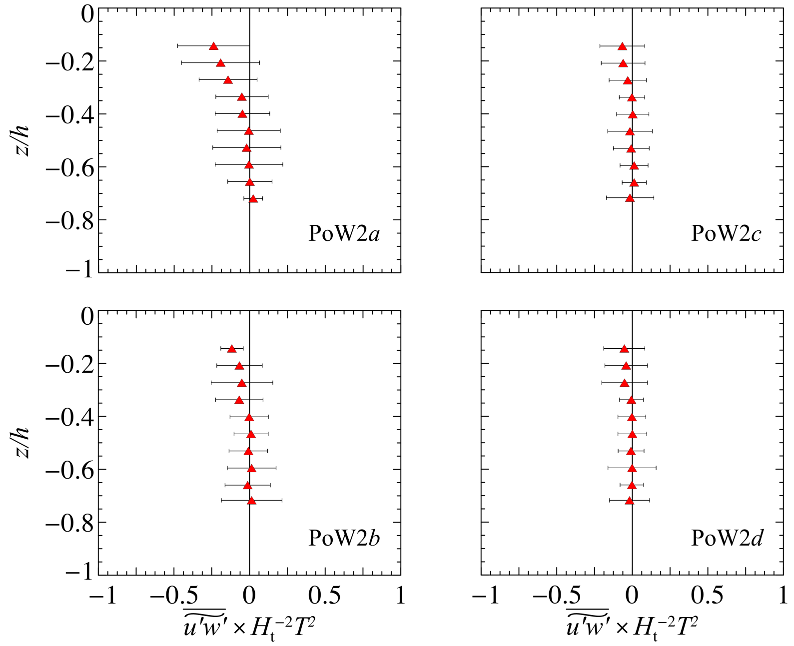

Figure 4.18: Experiments PoW2$a$–$d$, paddle waves with opposing wind (same reflection, different LDV sections): turbulent Reynolds shear stress $\widetilde{u'w'}$ along the vertical. Symbols are experimental data, error bars are two standard deviations.

Figure 4.18 shows the Reynolds turbulent shear stress in the vertical for experiments PoW2$a$–$d$ (same reflective conditions, different LDV section). The vertical profile of $\overline{u'w'}$ differs for each test and suggests some dependence on the LDV measurement section, even though the trend is not clear. Also in these experiments, observations indicate a net momentum transfer from wind to the water field.

Figures 4.19 and 4.20 show the diagonal terms of the turbulent Reynolds stresses tensor for tests PoW1–5 and PoW2$a$–$d$, respectively. Their values increase approaching the air/water boundary layer; it means that much of the kinetic energy is concentrated at the interface between air and water.

In particular, it is observed that the horizontal normal stress $\widetilde{\overline{u'u'}}$ is always larger than the vertical $\widetilde{\overline{w'w'}}$, suggesting a dominant component in the wind direction. At lower levels, the normal stresses decrease and become uniform in the vertical, indicating a rotation of the Reynolds turbulent stress tensor. For increasing reflection, normal stresses show a reduction of their values in the measured water column and have less variability (deviations are smaller). Experiments PoW2$a$–$d$ show similar vertical profiles at different LDV sections and also a slight spatial variation of the normal stresses appears, more evident near the surface.

In general, observations of the non-dimensional Reynolds turbulent stress tensor components indicate that reflection acts as a constraint on the turbulent flow field induced by an opposing wind; for lower reflection, the turbulent stresses are larger with higher deviations and diffuse at lower water levels, while for higher reflection the turbulent stresses have less intensity and smaller variability. The vertical profile of the turbulent stresses, and in particular the shear component, shows a transfer of momentum from the air flow to the water column which deserves further investigations through a quadrant analysis.

### 4.2.4 Quadrant Analysis

A quadrant analysis, which is described in 2.2.3 and performed in 3.2.7, is conducted for experiments of paddle waves with opposing wind. This type of analysis identifies the dominant contributions of the Reynolds turbulent shear stress to the turbulent momentum exchange by considering the signs of $u'$ and $w'$. We call “sweeps” and “ejections” the events attributed to the first quadrant ($u'$ and $w'$ both positive) and the third quadrant ($u'$ and $w'$ both negative), respectively. Events related to the second and fourth quadrants are called outward and inward interaction, respectively.

Figure 4.21 shows the vertical profiles of the event-averaged and total shear stress for PoW1–5 (different reflection, same LDV position). Results show that the main elements contributing to the total shear stress are $S_2$ and $S_4$, which represent the turbulent shear stresses of the second and fourth quadrant. In particular, the outward interaction is the dominant

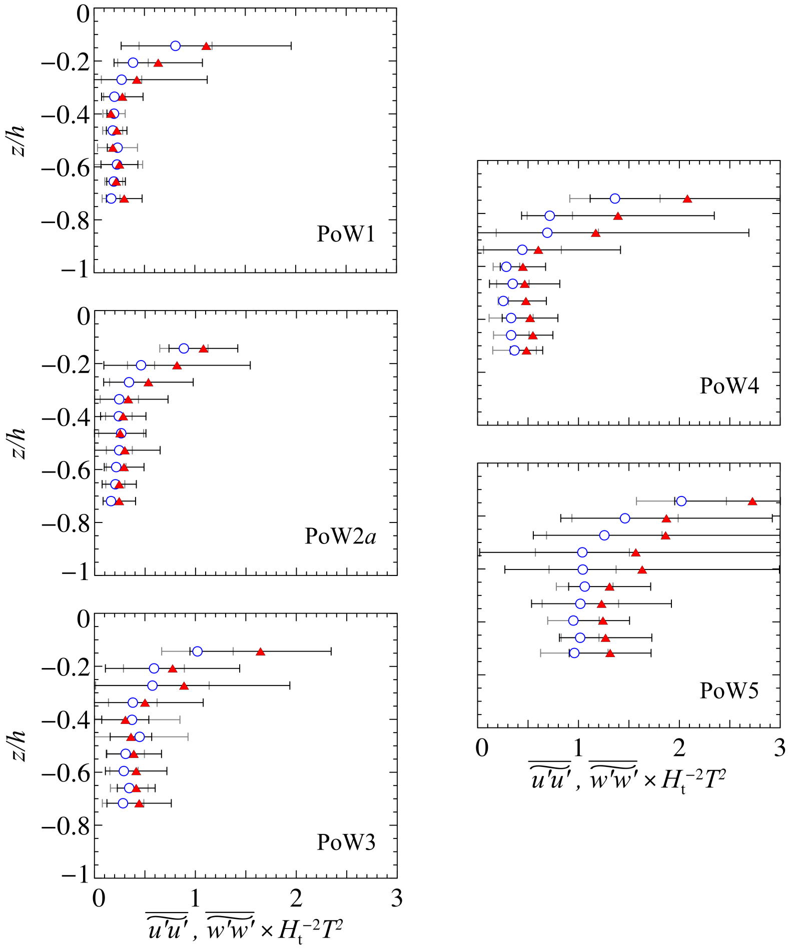

Figure 4.19: Experiments PoW1–5, paddle waves with opposing wind (different reflective conditions, same LDV section): vertical profile of the experimental turbulent Reynolds normal stresses $\widetilde{\overline{u'u'}}$ (blue stars) and $\widetilde{\overline{w'w'}}$. Error bars are two standard deviations.

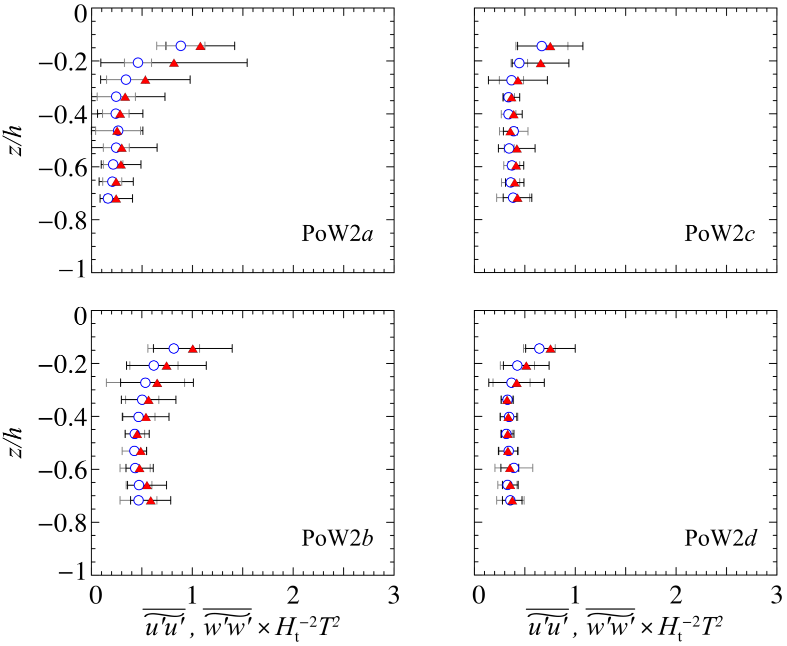

Figure 4.20: Experiments PoW2$a$–$d$, paddle waves with opposing wind (same reflection, different LDV sections): vertical profile of the experimental turbulent Reynolds normal stresses $\overline{\widetilde{u'u'}}$ (blue stars) and $\overline{\widetilde{w'w'}}$. Error bars are two standard deviations.

component and indicates that momentum is transferred from the upper side of the interface towards lower water levels. We observe also that the intensity of the events of every quadrant increases for decreasing reflection, and that stronger events take place near the surface (that is where wind action is more effective). At lower levels, the turbulent shear stress contributions from each quadrant has minor intensity; in addition, they are uniform in the vertical and each quadrant gives an equal contribution to the total shear stress.

Figure 4.22 reports the vertical profiles of the event-averaged and total shear stress for experiments $2a$–$d$ (same reflective conditions, different LDV sections). Results suggest that the event-averaged shear stresses depend on the section of velocity measurements, hence a reflection induces also a spatial variation of the turbulent shear stress contributors. The dominant components are again the outward and inward interaction, and the vertical profiles behaves coherently with the observations of PoW1–5.

Conditional averages are related to the joint probability density function of the fluctuating velocities. Figures 4.23 reports the joint p.d.f. at the maximum level of measurement in water below the free surface, for experiments PoW1–5 (different reflection, same LDV section). Contours of the surface has a constant interval of each 10% and are elliptic (or almost elliptic) in all the cases. The major axis of the ellipses tends to be directed as the bisector of the second and the third quadrants, while turbulent velocities fluctuations show tendency to inhibit each other in the third and the first quadrants. It confirms the main contributions of outward and inward interactions. However, different reflective conditions modify the shape and also the orientation of the ellipses, even though the trend is not clear.

Figure 4.24 shows the joint p.d.f. at the higher level of measurement in water below the free surface, for tests PoW$2a$–$d$ (same reflection, different LDV positions). In this case, neither the form nor the inclination of the

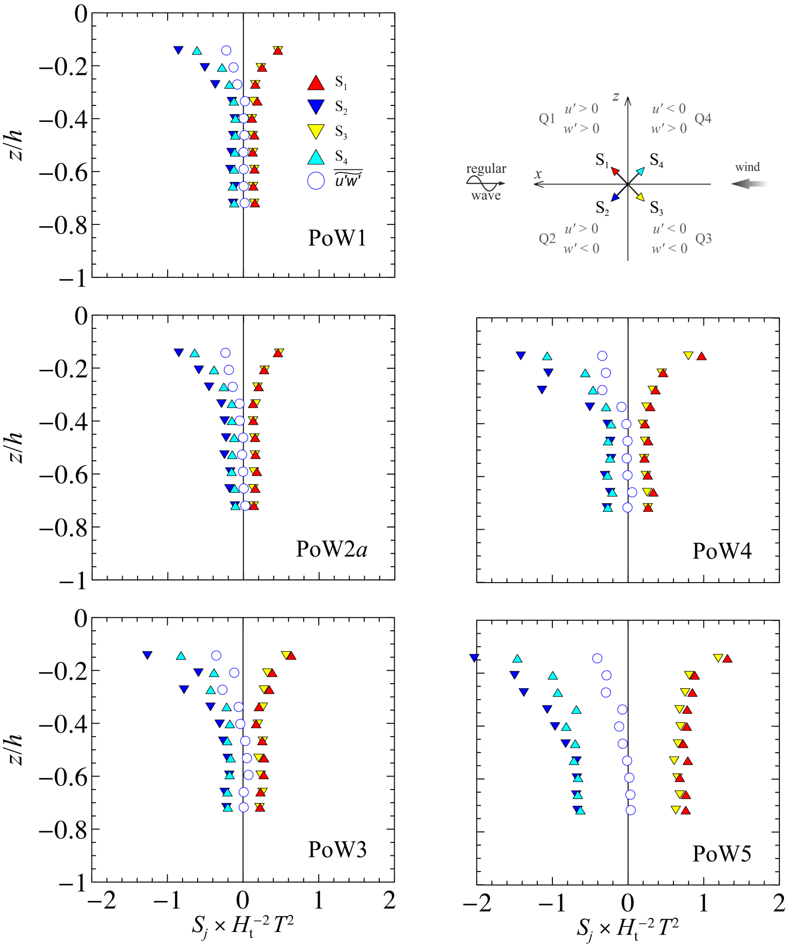

Figure 4.21: Experiments PoW1–5, paddle waves with opposing wind (different reflective conditions, same LDV section). The event-averaged shear stress $S_j$ for the $j$th quadrant (triangles) and the total shear stress (circles).

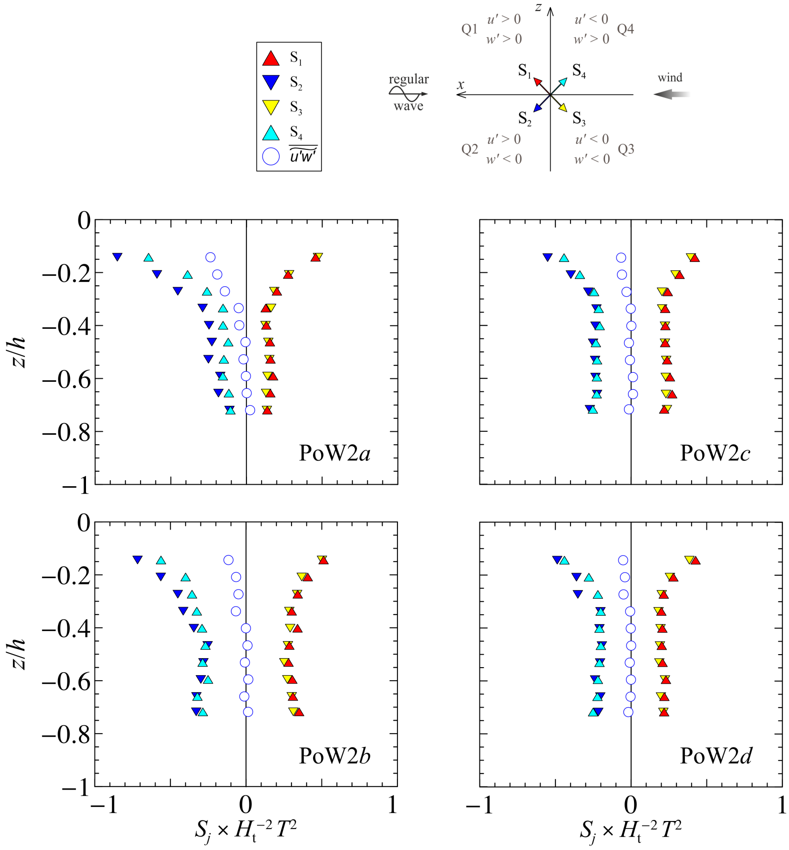

Figure 4.22: Experiments PoW2$a$–$d$, paddle waves with opposing wind (same reflection, same LDV sections). The event-averaged shear stress $S_j$ for the $j$th quadrant (triangles) and the total shear stress (circles).

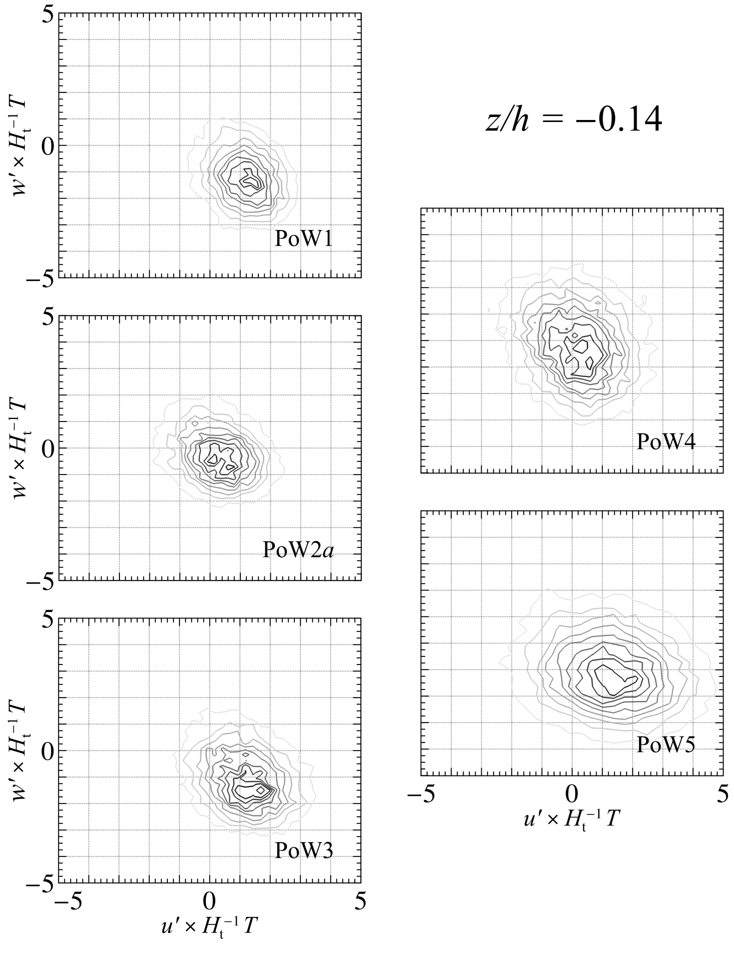

Figure 4.23: Experiments PoW1–5, paddle waves with opposing wind (different reflective conditions, same LDV section). Contours of the joint probability density functions for the non-dimensional fluctuating velocities $u'$ and $w'$, at the maximum measurement level ($z/h = 0.14$). The inner curve is equal to 90%, with a constant probability interval of each 10%.

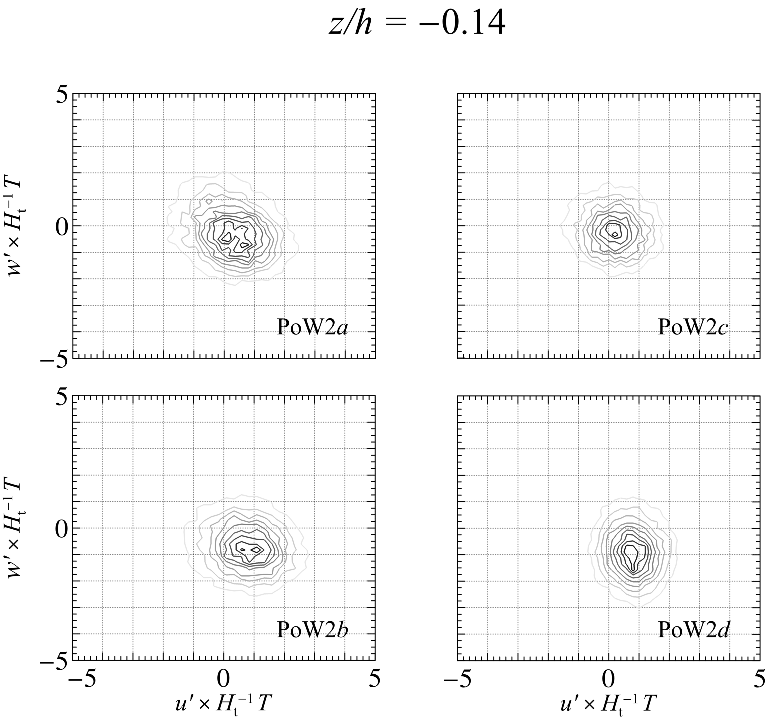

Figure 4.24: Experiments PoW2$a$–$d$, paddle waves with opposing wind (same reflection, same LDV sections). Contours of the joint probability density functions for the non-dimensional fluctuating velocities $u'$ and $w'$, at the maximum measurement level ($z/h = 0.14$). The inner curve is equal to 90%, with a constant probability interval of each 10%.

contours are well defined. Since this phenomenon happens with constant reflective conditions, we attribute this distortion to the spatial variation induced by reflection.

The time-averaged Reynolds shear stress from each quadrant are also calculated as function of the parameter $M$, which determines the threshold above which events are considered. Figure 4.25 shows the results for experiment PoW5, with different levels of concentration $C_M^j$ superimposed

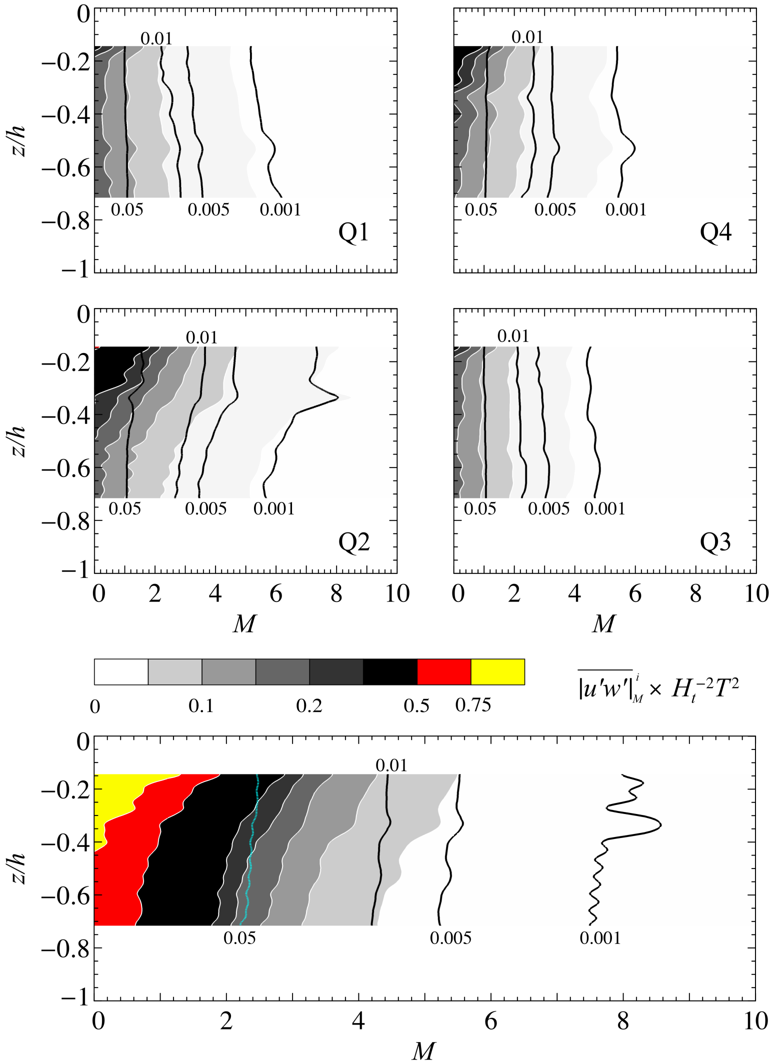

Figure 4.25: Experiment PoW5. Time-averaged Reynolds shear stress in each quadrant decomposed (upper panels) and without decomposition (lower panel), as a function of the threshold parameter M. The isolines of the duration fraction (concentration) are superimposed.

to the time-averaged shear stress, decomposed in quadrants and without decomposition (total). The results suggest again that the main contribution to the total shear stress derives from quadrants $Q_2$ and $Q_4$, with a major momentum transfer from the air to the water side, which is the same results found for following winds. The highest values of the time-averaged shear stress still take place in proximity of the free surface, but we notice that for experiment PoW5 (opposing wind, minimum reflection), the turbulent shear stresses are relevant also far from the interface, meaning that they can induce turbulent momentum flux into deep waters.

### 4.2.5 Reynolds stress tensor principal axes

We have already defined both the Reynolds wave stress tensor, which represents the periodic stresses, and the Reynolds turbulent stress tensor, which represents the fluctuating stresses. They are both second-order and symmetric and can be diagonalized in order to obtain the principal stresses $\sigma_{\max}$ and $\sigma_{\min}$ (the diagonal term of the diagonalized tensor) and the principal angle $\alpha_{\mathrm{p}}$, which represents the inclination of the principal stresses with respect to the coordinates $x$-$z$ (see §1.3). We notice that the real flow field is three-dimensional, hence we have a reduced perspective of the real structure

For the Reynolds wave stress tensor, the analytical model allows a theoretical representation of the principal stresses and the principal angle in the vertical, thus theoretical profiles can be compared to the experimental values. For the Reynolds turbulent stress tensor, only the experimental values are available.

Figure 4.26 shows the ratio of the maximum to the minimum principal stress for tests PoW1–5 (different reflective conditions, same LDV position), which offers a synthetic view of the isotropy of the second-order tensor. The wave principal stresses values $\widetilde{\sigma}_{\max}$ and $\widetilde{\sigma}_{\min}$ are well approximated by theory; the vertical trend is similar for different reflective conditions, but it is evident that higher reflection causes a shift towards larger values of the ratio $\widetilde{\sigma}_{\max}/\widetilde{\sigma}_{\min}$ (i.e. a stronger anisotropy). Turbulent principal stresses ratio shows a vertical profile which is almost uniform and in the range

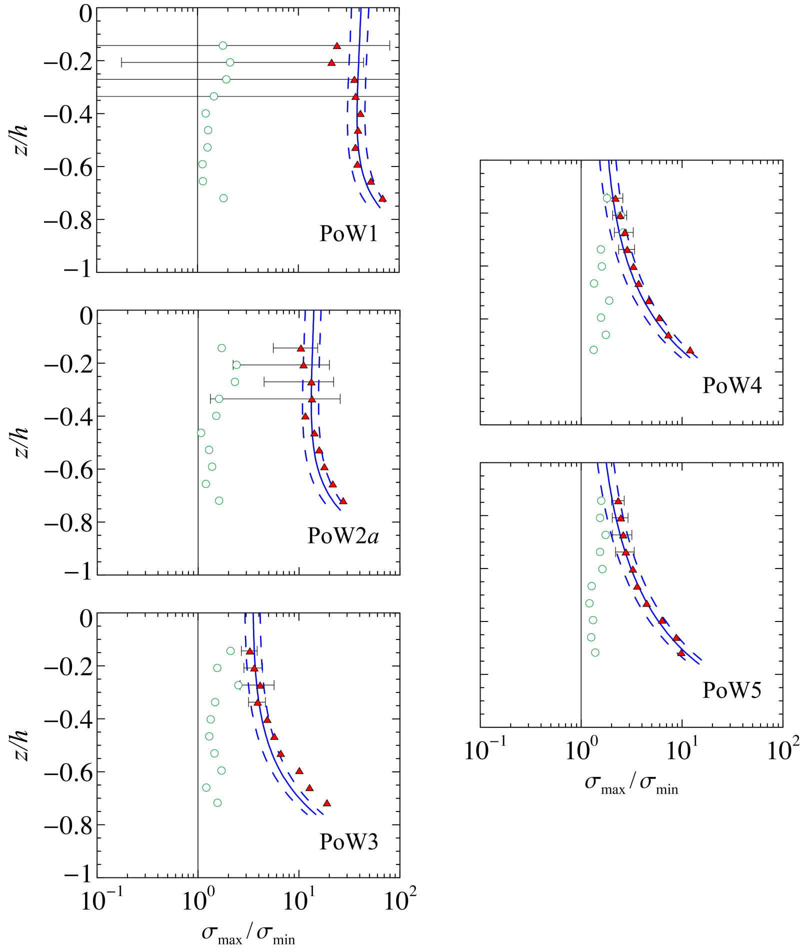

Figure 4.26: Experiments PoW1–5, paddle waves with opposing wind (different reflective conditions, same LDV section). Ratio of the maximum to minimum principal stress $\sigma_{\max}/\sigma_{\min}$. Triangles and circles are experimental values for periodic and fluctuating components, respectively, with error bars equal to one standard deviations. Solid lines are theoretical values from equation (1.27), while dashed lines are confidence intervals to 95%.

$1-3$; in particular, the general trend suggests that the ratio $\sigma'_{\max}/\sigma'_{\min}$ increases from the bottom to the free surface where a slight anisotropy is more evident. For decreasing reflection (from PoW1 to PoW5), the wave principal stress ratio tend to collapse on the turbulent component.

Figure 4.27 shows the ratio of the maximum to the minimum principal stress for tests PoW2*a–d* (same reflective conditions, different LDV sections). In this case, the vertical profiles of both the wave $\widetilde{\sigma}_{\max}/\widetilde{\sigma}_{\min}$ and the turbulent $\sigma'_{\max}/\sigma'_{\min}$ shows a dependence on the LDV measurement section of the maximum to minimum stress ratio.

Figure 4.28 shows the principal angles of the Reynolds wave and turbulent stress tensors for tests PoW1–5 (different reflective conditions, same LDV section). The vertical profile is modulated for different reflective conditions, coherently with the theoretical model: we notice also that the principal angle decreases for decreasing reflection (from PoW1 to 5).

Figure 4.29 shows the principal angles of the Reynolds wave and turbulent stress tensors for tests PoW2*a–d* (same reflective conditions, different LDV sections), indicating the different profiles and values assumed by the principal angle by changing the LDV measurements section. The results highlight that the partially reflective conditions are not the only effect to be taken into account, and that also the spatial variation has a relevant influence in wave field with partial reflection.

The principal angles of all experiments of the Reynolds turbulent tensor are shown in figure 4.30. The trend of experimental values suggests an increasing $\alpha'_p$ from the bottom to the top, tending to $\pi/4$ near the free surface. The results shows that uniform shear rate current near the free surface is dominant also for opposing wind; the same result was observed in paddle waves plus following wind, where the experimental points of the turbulent principal angle in the vertical show a similar trend.

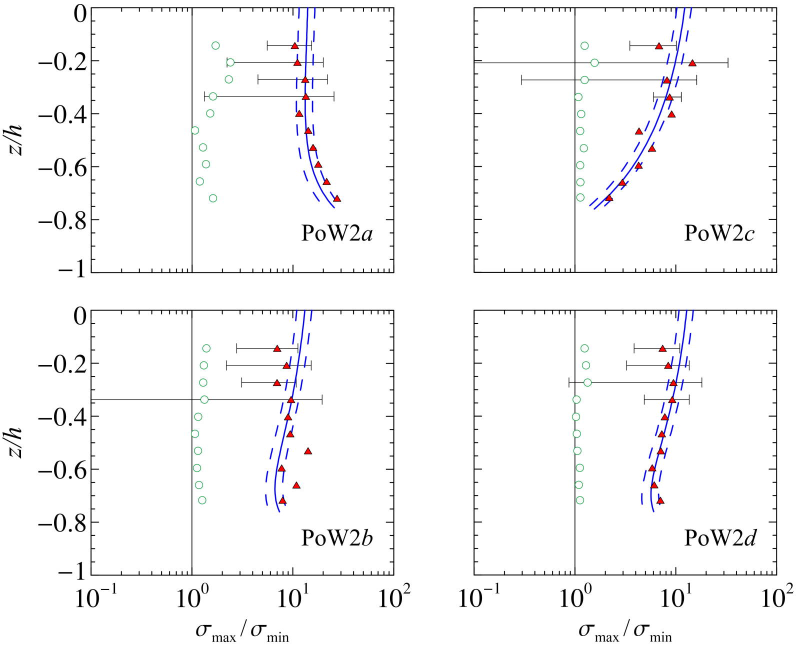

Figure 4.27: Experiments PoW2*a*–*d*, paddle waves with opposing wind (same reflective conditions, different LDV sections). Ratio of the maximum to minimum principal stress $\sigma_{\max}/\sigma_{\min}$. Triangles and circles are experimental values for periodic and fluctuating components, respectively, with error bars equal to one standard deviations. Solid lines are theoretical values from equation (1.27), while dashed lines are confidence intervals to 95%.

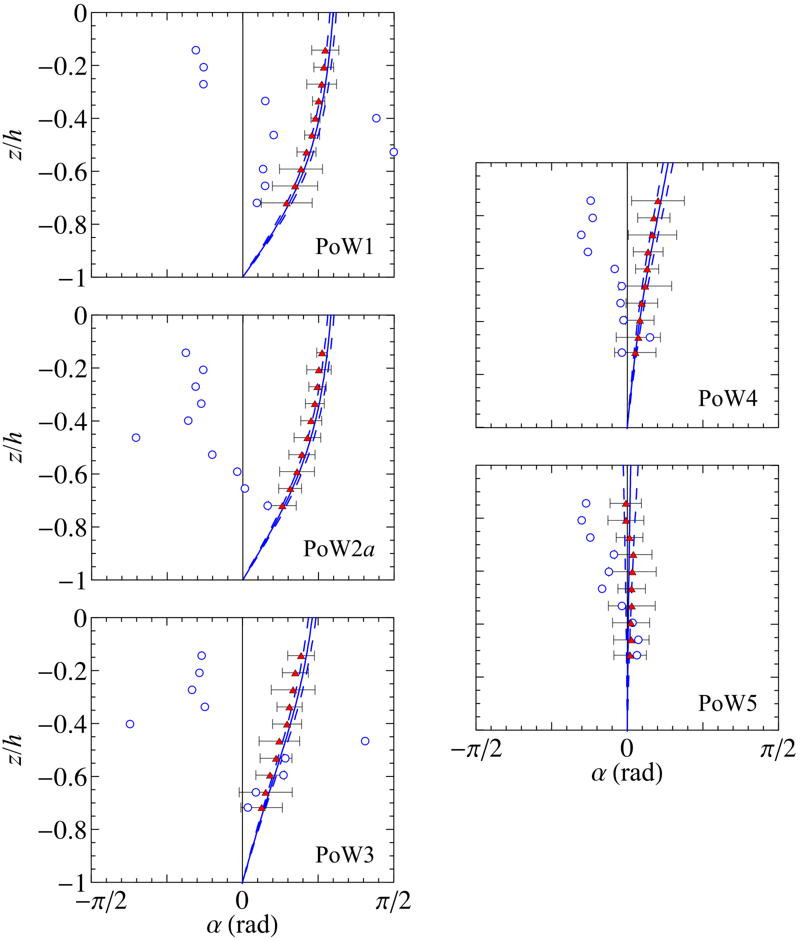

Figure 4.28: Experiments PoW1–5, paddle waves with opposing wind (different reflection, same LDV section). Wave and turbulent principal angles $\widetilde{\alpha}_p$ and $\alpha'_{exp}$, respectively. Triangles and circles are periodic and fluctuating experiments, respectively, while solid lines are theoretical values. Error bars are two standard deviations, dashed lines are confidence intervals to 95% level.

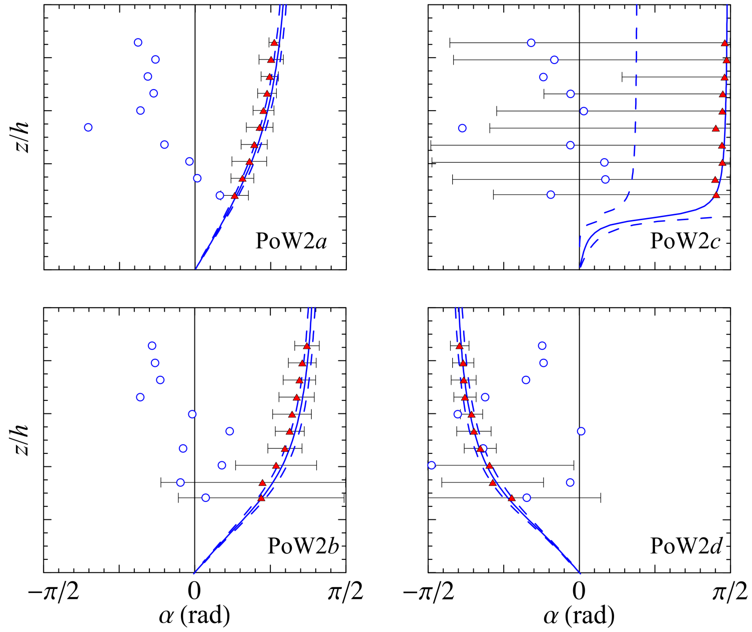

Figure 4.29: Experiments P2$a$–$d$, paddle waves with opposing wind (same reflection, different LDV positions). Wave and turbulent principal angles $\widetilde{\alpha}_p$ and $\alpha'_{exp}$, respectively. Triangles and circles are periodic and fluctuating experiments, respectively, while solid lines are theoretical values. Error bars are two standard deviations, dashed lines are confidence intervals to 95% level.

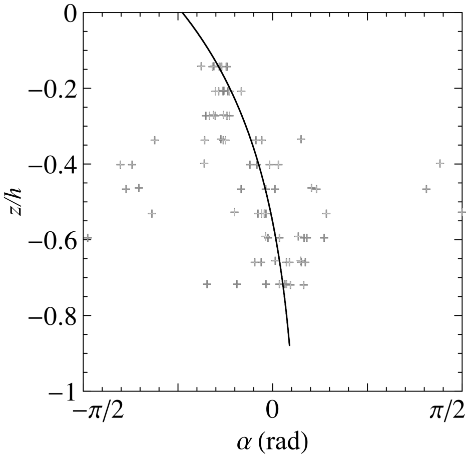

Figure 4.30: Experiments PoW, paddle waves with opposing wind. Symbols are the experimental turbulent principal angles $\alpha'_{exp}$. Solid lines is an empirical fitting of the experimental data.

## 4.3 Discussion of the results

We report experiments of paddle waves with opposing wind (PoW) under partial reflection conditions.

The results confirm that the theoretical model developed in Chapter§1 is valid also with opposing wind for the Reynolds wave stress tensor, as well as for the periodic component of the free surface data (mean water level and total wave height).

The direct comparison of the opposing wind effects on the wave field, in particular on the reflective conditions, is observed. The overall effects on the free surface is that wind induces an attenuation of the wave height, a reduction of the reflection coefficient and a negative phase shift to the reflected component. Furthermore, the wave profiles clearly indicate that, for increasing reflective conditions, wind induces a significant distortion of the shape of the wave.

In the analysed fetch domain, the general behaviour of the wind wave height is an initial growth attributed to the wind energy input, as expected, followed by an attenuation due possibly to micro-breaking. On the other hand, wind wave peak period grows monotonically for increasing fetch length, coherently with the current knowledge of the wind-wave growth. The separation of the wind waves components gives the tool to analyse how wind waves propagate along the channel, through the measures of the phase and group velocities. Experimental observations are well interpreted by a dispersion relation which includes the effects of sheared horizontal currents beneath the free surface (Swan & James, 2000), while the linear dispersion relation $\omega^2 = gk \tanh kh$ always underestimates the experimental data.

The components of the Reynolds stress tensors (both wave and turbulent) are experimentally analysed. Wave normal and shear stresses, as well as the principal stresses and the principal angle, show good agreement with the theoretical predictions. The Reynolds wave shear stress $-\overline{\tilde{u}\tilde{w}}$ changes sign and intensity again as found in Chapter §3, is always well-predicted by the theory and confirms the importance of including partial reflection analysis in modelling the wave field. The comparison between paddle waves (no wind) and paddle waves with opposing wind indicates a reflection attenuation and a phase lag in the second case (when both experiments have similar experimental parameters). The Reynolds wave normal stresses are well predicted by theory; furthermore, it is observed that $\overline{\tilde{u}\tilde{u}}$ is much more influenced by the reflection parameters than the vertical component $\overline{\tilde{w}\tilde{w}}$, which is almost independent on the reflective conditions.

The experimental Reynolds turbulent stresses are also reported. Some insights on the turbulent flow of the wind waves are investigated through the quadrant analysis and the joint probability density functions of the non-dimensional horizontal and vertical fluctuating velocities. The outward-inward interactions are dominant in the physical process, and a net transfer of momentum from air to water is observed, as expected.

We notice that turbulent fluctuations are non-dimensional with respect to $H_t/T$, which is a velocity scale which depends on reflective conditions. In particular, the square of the velocity scale can be interpreted as the kinetic energy of the wave component, thus the non dimensional turbulent normal stresses represent the rate of the turbulent kinetic energy with respect to the wave component. Observations indicate that these rates decrease for increasing reflection, indicating that turbulent kinetic energy is less relevant for higher reflective conditions. In addition, the absolute values of the turbulent stresses also increase for decreasing reflection, which means that turbulent momentum transfer under opposing wind action is more effective for lower reflective conditions.

The Reynolds wave and turbulent stress tensors are also analysed in terms of principal stresses and angle of the principal axes. The vertical profile of the wave principal stresses ratio is well interpreted by the theoretical model, showing larger anisotropy of the tensor for increasing reflection. The turbulent principal stresses tends to 1 at lower water levels, and increases toward the bottom. For lower reflection intensity, the principal stresses ratio of the wave and turbulent Reynolds tensors tend to the same value near the surface. A spatial variation of the principal stresses ratio is also observed for same reflective conditions for both wave and turbulent components, even though it is more evident for the wave Reynolds tensor. The principal angles show the different behavior of the Reynolds wave principal axes for varying reflective conditions and LDV measurement sections, and is always well represented by the theoretical profile. The turbulent principal angles show a slight dependence on different reflective conditions (larger fluctuations for increasing reflection) and on LDV measurement sections, but the general behaviour suggests that in all cases near the surface a uniform shear rate current is dominant, rotating the reference system. The same result was also observed for following wind conditions.

# Chapter 5

# General overview of the results

Chapters §3 and §4 report the analyses and the results of the two sets of experiments realized. Since the two previous chapters are wide with extensive descriptions, the reader could get lost within the huge amount of images and discussions without finding the connections among the different parts of the thesis. This chapter aims to give a unified vision of the analyses conducted (in particular, for experiments in the presence of wind), starting from velocity measurements, comparing the different experimental conditions in order to facilitate the comprehension of the study and yielding to further remarks. In particular, the results are shown in a compact form for paddle waves plus following wind (PpW), for paddle waves with opposing wind (PoW) and by comparing three experiments with similar reflection and different wind conditions (P1 for no wind, PpW4 for following wind and PoW4 for opposing wind). Here only experimental values are shown, since the agreement between the theoretical model and the experiments has already been discussed in the previous chapters.

## 5.1 Mean velocity

The mean velocities represent currents which develop inside the wave flume. The main interest is generally focused on the horizontal mean current, which in the present experiments is strongly influenced by the wind action. The mean horizontal and vertical velocities arise also from other sources, as non-linear effects of the regular wave between troughs and crests, the finite length of the wave flume, secondary circulations which take place in the presence of wind and partial reflection.

Figure 5.1a) shows the horizontal and vertical mean velocities for experiments PpW1–4. The results illustrate the profiles for different following wind speeds and similar reflection conditions. A typical profile for a wind-induced horizontal current $\overline{u}$, which has already been explained in chapter §3, is observed: positive near the surface (i.e., in the same direction of the wind) and negative at lower levels, in order to fill the mass conservation for a finite-length domain. Furthermore, non-dimensional values indicate that for increasing wind speed, the modulus of both positive and negative horizontal mean velocities is enhanced. On the other hand, the vertical velocity $\overline{w}$ is negative at lower levels and tends to positive values near the surface, but it is not clear the influence of different winds on the vertical profile.

Figure 5.1b) reports the horizontal and vertical mean velocities for experiments PoW1–5, which investigate different reflective conditions with same opposing wind speeds. The same considerations of experiments PpW1–4 can be done for the wind-induced horizontal currents; moreover, we observe that, for increasing reflection, the non-dimensional horizontal mean velocity decreases. The pattern of the vertical mean velocity does not show a clear trend for varying reflection and is similar to experiments PpW1–4.

Figure 5.1c) shows the horizontal and vertical mean velocities for experiments PoW2$a$–$d$, which have with similar reflective conditions, same opposing wind and different LDV measurements section. The wind-induced horizontal and vertical mean velocities have similar trend if compared with experiments PoW1–5 and PpW1–4: an influence of different LDV sections is present, but we are not able to extract a significant trend.

Figure 5.1d) shows the comparison among experiments with similar reflection and different wind conditions (PoW4 for opposing wind, PpW1 for following wind and P1 for the absence of wind). The results suggest that, for both the horizontal and vertical mean velocities, increasing wind speed yields a larger modulus (both in a negative and positive sense) of the mean values.

## 5.2 Wave normal and shear stresses

The wave stresses are intended as those stresses induced by the paddle waves and separated from the mean and turbulent components by means of a phase average technique. In this thesis, the wave stresses are also studied through a theoretical model which takes into accounts the effects of different reflective conditions; the goodness of the theoretical approach has been shown in the previous chapter, thus theoretical profiles are not reported in this chapter.

Figure 5.2a) shows the wave shear stress (covariance) $\overline{\widetilde{u}\widetilde{w}}$ for experiments PpW1–4, i.e. paddle waves with different following winds, similar reflective conditions and active absorption. Since the reflective conditions and the LDV section are the same, we do not observe significant change in the experimental values of $\overline{\widetilde{u}\widetilde{w}}$. We have already described the dependence of the wave shear stress (and its variability) in chapter §3, where also the goodness of the theoretical model is illustrated.

The explanation given for the wave shear stress profile of experiments PpW1–4 is confirmed in figure 5.2b) and figure 5.2c), which report the wave shear stress for experiments PoW1–5 and PoW2*a*–*d*, respectively. In the first case, figure 5.2b), different reflective conditions with same opposing wind and LDV section are illustrated, while in the second case same opposing wind, similar reflective conditions and different LDV sections are shown. The results clearly indicate and support the analytical formulation of chapter §1, where the equation (1.13) shows that sign and modulus of $\overline{\widetilde{u}\widetilde{w}}$ depend on the reflective parameters and the section of measurements.

Figure 5.2d) reports the comparison of $\overline{\widetilde{u}\widetilde{w}}$ among experiments with

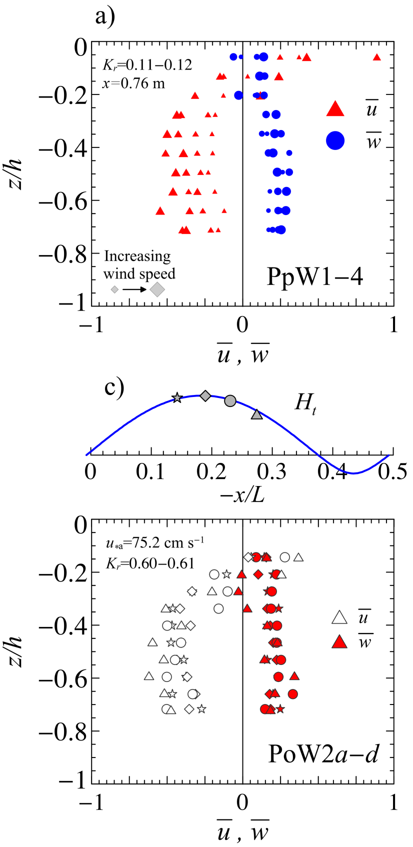

Figure 5.1: Comparison of the non-dimensional mean velocities for different experimental conditions. a) Horizontal (red triangles) and vertical (blue circles) mean velocities for experiments PpW1–4, paddle waves plus following wind (same reflection, same LDV section, different wind). Symbol size is proportional to the wind speed. b) Horizontal (red triangles) and vertical (blue circles) mean velocities for experiments PoW1–5, paddle waves with opposing wind (different reflection, same LDV section, same wind). Symbol transparency is proportional to the paddle wave reflection. c) Horizontal (empty symbols) and vertical (blue symbols) mean velocities for experiments PoW2$a$–$d$ (same reflection, different LDV section, same wind). d) Comparison among experiments with similar reflection and different wind conditions: P1 (grey small symbol with dotted line) for no wind, PpW4 (empty small symbol with solid line) for following wind, PoW4 (big blue symbol) for opposing wind. All values are non-dimensional with respect to $H_tT^{-1}$.

similar reflection and different wind conditions (PoW4 for opposing wind, PpW1 for following wind and P1 for the absence of wind). The vertical profiles are different due to the specific reflective parameters of the single experiments: in particular, for similar reflection coefficient $K_r$, the phase shift $\Delta\varphi$ is the main responsible of the difference and is due to the different wind conditions.

Figure 5.3a) shows the wave normal stresses $\overline{\tilde{u}\tilde{u}}$ and $\overline{\tilde{w}\tilde{w}}$ for experiments PpW1–4. The same considerations reported for the wave shear stress still hold for normal stresses, since we do not observe significant variations of the wave normal stresses among the different experiments (as expected since we do not vary reflection conditions or LDV section). The main differences can be individuated near the interface between air and water, where the action of the wind becomes relevant and influences the wave stresses (both normal and shear) proportionally to the wind speed.

Figure 5.3b) and figure 5.37c) report the wave normal stresses for experiments PoW1–5 and PoW2*a*–*d*, respectively. It is still evident the dependence of the wave normal stresses on the reflective conditions (figure 5.3b) and on the LDV section (figure 5.3c); furthermore, the main variations take place for the horizontal component $\overline{\tilde{u}\tilde{u}}$, whose values differ also for one order of magnitude in the entire vertical profile, while the vertical component $\overline{\tilde{w}\tilde{w}}$ shows a major difference only near the surface.

Figure 5.3d) shows the comparison of $\overline{\tilde{u}\tilde{u}}$ and $\overline{\tilde{w}\tilde{w}}$ among experiments with similar reflection and different wind conditions (PoW4 for opposing wind, PpW1 for following wind and P1 for the absence of wind). We still attribute the main differences to the phase shift $\Delta\varphi$, which varies for different wind conditions (speed and direction), and also to the effects of the turbulent structure due to the wind, which induces variations of the experimental wave stresses not predictable by the theoretical model.

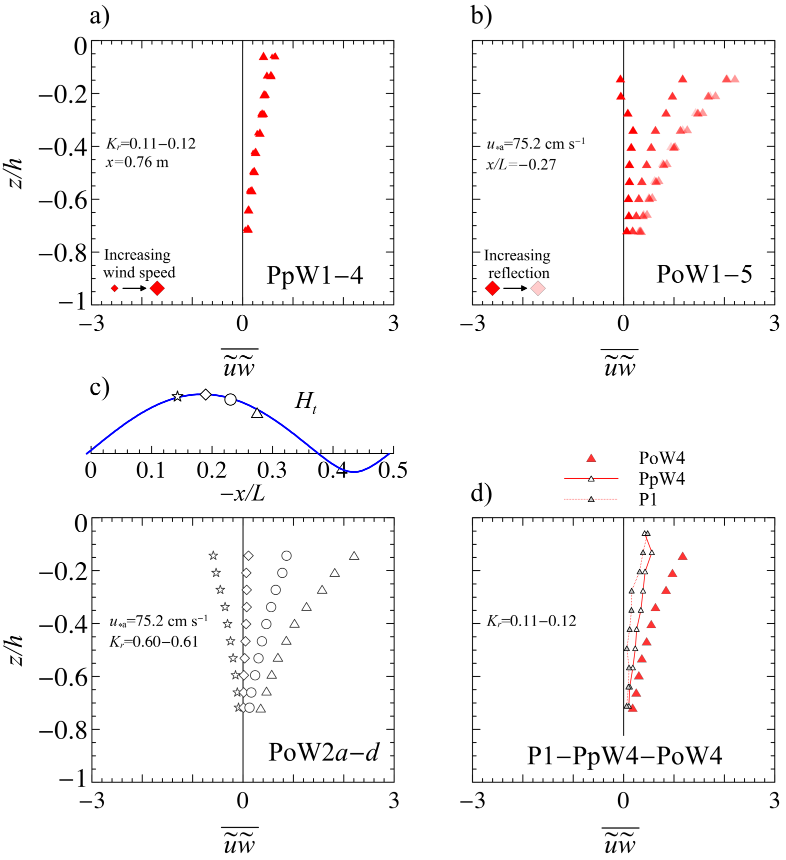

Figure 5.2: Comparison of the non-dimensional wave shear stress $\overline{\widetilde{u}\widetilde{w}}$ for different experimental conditions. a) Experimental $\overline{\widetilde{u}\widetilde{w}}$ (symbols) for PpW1–4, paddle waves plus following wind (same reflection, same LDV section, different wind). Symbol size is proportional to the wind speed. b) Experimental $\overline{\widetilde{u}\widetilde{w}}$ (symbols) for experiments PoW1–5, paddle waves with opposing wind (different reflection, same LDV section, same wind). Symbol transparency is proportional to the paddle wave reflection. c) Experimental $\overline{\widetilde{u}\widetilde{w}}$ (symbols) for experiments PoW2$a$–$d$ (same reflection, different LDV section, same wind). d) Comparison of $\overline{\widetilde{u}\widetilde{w}}$ among experiments with similar reflection and different wind conditions: P1 (grey small symbol with dotted line) for no wind, PpW4 (empty small symbol with solid line) for following wind, PoW4 (big blue symbol) for opposing wind. All values are non-dimensional with respect to $H_t^2T^{-2}$.

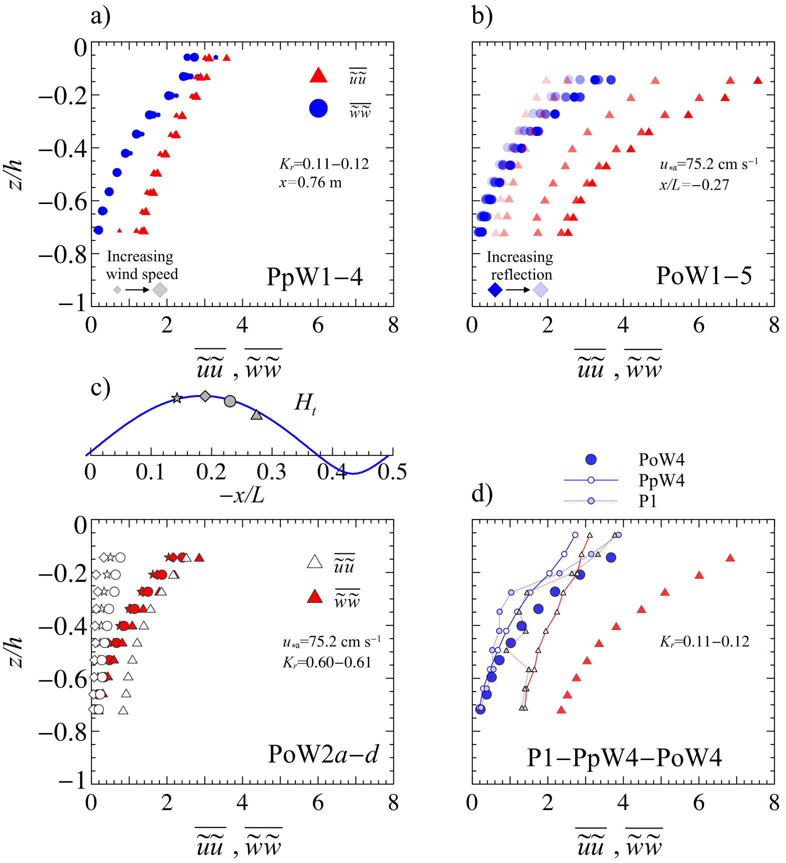

Figure 5.3: Comparison of the non-dimensional wave normal stresses $\overline{\tilde{u}\tilde{u}}$ and $\overline{\tilde{w}\tilde{w}}$ for different experimental conditions. a) Horizontal $\overline{\tilde{u}\tilde{u}}$ (red triangle) and vertical $\overline{\tilde{w}\tilde{w}}$ (blue circles) for PpW1–4, paddle waves plus following wind (same reflection, same LDV section, different wind). Symbol size is proportional to the wind speed. b) Horizontal (red triangles) and vertical (blue circles) wave normal stresses for experiments PoW1–5, paddle waves with opposing wind (different reflection, same LDV section, same wind). Symbol transparency is proportional to the paddle wave reflection. c) Horizontal (empty symbols) and vertical (blue symbols) wave normal stresses for experiments PoW2$a$–$d$ (same reflection, different LDV section, same wind). d) Comparison of $\overline{\tilde{u}\tilde{u}}$ and $\overline{\tilde{w}\tilde{w}}$ among experiments with similar reflection and different wind conditions: P1 (grey small symbol with dotted line) for no wind, PpW4 (empty small symbol with solid line) for following wind, PoW4 (big blue symbol) for opposing wind. All values are non-dimensional with respect to $H_t^2T^{-2}$.

## 5.3 Turbulent normal and shear stresses

The turbulent stresses are calculated from the turbulent components of the velocity signals, which are obtained after applying a mean and a phase average, i.e. after subtracting from the initial signal the mean and orbital (wave-induced) velocities.

Figure 5.4a) shows the non-dimensional turbulent shear stress (covariance) $\overline{\widetilde{u'w'}}$ for experiments PpW1–4, reporting the different vertical profiles varying the wind speed. The results show that, for increasing wind speed, the non-dimensional turbulent shear stresses are larger (in modulus), in particular near the free surface where the effects of the wind are stronger. We already discussed the sign of the turbulent covariance (negative), which suggests a net momentum transfer from air to water, as expected in the presence of wind.

Figure 5.4b) reports the non-dimensional turbulent shear stress for experiments PoW1–5, with same opposing wind, different reflection and same LDV measurements section. The results show that, for increasing reflection, the non-dimensional turbulent shear stress decreases. We remind that the velocity (and stress) scale refers to the wave component, hence a reduction of the non-dimensional turbulent component means a minor relative contribution. In this sense the turbulent momentum transfer (for an opposing wind) is less effective at high reflective conditions.

Figure 5.4c) shows the turbulent shear stress for experiments PoW2$a$–$d$, which have same opposing wind and similar reflective conditions, but different LDV measurements sections. The results suggest (as already discussed in chapter §4) a dependence of $\overline{\widetilde{u'w'}}$ on the LDV section, even though we are not able to determine a clear relation.

Figure 5.4d) shows the comparison of $\overline{\widetilde{u'w'}}$ among experiments with similar reflection and different wind conditions (PoW4 for opposing wind, PpW1 for following wind and P1 for the absence of wind). As suggested also by looking at figures 5.4b) and 5.4b), the vertical profiles of the turbulent shear stress have a similar trend if compared to following wind experiments. However, the non-dimensional values are larger for PoW experiments and

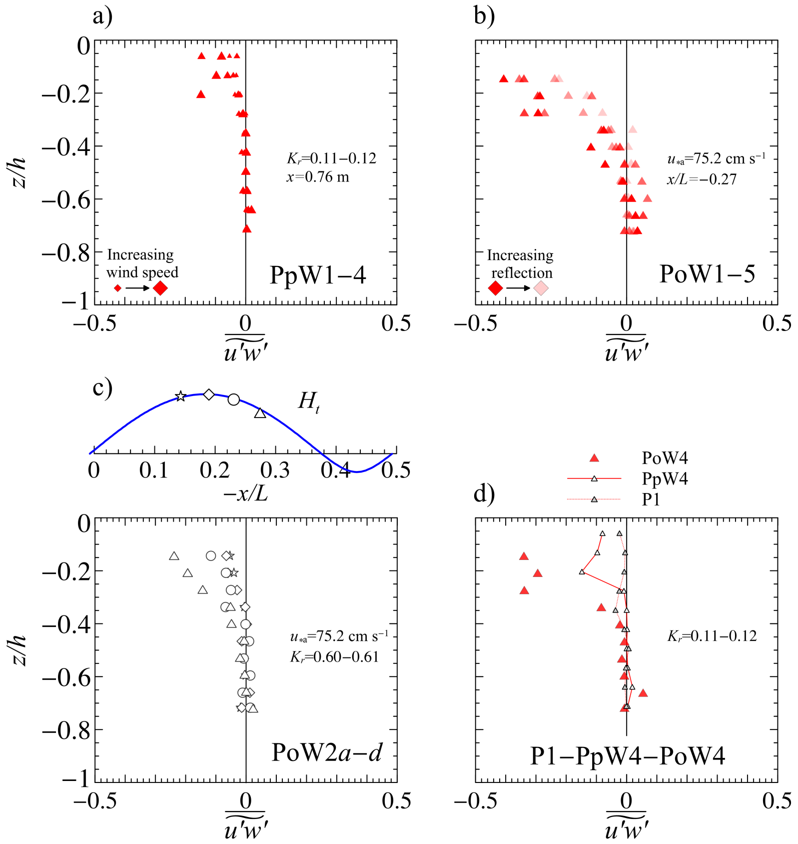

Figure 5.4: Comparison of the non-dimensional turbulent shear stress $\widetilde{\overline{u'w'}}$ for different experimental conditions. a) Experimental $\widetilde{\overline{u'w'}}$ (symbols) for PpW1–4, paddle waves plus following wind (same reflection, same LDV section, different wind). Symbol size is proportional to the wind speed. b) Experimental $\widetilde{\overline{u'w'}}$ (symbols) for experiments PoW1–5, paddle waves with opposing wind (different reflection, same LDV section, same wind). Symbol transparency is proportional to the paddle wave reflection. c) Experimental $\widetilde{\overline{u'w'}}$ (symbols) for experiments PoW2$a$–$d$ (same reflection, different LDV section, same wind). d) Comparison of $\widetilde{\overline{u'w'}}$ among experiments with similar reflection and different wind conditions: P1 (grey small symbol with dotted line) for no wind, PpW4 (empty small symbol with solid line) for following wind, PoW4 (big blue symbol) for opposing wind. All values are non-dimensional with respect to $H_t^2T^{-2}$.

reach lower water levels before going to zero.

Figure 5.5a) shows the non-dimensional turbulent normal stresses $\overline{\widetilde{u'u'}}$ and $\overline{\widetilde{w'w'}}$ for experiments PpW1–4. Both the horizontal and vertical normal stresses are enhanced for increasing wind, and we notice also an increasing anisotropy.

Figure 5.5b) reports the non-dimensional turbulent normal stresses for experiments PoW1–5. For decreasing reflection, it is evident a reduction of both $\overline{\widetilde{u'u'}}$ and $\overline{\widetilde{w'w'}}$ and an increasing anisotropy of the Reynolds turbulent stress tensor.

Figure 5.5c) shows the non-dimensional turbulent normal stresses for experiments PoW2*a*–*d*. The vertical profiles indicate different values of the turbulent normal stresses and of the system anisotropy for different values of the total wave height $H_t$, but the data are too vague to yield a clear conclusion.

Figure 5.5d) shows the comparison of non-dimensional $\overline{\widetilde{u'u'}}$ and $\overline{\widetilde{w'w'}}$ among experiments with similar reflection and different wind conditions (PoW4 for opposing wind, PpW1 for following wind and P1 for the absence of wind). The results confirm the conclusions reported for the turbulent shear stress, since an opposing wind supports higher values of the turbulent stresses; furthermore, we notice a stronger isotropy for the following wind experiments.

## 5.4 Wave and turbulent principal stresses

In the presence of a periodic and a turbulent field, a Reynolds wave stress tensor and a Reynolds turbulent stress tensor can be identified. The Reynolds wave stress tensor is diagonal only for progressive wave, but in partially-reflective conditions the velocities are not in quadrature and the wave shear stress is different from zero. Thus, the wave stress tensor can be diagonalized and the wave principal stresses can be calculated. The Reynolds turbulent stress tensor is not diagonal in general and the turbulent principal stresses can be calculated as well as the wave components.

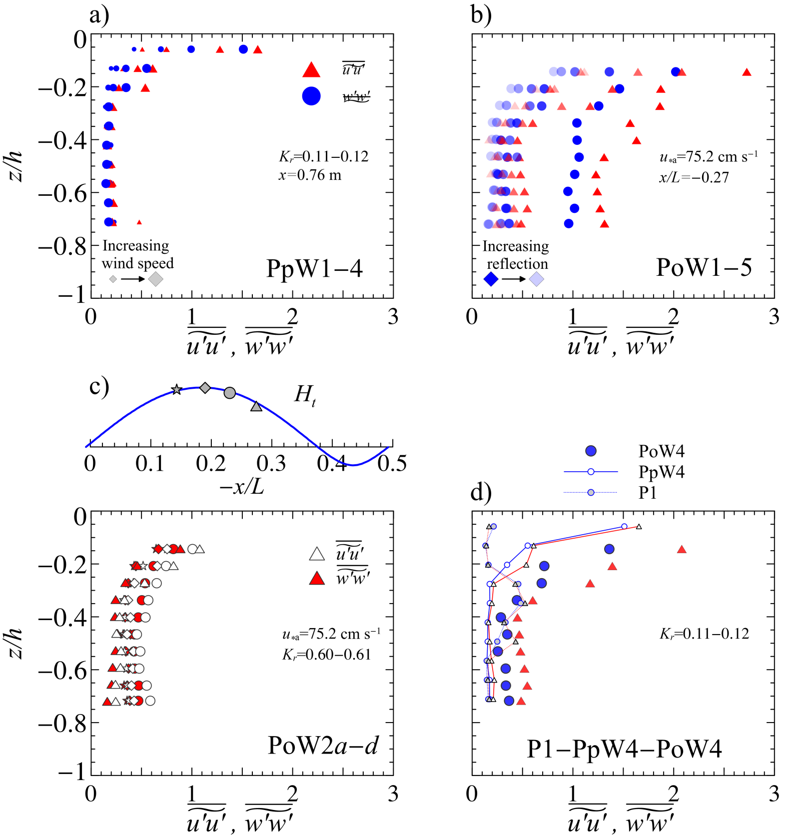

Figure 5.5: Comparison of the non-dimensional turbulent normal stresses $\widetilde{\overline{u'u'}}$ and $\widetilde{\overline{w'w'}}$ for different experimental conditions. a) Horizontal $\widetilde{\overline{u'u'}}$ (red triangle) and vertical $\widetilde{\overline{w'w'}}$ (blue circles) for PpW1–4, paddle waves plus following wind (same reflection, same LDV section, different wind). Symbol size is proportional to the wind speed. b) Horizontal (red triangles) and vertical (blue circles) turbulent normal stresses for experiments PoW1–5, paddle waves with opposing wind (different reflection, same LDV section, same wind). Symbol transparency is proportional to the paddle wave reflection. c) Horizontal (empty symbols) and vertical (blue symbols) turbulent normal stresses for experiments PoW2*a*–*d* (same reflection, different LDV section, same wind). d) Comparison of $\widetilde{\overline{u'u'}}$ and $\widetilde{\overline{w'w'}}$ among experiments with similar reflection and different wind conditions: P1 (grey small symbol with dotted line) for no wind, PpW4 (empty small symbol with solid line) for following wind, PoW4 (big blue symbol) for opposing wind. All values are non-dimensional with respect to $H_t^2T^{-2}$.

Figure 5.6a) shows the wave principal stresses ratio $\widetilde{\sigma}_{\max}/\widetilde{\sigma}_{\min}$ for experiments PpW1–4, which have similar reflective conditions, same LDV section and different following wind speeds. The results almost collapse on the same curve, as expected, and differ in particular for the different phase shift among experiments PpW1–4 and for the presence of wind, which can possibly introduce variations also to the wave principal stresses.

Figure 5.6b) reports the wave principal stresses ratio for experiments PoW1–5 (paddle waves with different reflective conditions, same opposing wind speed and same LDV section). The vertical profiles exhibit an increment of the principal stresses ratio proportional to the reflective conditions.

Figure 5.6c) shows the wave principal stresses ratio for experiments PoW2*a*–*d*, which show the influence of the LDV sections on the principal stresses ratio for similar reflective and same opposing wind conditions. The results show that the LDV measurements section does not only change the values of the wave principal stresses ratio, but modifies also the shape of the vertical profiles

Figure 5.6d) shows the comparison of $\widetilde{\sigma}_{\max}/\widetilde{\sigma}_{\min}$ among experiments with similar reflection and different wind conditions (PoW4 for opposing wind, PpW1 for following wind and P1 for the absence of wind). The results show a similar shape of the vertical profiles, with the largest and smallest values belonging to PpW4 and P1, respectively.

Figure 5.7a) shows the turbulent principal stresses ratio $\sigma'_{\max}/\sigma'_{\min}$ for experiments PpW1–5. The vertical line equal to one indicates isotropy of the principal stress tensor. We observe that the system is more anisotropic approaching the surface, and the maximum isotropy is reached at $z/h \approx -0.4$. It is not clear a dependence of the principal stresses ratio on the different wind speeds.

Figure 5.7b) reports the turbulent principal stresses ratio for experiments PoW1–5. The results show a similar trend if compared to experiments PpW1–4, with maximum and minimum isotropy reached about the middle of the water column and near the surface, respectively. The experimental values are quite disperse, but suggest an influence of the reflection conditions on the anisotropy of the system which should be further investigated.

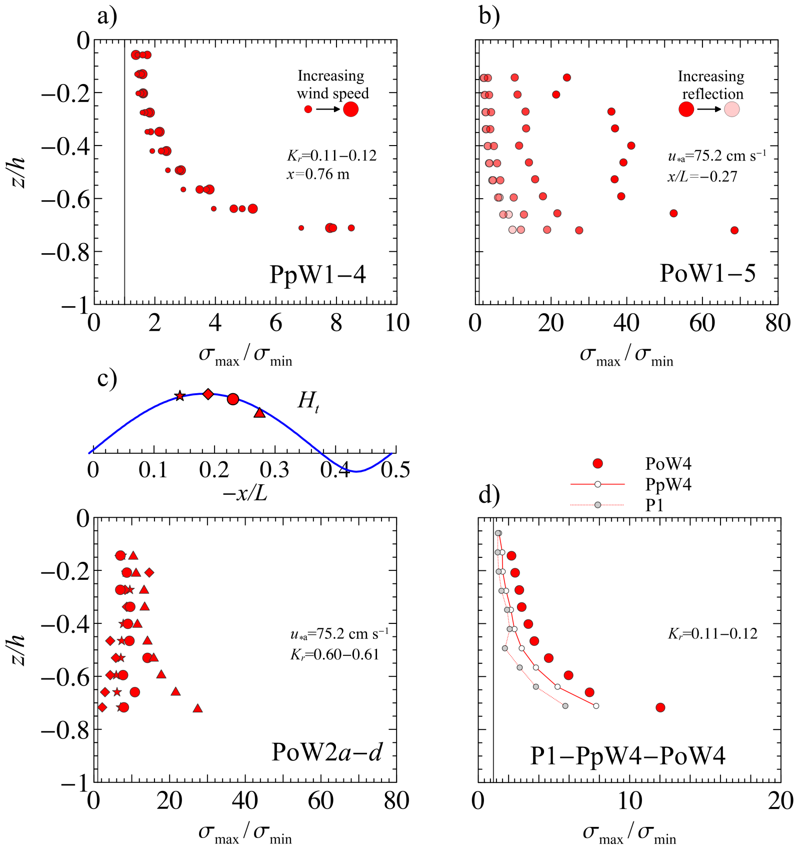

Figure 5.6: Comparison of the non-dimensional wave principal stress ratio $\widetilde{\sigma}_{\max}/\widetilde{\sigma}_{\min}$ for different experimental conditions. a) Experimental $\overline{\widetilde{u}\widetilde{w}}$ (symbols) for PpW1–4, paddle waves plus following wind (same reflection, same LDV section, different wind). Symbol size is proportional to the wind speed. b) Experimental $\widetilde{\sigma}_{\max}/\widetilde{\sigma}_{\min}$ (symbols) for experiments PoW1–5, paddle waves with opposing wind (different reflection, same LDV section, same wind). Symbol transparency is proportional to the paddle wave reflection. c) Experimental $\widetilde{\sigma}_{\max}/\widetilde{\sigma}_{\min}$ (symbols) for experiments PoW2$a$–$d$ (same reflection, different LDV section, same wind). d) Comparison of $\widetilde{\sigma}_{\max}/\widetilde{\sigma}_{\min}$ among experiments with similar reflection and different wind conditions: P1 (grey small symbol with dotted line) for no wind, PpW4 (empty small symbol with solid line) for following wind, PoW4 (big blue symbol) for opposing wind. All values are non-dimensional with respect to $H_t^2T^{-2}$.

Figure 5.7c) shows the turbulent principal stresses ratio for experiments PoW2*a–d*. Again, we notice the maximum anisotropy of the turbulent principal stress tensor near the interface between air and water and a not-well-defined dependence on the LDV measurement section.

Figure 5.7d) shows the comparison of $\sigma'_{\mathrm{max}}/\sigma'_{\mathrm{min}}$ among experiments with similar reflection and different wind conditions (PoW4 for opposing wind, PpW1 for following wind and P1 for the absence of wind). The results show the different behaviour of the turbulent principal stress tensor for different wind conditions, with maximum anisotropy for opposing wind and a much evident isotropy of the no-wind condition over almost the entire column.

## 5.5 Quadrant analysis

The quadrant analysis is a technique used for defining the turbulent structure and the dominant turbulent momentum flux events on the basis of the coupled signs of the turbulent horizontal and vertical velocities, with applications also in the characterization of the turbulent airflow over wind-generated waves (see Longo, 2012; Buckley & Veron, 2018). We have already determined that the dominant event-averaged shear stresses are $S_2$ and $S_4$, which belong to the second and the fourth quadrants, respectively. Thus, we focus our investigations in figure 5.8 on those two elements($S_4$ is shown with opposite sign in order to obtain a better visualization of the results).

Figure 5.8a) shows the dominant event-averaged shear stresses $S_2$ and $-S_4$ for experiments PpW1–4, paddle waves with similar reflective conditions, same LDV measurements section and different following wind speeds. The event-averaged shear stresses are proportional to the wind speed and much larger in proximity of the free surface, with a major contribution of $S_2$.

Figure 5.8b) reports the dominant event-averaged shear stresses for experiments PoW1–5, which report paddle waves with different reflection, same LDV section and same opposing wind speed. We can observe again

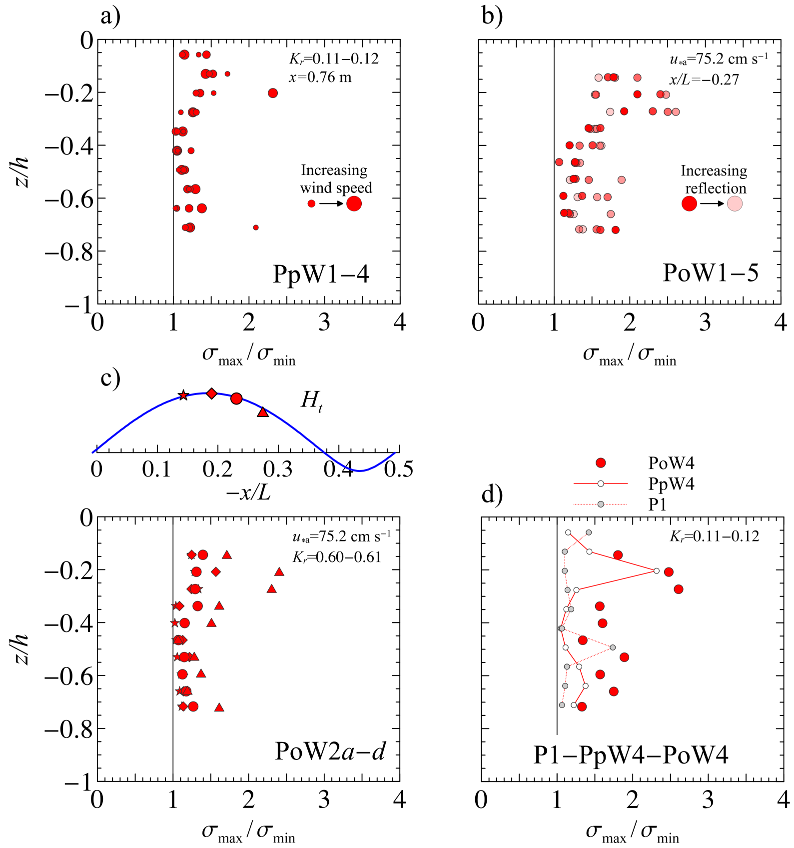

Figure 5.7: Comparison of the non-dimensional turbulent principal stress ratio $\sigma'_{\max}/\sigma'_{\min}$ for different experimental conditions. a) Experimental $\sigma'_{\max}/\sigma'_{\min}$ (symbols) for PpW1–4, paddle waves plus following wind (same reflection, same LDV section, different wind). Symbol size is proportional to the wind speed. b) Experimental $\sigma'_{\max}/\sigma'_{\min}$ (symbols) for experiments PoW1–5, paddle waves with opposing wind (different reflection, same LDV section, same wind). Symbol transparency is proportional to the paddle wave reflection. c) Experimental $\sigma'_{\max}/\sigma'_{\min}$ (symbols) for experiments PoW2$a$–$d$ (same reflection, different LDV section, same wind). d) Comparison of $\sigma'_{\max}/\sigma'_{\min}$ among experiments with similar reflection and different wind conditions: P1 (grey small symbol with dotted line) for no wind, PpW4 (empty small symbol with solid line) for following wind, PoW4 (big blue symbol) for opposing wind. All values are non-dimensional with respect to $H_t^2T^{-2}$.

that $S_2$ gives the dominant contribution and that events are stronger near the surface. Furthermore, we notice that the effect of increasing reflection is to reduce the intensity of the event-averaged shear stresses. In particular, for the condition with minimum reflection the turbulent shear stress can penetrate deeper into the water column.

Figure 5.8c) shows the dominant event-averaged shear stresses for experiments PoW2*a*–*d*. These experiments show that also the event-averaged turbulent shear stresses are influenced by the LDV section (for similar reflective conditions and same opposing wind speeds). In fact, we observe that also at consistent reflection coefficients ($K_r \approx 0.6$) the turbulent shear stresses can be relevant in the entire measurements vertical domain.

Figure 5.8d) shows the comparison of $S_2$ and $-S_4$ among experiments with similar reflection and different wind conditions (PoW4 for opposing wind, PpW1 for following wind and P1 for the absence of wind). The presence of wind induces stronger events near the surface, which are more intense for opposing wind. However, wind action is less effective towards the bottom where the values of the different experiments are very similar.

Figure 5.9 shows the time-averaged shear stresses contribution (total and decomposed for each quadrant) for experiments PoW4 (opposing wind), PpW1 (following wind) and P1 (in the absence of wind) in order to determine and compare the turbulent structure among experiments with similar reflection and different wind conditions. The results indicate that, in the presence of wind (both following or opposing) the main input comes from the interface between air and water. Furthermore we notice that, for opposing wind, the turbulent shear stresses are more intense and go to deeper water levels. In the case of wind absence, the dominant turbulent shear stresses still belong to the second and the fourth quadrant, but major intensities are observed in about the middle of the water depth.

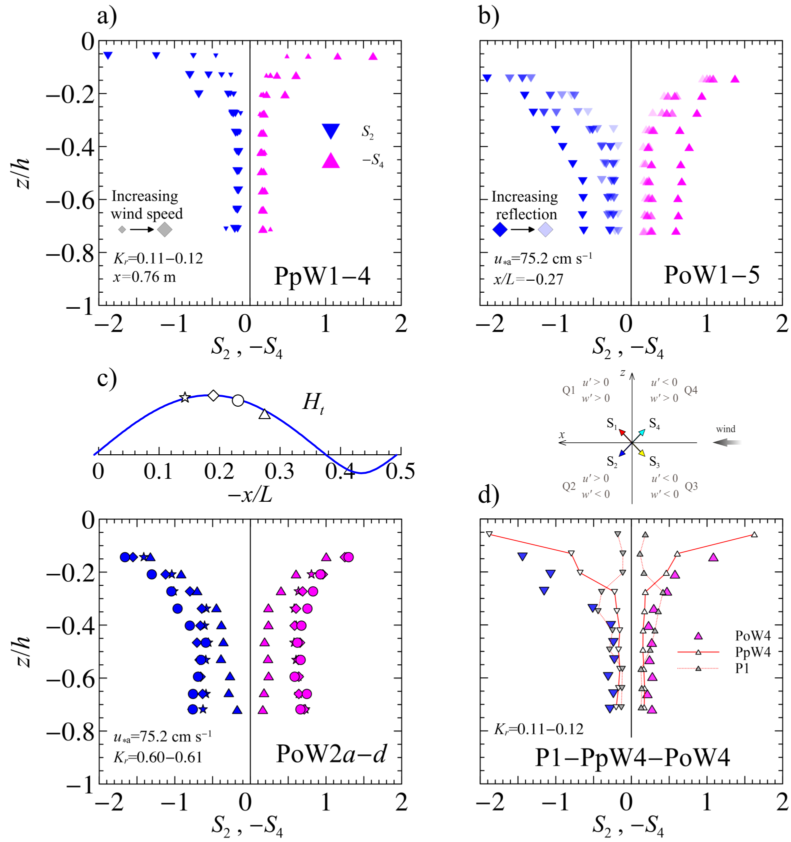

Figure 5.8: Comparison of the dominant non-dimensional event-averaged shear stresses $S_2$ and $-S_4$ (from quadrant analysis) for different experimental conditions. The inward interaction contribution ($S_4$) is shown with opposite sign for a better visualization of the results. a) Experimental $S_2$ (down-pointing blue triangles) and $-S_4$ (up-pointing magenta triangles) for PpW1–4, paddle waves plus following wind (same reflection, same LDV section, different wind). Symbol size is proportional to the wind speed. b) Experimental $S_2$ (down-pointing blue triangles) and $-S_4$ (up-pointing magenta triangles) for experiments PoW1–5, paddle waves with opposing wind (different reflection, same LDV section, same wind). Symbol transparency is proportional to the paddle wave reflection. c) Experimental $S_2$ (down-pointing blue triangles) and $-S_4$ (up-pointing magenta triangles) for experiments PoW2$a$–$d$ (same reflection, different LDV section, same wind). d) Comparison of $S_2$ (down-pointing triangles) and $S_4$ (up-pointing triangles) among experiments with similar reflection and different wind conditions: P1 (grey small triangle with dotted line) for no wind, PpW4 (empty small triangle with solid line) for following wind, PoW4 (big triangle) for opposing wind. All values are non-dimensional with respect to $H_t^2T^{-2}$.

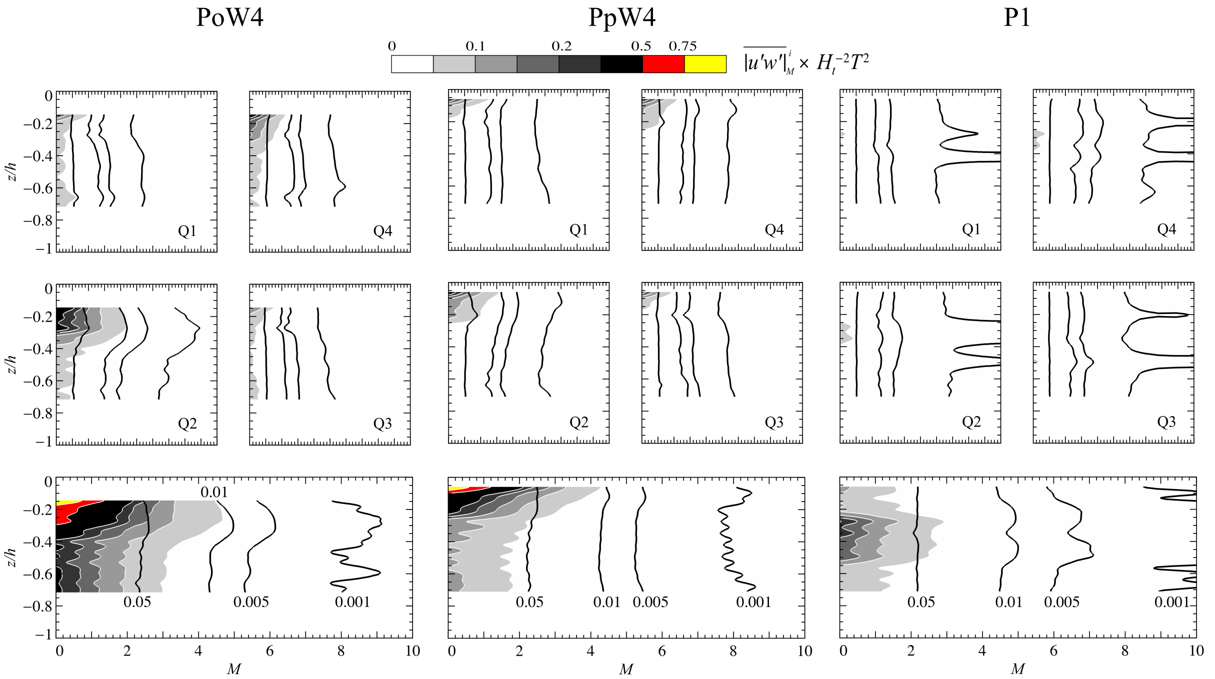

Figure 5.9: Comparison of the time-averaged shear stresses (total and in each quadrant decomposed) among experiments with similar reflection and different wind conditions: left panels show experiment PoW4 (opposing wind), central panels show experiment PpW4 (following wind) and right panels show experiment P1 (no wind). The time-averaged shear stress is shown in each quadrant decomposed (upper panels) and without decomposition (lower panels), as a function of the threshold parameter $M$. The isolines of the duration fraction (concentration) are superimposed. All stresses are non-dimensional with respect to $H_t^2 T^{-2}$.

# Conclusions

### A short summary of the activity

The main aim of this thesis is to shed light about the influence that partial reflection, which is the most common case encountered both in field and laboratory studies, exerts on a wave field where regular waves are present alone and under the action of following or opposing wind.

We have analysed experimentally and theoretically the flow field of paddle waves, paddle waves plus following wind and paddle waves with opposing wind under partial reflection conditions in laboratory, in terms of free surface elevations, velocities and stresses.

For the theoretical and experimental analyses of the flow field, we consider velocities and free surface elevations as a superposition of a mean, a periodic (wave) and a turbulent (fluctuating) component.

A theoretical model for the periodic (wave) component is developed by means of a perturbation scheme which considers the wave field as a superposition of an incident, a reflected and a bound wave. The phase shift between the incident and the reflected wave is included in the analysis. The theory yields an analytical formulation of the wave components of velocities and stresses, and a spatial variation of the mean water level. The model also predicts the principal stresses, as well as the angle of the principal axes, of both the Reynolds wave and turbulent stress tensors.

The wave flume used for the experimental activity provides a complete control of the generated and reflected wave conditions, and is used to investigate the influence of partial reflection on the main variables of interest, i.e. velocity and free surface elevation, and the combined effect of regular waves and wind action.

We measure velocity and free surface elevation in two different sets of experiments: in the first series, paddle waves (P) and paddle waves plus following wind (PpW) are observed and studied; in the second series, paddle waves with opposing wind (PoW) are observed and studied.

Data analysis allows a complete representation of the experimental velocities, stresses and free surface characteristics of the flow field. Time average yields the mean components, phase average yields the wave (periodic) components, while the residual part (after time and phase average) represents the fluctuating components. A spectral filter is also used for the separation of the free surface elevation component attributed to the paddles (wave) and to the wind (turbulent). Several analyses of velocity and free surface data are performed to quantify the experimental contributions of the separated components.

The discussions of the two series of experiments (reported at the end of the chapters 3 and 4, respectively) show separately the main results of the activities, while chapter 5 offers a unified vision of the results and their comparison. The scope of this chapter is to summarize the advances brought by this thesis in the wide scenario of swell and wind waves interaction under partially-reflective conditions.

## The role of partial reflection in data analysis

The reflection analysis performed in this work allows the theoretical representation of all quantities observed and calculated. We remark that the inclusion of the phase shift between the incident and the reflected waves is a novelty and is essential for a correct reconstruction of the measured wave field. The physical meaning of the phase shift can be easily explained if compared to a well-known solution. If we consider the case of perfect reflection, hence implicitly assuming an impermeable boundary (like a wall), the maximum wave height (antinodes) and the minimum wave height (nodes) appear at the boundary section and at a distance of one quarter of the wave length, respectively. But if the two wave trains (incident and reflected) have a different phase, hence a non-null phase shift, the nodes and the antinodes move along the horizontal coordinate according to the sign and the value of the phase shift. The goodness of the comparison between theory and experiments (hence the prediction of the results) relies entirely on an adequate reflection analysis.

### Free surface elevation

The wave profiles show a modulation induced by reflection and by the section of measurements, and in the presence of following or opposing wind larger fluctuations (corresponding to the wind waves) are observed. The wind waves (separated through a spectral filter) grow in average with fetch length, more evidently in the case of swell following wind. A reduction of the wind wave height in the last part of the fetch is observed in particular for swell opposing wind, physically justified by micro-breaking. The wind waves mean peak period grows monotonically for increasing fetch length, as expected. The phase celerities of the wind waves (for swell opposing wind) are well represented by a dispersion relation which is a perturbed version of the linear dispersion relation, where the higher-order terms take into account the vertical shear of the horizontal velocity.

Partial reflection also induces an imbalance in the conservation of the radiation stress along the horizontal which is interpreted as a spatial variation of the mean water level. The theoretical model gives the exact evolution of the mean water level and observations confirm that the interpretation given to the phenomenon is correct.

### The effects of an opposing wind on a partially-reflected wave environment

Several effects of opposing wind are observed by comparing the results in the presence and in the absence of wind for the same experimental conditions. Observations indicate that the wave shape, in the presence of opposing wind, is clearly distorted (if compared to the wave shape in the absence of wind) at high reflection intensity, while for reflection tending to zero the phase-averaged wave profiles collapse for the two cases (wind and no-wind conditions).

Reflection parameters are also influenced by the presence of opposing wind: in particular, measurements report an attenuation of the incident wave height, a reduction of the reflection coefficient and an additional negative phase shift. The reflection coefficient, the phase shift and the incident wave height govern the sign and the intensity of the momentum transfer due to the Reynolds wave shear stress; thus, it is important to understand the response of these parameters to the external forcings of the system.

We believe that further studies are highly recommended in order to capture the physical mechanism of the interactions between swell and wind waves in partially-reflected environments, determining analytical relations which increase the reliability of the current numerical models.

### Wave shear stress variability for waves under partial reflection conditions

One of the main reasons of this thesis is to understand and quantify the role of the Reynolds wave shear stress. The importance of this element emerges in all experiments and it is also more evident if compared to the values of the turbulent shear stress, which usually in literature represents the element of greatest interest. In our work, we derive theoretically, observe and then compare the values of the Reynolds wave shear stress in different configurations: for paddle waves, paddle waves with following wind and paddle waves with opposing wind.

All results clearly show the main role of the wave shear stress for partially-reflected wave field, even for small values of the reflection coefficient. In particular, we notice that the wave shear stress can be large or small, positive or negative depending on two factors: (i) reflection parameters, i.e. the reflection coefficient and the phase shift, as a straightforward (but not obvious) consequence of the reflective conditions; (ii) the section of measurements, indicating a spatial modulation of the wave shear stress along horizontal coordinate (in our case is along the wave flume, but in general it can take place also in the open sea). We also highlight that the wave shear stress (hence, the effects of the partial reflection) are larger near the surface, thus having a strong influence on the exchanges (of heat, substance and momentum) which take place at the interface between air and water.

Considering that partial reflection is almost ubiquitous in nature and also in controlled environments like laboratory activities, it means that this element is always to be taken into account and accurately evaluated for a correct interpretation of the observed data.

### A fundamental tool for the correct evaluation of the turbulent momentum transfer

In general, the vertical profile and the sign of the turbulent shear stresses can help in individuating a transfer of momentum from the air to the water (or vice versa), even though the simple observation of the total shear stress does not give a complete information about the real momentum transfer. For example, a negative sign of the turbulent shear stress at the interface can be associated to a transfer of momentum from the air to the water only for positive horizontal velocity and negative vertical velocity, which determines an injection of momentum from the top, while a negative horizontal velocity with a positive vertical velocity determines an opposite transfer of momentum, i.e. from the bottom to the top.

An appropriate approach to the problem is represented by the quadrant analysis, since it classifies the events on the basis of the combined signs of the fluctuating velocities, both horizontal and vertical. The results of the quadrant analysis of our experiments show a net transfer of momentum from the air to the water in the presence of wind (both following and opposing), with dominant components represented by the outward and inward interactions. For following wind, the joint probability density functions of the fluctuating velocities also confirm the versus of the momentum transfer.

### Wave and turbulent Reynolds stress tensors

The Reynolds wave and turbulent stress tensors are composed by shear (examined in the previous paragraphs) and normal components.

The normal components of the periodic Reynolds tensor show a good agreement with the theoretical predictions equally for paddle waves, paddle waves plus following wind and paddle waves with opposing wind. In particular, we notice that partial reflection conditions induce a modulation of the normal stresses, which is stronger for the horizontal component. Also, we notice that near the surface the experimental values depart slightly from the theoretical profile, possibly due to the presence of nonlinear interactions and other factors which take place at the interface and more evident in the presence of wind (both following and opposing).

The normal components of the Reynolds turbulent stress tensors are almost isotropic in the absence of wind; in the presence of wind, the vertical profile of the horizontal and vertical components diverges and the difference between the experimental values increases from the bottom to the top. In case of opposing wind, this is more evident and the anisotropy increases for decreasing reflection. We notice also that the turbulent stresses are enhanced for decreasing reflection, which suggests that reflection acts as an inhibitor for the turbulent momentum exchange in case of opposing wind.

The principal stresses and angle of the principal axes complete the analysis of the turbulent and periodic Reynolds stress tensors. The ratio between the maximum and the minimum stress indicates the anisotropy (or isotropy) of the diagonalized tensor. Our results show an isotropic behaviour in the absence of wind for the turbulent principal stresses, while in the presence of wind (both following and opposing) the diagonized turbulent tensor is isotropic toward the bottom while it shows a remarkable anisotropy near the surface, where the turbulent structure induced by the wind is more defined. The ratio of the wave principal stresses shows that the diagonalized wave tensor is strongly anisotropic and well predicted by the theoretical model; furthermore, its values tend to the turbulent principal stresses ratio for decreasing reflection.

The principal angle is observed for the turbulent and wave Reynolds tensors. The turbulence principal angle shows that in proximity of the surface the dominant effect is determined by a uniform shear rate current in the presence of wind (both following and opposing), even though a dispersion of the data is observed and possibly due to the effects of partial reflection conditions.

### Implications for atmosphere-ocean exchange models

Transfer of different species (momentum, gasses, heat) at the interface between ocean and atmosphere has been widely modeled, thanks to the increasing availability of data, better computational resources used for simulations and accuracy of the models. However, global models have need to include simplifications of physical processes and cannot always take into account all the significant variables.

To the knowledge of the authors, the phase shift is not taken into consideration even in those including reflection analysis. However, some analytical works (Nielsen *et al.*, 2011; Deigaard & Nielsen, 2018) show that the role of the phase for spatially growing stationary waves and time-growing uniform waves, i.e. for swell subjected to the action of the wind cannot be disregarded and is further confirmed in this thesis.

This is just an example of the potential application of the results presented in this thesis for the refinements of the current ocean-atmosphere coupled models. We believe that this work could provide some insight and inspire researchers towards experimental, numerical and field studies of swell and wind waves, in order to improve the ocean weather forecasting used nowadays to predict and mitigate the impacts on the human life and the existing ecosystems.

### Highlights

The overall work here presented show extensive results about swell and wind interactions under partial reflection conditions. Most of them confirm the results given by the previous literature and extend the results with novel experimental and theoretical observations through well-known and accepted techniques, like perturbation methods and the triple decomposition.

All the analyses reveal the importance of an adequate method to describe the combined effects of different components in a complex field like the one which is studied in this thesis, where nonlinear effects, boundary conditions, experimental conditions and measuring techniques can affect the results and conduct to misleading interpretations. Furthermore, the inclusion of the reflection coefficient and phase shift between the incident and reflected waves solves the problem of the variability of the wave shear stress in swell and wind waves, which has been found in literature, with new experimental results to support the theoretical model.

These results are very encouraging towards new studies which, taking advantage of the present work, aim to provide an extended view of the complexity given by the fascinating world of water waves.

# Abbreviations

| | |
|---|---|
| **2D-LDV** | Two-component Laser Doppler Velocimeter |
| **CIAO** | Ocean-Atmosphere Interaction Flume |
| **MWL** | Mean water level |
| **RPM** | Revolutions per minute |
| **P** | Experimental tests with Paddle waves |
| **PpW** | Experimental tests with Paddle waves plus following Wind |
| **PoW** | Experimental tests with Paddle waves with opposing Wind |
| **US** | Acoustic wave gauge |

# Notation

## Latin Letters

| | | |
|---|---|---|
| $c$, $c_{exp}$ | Phase celerity (theoretical and experimental) | $\mathrm{m\,s^{-1}}$ |
| $c_{g,exp}$ | Experimental wave group celerity | $\mathrm{m\,s^{-1}}$ |
| $f$ | Wave frequency | Hz |
| $f_{peak}$ | Wave peak frequency | Hz |
| $h$ | Water depth | m |
| $k$ | Wave number | $\mathrm{m^{-1}}$ |
| $p$ | Total pressure | Pa |
| $p_0$ | Hydrostatic pressure | Pa |
| $t$ | Time | s |
| $u$ | Horizontal velocity | $\mathrm{m\,s^{-1}}$ |
| $\overline{u}$ | Time-averaged horizontal velocity (mean component) | $\mathrm{m\,s^{-1}}$ |
| $\widetilde{u}$ | Phase-averaged horizontal velocity (periodic component) | $\mathrm{m\,s^{-1}}$ |
| $u'$ | Fluctuating horizontal velocity (turbulent component) | $\mathrm{m\,s^{-1}}$ |
| $u_{*a}$ | Wind friction velocity | $\mathrm{m\,s^{-1}}$ |
| $w$ | Vertical velocity | $\mathrm{m\,s^{-1}}$ |
| $\overline{w}$ | Time-averaged vertical velocity (mean component) | $\mathrm{m\,s^{-1}}$ |

| | | |
|---|---|---|
| $\widetilde{w}$ | Phase-averaged vertical velocity (periodic component) | $\mathrm{m\,s^{-1}}$ |
| $w'$ | Fluctuating vertical velocity (turbulent component) | $\mathrm{m\,s^{-1}}$ |
| $x-$ | Horizontal coordinate of the reference system | m |
| $z-$ | Vertical coordinate of the reference system | m |
| $z_0$ | Aerodynamic roughness length | m |
| $-\overline{\widetilde{u}\widetilde{w}}$ | Reynolds wave shear stress | $\mathrm{m^2\,s^{-2}}$ |
| $\overline{\widetilde{w}\widetilde{\omega}}$ | Oscillatory vorticity | $\mathrm{m\,s^{-2}}$ |
| $\overline{\widetilde{u}\widetilde{u}}$, $\overline{\widetilde{u}\widetilde{w}}$, $\overline{\widetilde{w}\widetilde{w}}$ | Periodic correlation (covariance) | $\mathrm{m^2\,s^{-2}}$ |
| $\overline{\widetilde{u'u'}}$, $\overline{\widetilde{u'w'}}$, $\overline{\widetilde{w'w'}}$ | Turbulent correlation (covariance) | $\mathrm{m^2\,s^{-2}}$ |
| $E$ | Wave energy density | $\mathrm{N\,m^{-1}}$ |
| $H$ | Wave height | m |
| $H_{1/3}$ | Average of the one third maximum wave height | m |
| $H_{1/10}$ | Average of the one tenth maximum wave height | m |
| $H_\mathrm{m}$ | Mean wave height | m |
| $H_\mathrm{rms}$ | Root mean square wave height | m |
| $H_{i,\mathrm{rms}}$ | Root mean square wave height of the incident wave | m |
| $H_t$ | Total wave height | m |
| $K_r$ | Reflection coefficient | |
| $K_{r,w}$ | Reflection coefficient under wind conditions | |
| $L$ | Wave length | m |
| $L_{peak}$ | Wave length associated to the peak frequency | m |
| $M$ | threshold parameter | |
| $N$ | Number of samples in a measurement | |

| | | |
|---|---|---|
| $N_j$ | Number of samples in a measurement belonging to the $j$-th quadrant | |
| $N_w$ | Number of waves | |
| $S_j$ | Event-averaged shear stress | $\mathrm{m}^2\,\mathrm{s}^{-2}$ |
| $S_{xx}$ | Wave-induced component of the radiation stress | $\mathrm{N\,m}^{-1}$ |
| $T$ | Wave period | s |
| $T_{1/3}$ | Average of the one third maximum wave period | s |
| $T_{1/10}$ | Average of the one tenth maximum wave period | s |
| $T_m$ | Mean wave period | s |
| $T_{acq}$ | Sampling time | s |
| $U$ | Wind velocity | $\mathrm{m\,s}^{-1}$ |
| $\langle ... \rangle_i$, $\langle ... \rangle_r$, $\langle ... \rangle_b$ | Incident, reflected and bound component | |

# Greek Letters

| | | |
|---|---|---|
| $\Delta\varphi$ | Phase shift | rad |
| $\Delta\varphi_w$ | Phase shift under wind conditions | rad |
| $\varphi$ | Phase | rad |
| $\Delta x$ | Distance between two adjacent sensors | m |
| $\Delta\tau$ | Temporal lag between two adjacent sensors | s |
| $\epsilon$ | Small parameter for the series expansion | |
| $\eta$ | Free surface elevation | m |
| $\omega$ | Radial frequency | Hz |
| $\Phi$ | Wave velocity potential | $\mathrm{m\,s}^{-2}$ |
| $\sigma$ | Principal Reynolds stress | $\mathrm{m}^2\,\mathrm{s}^{-2}$ |
| $\widetilde{\sigma}$ | Principal Reynolds wave stress | $\mathrm{m}^2\,\mathrm{s}^{-2}$ |
| $\sigma'$ | Principal Reynolds turbulent stress | $\mathrm{m}^2\,\mathrm{s}^{-2}$ |
| $\alpha$ | Principal Reynolds wave angle | rad |
| $\widetilde{\alpha}$ | Principal Reynolds angle | rad |

| | | |
|---|---|---|
| $\alpha'$ | Principal Reynolds turbulent angle | rad |
| $\overline{\zeta}$ | Mean water level | m |

# Bibliography

ADDONA, F., LOARCA, A. LIRA, CHIAPPONI, L., LOSADA, M.A. & LONGO, S. 2018 The Reynolds wave shear stress in partially reflected waves. *Coastal Engineering* **138**, 220–226.

ARDHUIN, F. & ROLAND, A. 2012 Coastal wave reflection, directional spread, and seismoacoustic noise sources. *Journal of Geophysical Research: Oceans* **117** (C11).

BAQUERIZO, A. 1995 Reflexión del oleaje en playas. métodos de evaluación y de predicción (in Spanish). PhD thesis, Universidad de Cantabria, Santander.

BAQUERIZO, A. & LOSADA, M.Á. 1999*a* Sediment transport around a mound breakwater: The toe erosion problem. In *Proceedings of Coastal Engineering 1998*, pp. 1720–1729.

BAQUERIZO, A. & LOSADA, M. A. 1999*b* Wave height to depth ratio in front of coastal structures. In *Proceedings of Coastal Structures*, pp. 23–28.

BAQUERIZO, A., LOSADA, M. A., SMITH, J. M. & KOBAYASHI, N. 1997 Cross-shore variation of wave reflection from beaches. *Journal of Waterway, Port, Coastal, and Ocean Engineering* **123** (5), 274–279.

BAUER, J. E., CAI, W.-J., RAYMOND, P. A, BIANCHI, T. S., HOPKINSON, C. S. & REGNIER, P. A. G. 2013 The changing carbon cycle of the coastal ocean. *Nature* **504** (7478), 61–70.

Belcher, S.E., Harris, J.A. & Street, R.L. 1994 Linear dynamics of wind waves in coupled turbulent air—water flow. Part 1. theory. *Journal of Fluid Mechanics* **271**, 119–151.

Bendat, J.S. & Piersol, A.G. 2000 *Random data analysis and measurement procedures*. Wiley & Sons, New York.

Bopp, L., Le Quéré, C., Heimann, M., Manning, A.C. & Monfray, P. 2002 Climate-induced oceanic oxygen fluxes: Implications for the contemporary carbon budget. *Global Biogeochemical Cycles* **16** (2).

Borges, A. V. 2005 Do we have enough pieces of the jigsaw to integrate $CO_2$ fluxes in the coastal ocean? *Estuaries* **28** (1), 3–27.

Buckley, M.P. & Veron, F. 2018 The turbulent airflow over wind generated surface waves. *European Journal of Mechanics-B/Fluids* .

Cavaleri, L., Alves, J.-H.G.M., Ardhuin, F., Babanin, A., Banner, M., Belibassakis, K., Benoit, M., Donelan, M., Groeneweg, J., Herbers, T.H.C., Hwang, P., Janssen, P.A.E.M., Janssen, T., Lavrenov, I.V., Magne, R., Monbaliu, J., Onorato, M., Polnikov, V., Resio, D., Rogers, W.E., Sheremet, A., McKee Smith, J., Tolman, H.L., van Vledder, G., Wolf, J. & Young, I. 2007 Wave modelling – The state of the art. *Progress in Oceanography* **75** (4), 603–674.

Chen, G. & Belcher, S.E. 2000 Effects of long waves on wind-generated waves. *Journal of Physical Oceanography* **30** (9), 2246–2256.

Cheung, T.K. & Street, R.L. 1988 The turbulent layer in the water at an air—water interface. *Journal of Fluid Mechanics* **194**, 133–151.

De Serio, F. & Mossa, M. 2013 A laboratory study of irregular shoaling waves. *Experiments in Fluids* **54** (6), 1536.

De Vriend, H.J. & Kitou, N. 1991 Incorporation of wave effects in a 3D hydrostatic mean current model. In *Proceedings of Coastal Engineering 1990*, pp. 1005–1018. Elsevier.

DEIGAARD, R. & FREDSØE, J. 1989 Shear stress distribution in dissipative water waves. *Coastal Engineering* **13** (4), 357–378.

DEIGAARD, R. & NIELSEN, P. 2018 Wind generation of waves: Energy and momentum transfer - An overview with physical discussion. *Coastal Engineering* **139**, 36–46.

DICKSON, A.G., SABINE, C.L. & CHRISTIAN, J.R. 2007 *Guide to best practices for ocean $CO_2$ measurements*. North Pacific Marine Science Organization.

DOBSON, F.W. 1969 Observations of normal pressure on wind-generated sea waves. PhD thesis, University of British Columbia.

DOBSON, F.W. 1971 Measurements of atmospheric pressure on wind-generated sea waves. *Journal of Fluid Mechanics* **48** (1), 91–127.

DONELAN, M.A. 1987 The effect of swell on the growth of wind waves. *John Hopkins APL Tech. Dig.* **8**, 18–23.

DONELAN, M.A., DRENNAN, W.M. & KATSAROS, K.B. 1997 The air–sea momentum flux in conditions of wind sea and swell. *Journal of Physical Oceanography* **27** (10), 2087–2099.

FENNEL, K. 2010 The role of continental shelves in nitrogen and carbon cycling: Northwestern North Atlantic case study. *Ocean Science* **6** (2), 539.

FIECHTER, J., CURCHITSER, E.N., EDWARDS, C.A., CHAI, F., GOEBEL, N.L. & CHAVEZ, F.P. 2014 Air-sea $CO_2$ fluxes in the California Current: Impacts of model resolution and coastal topography. *Global Biogeochemical Cycles* **28** (4), 371–385.

GARRETT, C. & SMITH, J. 1976 On the interaction between long and short surface waves. *Journal of Physical Oceanography* **6** (6), 925–930.

GODA, Y. & ABE, Y. 1968 Apparent coefficient of partial reflection of finite amplitude waves. *Tech. Rep.*. Port and Harbour Research Institute.

Goring, D.G. & Nikora, V.I. 2002 Despiking acoustic doppler velocimeter data. *Journal of Hydraulic Engineering* **128** (1), 117–126.

Grare, L., Peirson, W.L., Branger, H., Walker, J.W., Giovanangeli, J.-P. & Makin, V. 2013 Growth and dissipation of wind-forced, deep-water waves. *Journal of Fluid Mechanics* **722**, 5–50.

Hasselmann, K. 1971 On the mass and momentum transfer between short gravity waves and larger-scale motions. *Journal of Fluid Mechanics* **50** (1), 189–205.

Hsu, C.-T. & Hsu, E.Y. 1983 On the structure of turbulent flow over a progressive water wave: theory and experiment in a transformed wave-following coordinate system. Part 2. *Journal of Fluid Mechanics* **131**, 123–153.

Hussain, A.K.M.F. & Reynolds, W.C. 1970 The mechanics of an organized wave in turbulent shear flow. *Journal of Fluid Mechanics* **41** (2), 241–258.

Kline, S.J., Reynolds, W.C., Schraub, F.A. & Runstadler, P.W. 1967 The structure of turbulent boundary layers. *Journal of Fluid Mechanics* **30** (4), 741–773.

Lachkar, Z., Orr, J. C., Dutay, J.-C. & Delecluse, P. 2007 Effects of mesoscale eddies on global ocean distributions of CFC-11, $CO_2$, and $\Delta^{14}$ C. *Ocean Science* **3** (4), 461–482.

Laruelle, G.G., Dürr, H.H., Slomp, C.P. & Borges, A.V. 2010 Evaluation of sinks and sources of $CO_2$ in the global coastal ocean using a spatially-explicit typology of estuaries and continental shelves. *Geophysical Research Letters* **37** (15).

Laruelle, G.G., Lauerwald, R., Pfeil, B. & Regnier, P. 2014 Regionalized global budget of the $CO_2$ exchange at the air-water interface in continental shelf seas. *Global Biogeochemical Cycles* **28** (11), 1199–1214.

Le Quéré, C., Aumont, O., Bopp, L., Bousquet, P., Ciais, P., Francey, R., Heimann, M., Keeling, C.D., Keeling, R.F., Kheshgi, H., Peylin, P., Piper, S.C., Prentice, I.C. & Rayner, P.J. 2003 Two decades of ocean $CO_2$ sink and variability. *Tellus B* **55** (2), 649–656.

Li, D. & Bou-Zeid, E. 2011 Coherent structures and the dissimilarity of turbulent transport of momentum and scalars in the unstable atmospheric surface layer. *Boundary-Layer Meteorology* **140** (2), 243–262.

Longo, S. 2010 Experiments on turbulence beneath a free surface in a stationary field generated by a Crump weir: free-surface characteristics and the relevant scales. *Experiments in Fluids* **49** (6), 1325–1338.

Longo, S. 2011 Experiments on turbulence beneath a free surface in a stationary field generated by a crump weir: turbulence structure and correlation with the free surface. *Experiments in Fluids* **50** (1), 201–215.

Longo, S. 2012 Wind-generated water waves in a wind tunnel: Free surface statistics, wind friction and mean air flow properties. *Coastal Engineering* **61**, 27–41.

Longo, S., Chiapponi, L., Clavero, M., Mäkelä, T. & Liang, D. 2012 Study of the turbulence in the air-side and water-side boundary layers in experimental laboratory wind induced surface waves. *Coastal Engineering* **69**, 67–81.

Longo, S. & Losada, M.A. 2012 Turbulent structure of air flow over wind-induced gravity waves. *Experiments in Fluids* **53** (2), 369–390.

Longuet-Higgins, M.S. 1969*a* Action of a variable stress at the surface of water waves. *The Physics of Fluids* **12** (4), 737–740.

Longuet-Higgins, M.S. 1969*b* A nonlinear mechanism for the generation of sea waves. *Proceedings of the Royal Society A* **311**, 371–389.

LONGUET-HIGGINS, M.S. & STEWART, R.W. 1960 Changes in the form of short gravity waves on long waves and tidal currents. *Journal of Fluid Mechanics* **8** (4), 565–583.

LONGUET-HIGGINS, M.S. & STEWART, R.W. 1964 Radiation stresses in water waves; a physical discussion, with applications. In *Deep Sea Research and Oceanographic Abstracts*, , vol. 11, pp. 529–562. Elsevier.

LYKKE ANDERSEN, T., CLAVERO, M., FRIGAARD, P., LOSADA, M.A. & PUYOL, J.I. 2016 A new active absorption system and its performance to linear and non-linear waves. *Coastal Engineering* **114**, 47–60.

MACKENZIE, F.T., DE CARLO, E.H. & LERMAN, A. 2011 5.10-Coupled C, N, P, and O Biogeochemical Cycling at the Land–Ocean Interface. *Treatise on Estuarine and Coastal Science* pp. 317–342.

MANSARD, E.P.D. & FUNKE, E.R. 1980 The measurement of incident and reflected spectra using a least squares method. In *Proceedings of Coastal Engineering 1980*, , vol. 1, pp. 154–172.

MASSEY, B.S. 1971 *Units, Dimensional Analysis and Physical Similarity*. Van Nostrand Reinhold Company, London.

MILES, J.W. 1957 On the generation of surface waves by shear flows. *Journal of Fluid Mechanics* **3** (2), 185–204.

MITSUYASU, H. & HONDA, T. 1982 Wind-induced growth of water waves. *Journal of Fluid Mechanics* **123**, 425–442.

MORI, N., SUZUKI, T. & KAKUNO, S. 2007 Noise of acoustic doppler velocimeter data in bubbly flows. *Journal of Engineering Mechanics* **133** (1), 122–125.

NIELSEN, P., CALLAGHAN, D.P. & BALDOCK, T.E. 2011 Downward transfer of momentum by wind-driven waves. *Coastal Engineering* **58** (12), 1118–1124.

Olfateh, M., Ware, P., Callaghan, D.P., Nielsen, P. & Baldock, T.E. 2017 Momentum transfer under laboratory wind waves. *Coastal Engineering* **121**, 255–264.

Park, P.K. 1969 Oceanic $CO_2$ system: an evaluation of ten methods of investigation. *Limnology and Oceanography* **14** (2), 179–186.

Peirson, W.L., Garcia, A.W. & Pells, S.E. 2003 Water wave attenuation due to opposing wind. *Journal of Fluid Mechanics* **487**, 345–365.

Phillips, O.M. 1957 On the generation of waves by turbulent wind. *Journal of Fluid Mechanics* **2** (5), 417–445.

Phillips, O.M. 1963 On the attenuation of long gravity waves by short breaking waves. *Journal of Fluid Mechanics* **16** (3), 321–332.

Phillips, O.M. 1966 *The dynamics of the upper oceans*. New York: Cambridge University Press.

Ribberink, J.S., Katopodi, I., Ramadan, K.A.H., Koelewijn, R. & Longo, S. 1995 Sediment transport under (non)-linear waves and currents. In *Coastal Engineering 1994*, pp. 2527–2541.

Rivero, F.J. & Arcilla, A.S. 1995 On the vertical distribution of $\langle \tilde{\mathrm{u}}\tilde{\mathrm{w}} \rangle$. *Coastal Engineering* **25** (3-4), 137–152.

Sánchez-Badorrey, E., Losada, M.A. & Rodero, J. 2008 Sediment transport patterns in front of reflective structures under wind wave-dominated conditions. *Coastal Engineering* **55** (7-8), 685–700.

Sánchez-Badorrey, E., Mans, C., Bramato, S. & Losada, M.A. 2009 High-order oscillatory contributions to shear stress under standing regular wave groups: Theory and experimental evidence. *Journal of Geophysical Research: Oceans* **114** (C3).

Snyder, R.L., Dobson, F.W., Elliott, J.A. & Long, R.B. 1981 Array measurements of atmospheric pressure fluctuations above surface gravity waves. *Journal of Fluid Mechanics* **102**, 1–59.

STEWART, R.H. & TEAGUE, C. 1980 Dekameter radar observations of ocean wave growth and decay. *Journal of Physical Oceanography* **10** (1), 128–143.

SULLIVAN, P.P. & MCWILLIAMS, J.C. 2010 Dynamics of winds and currents coupled to surface waves. *Annual Review of Fluid Mechanics* **42**.

SWAN, C. & JAMES, R.L. 2000 A simple analytical model for surface water waves on a depth-varying current. *Applied Ocean Research* **22** (6), 331–347.

THAIS, L. & MAGNAUDET, J. 1995 A triple decomposition of the fluctuating motion below laboratory wind water waves. *Journal of Geophysical Research: Oceans* **100** (C1), 741–755.

THAIS, L. & MAGNAUDET, J. 1996 Turbulent structure beneath surface gravity waves sheared by the wind. *Journal of Fluid Mechanics* **328**, 313–344.

VÍLCHEZ, M., CLAVERO, M., BAQUERIZO, A. & LOSADA, M.Á 2017 An approximation to the statistical characteristics of wind waves in front and from the toe of the structure to the toe of the crown of nonovertopped breakwaters. *Coastal Engineering Journal* **59** (3), 1750012–1.

WALLACE, J.M. 2016 Quadrant analysis in turbulence research: history and evolution. *Annual Review of Fluid Mechanics* **48**, 131–158.

WALLACE, J.M. & BRODKEY, R.S. 1977 Reynolds stress and joint probability density distributions in the u-v plane of a turbulent channel flow. *The Physics of Fluids* **20** (3), 351–355.

YOUNG, I.R. & SOBEY, R.J. 1985 Measurements of the wind-wave energy flux in an opposing wind. *Journal of Fluid Mechanics* **151**, 427–442.

YU, J. & MEI, C.C. 2000 Do longshore bars shelter the shore? *Journal of Fluid Mechanics* **404**, 251–268.